BEAM SHAPING EFFECTS ON MIMO FREE-SPACE OPTICAL COMMUNICATION SYSTEMS

A THESIS SUBMITTED TO

THE GRADUATE SCHOOL OF NATURAL AND APPLIED

SCIENCES OF

ÇANKAYA UNIVERSITY

BY

MUHSİN CANER GÖKÇE

IN PARTIAL FULFILLMENT OF THE REQUIREMENTS FOR THE

DEGREE OF

DOCTOR OF PHILOSPHY

IN

THE DEPARTMENT OF

ELECTRONIC AND COMMUNICATION ENGINEERING

DECEMBER 2016

Title of the Thesis: **Beam Shaping effects on MIMO Free-Space Optical Communication Systems**
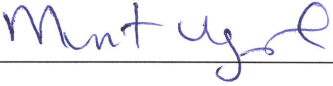
Submitted by **Muhsin Caner GÖKÇE**

Approval of the Graduate School of Natural and Applied Sciences, Çankaya University.
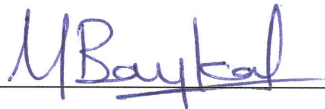
Prof. Dr. Halil Tanyer EYYUBOĞLU
Director

I certify that this thesis satisfies all the requirements as a thesis for the degree of Doctor of Philosophy.

Prof. Dr. Yusuf Ziya UMUL
Head of Department

This is to certify that we have read this thesis and that in our opinion it is fully adequate, in scope and quality, as a thesis for the degree of Doctor of Philosophy.

Prof. Dr. Murat UYSAL
Co-supervisor

Prof. Dr. Yahya Kemal BAYKAL
Supervisor

Examination Date: 23.12.2016
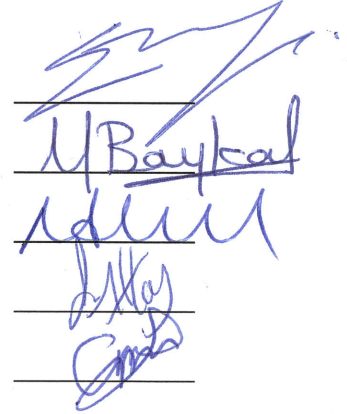
Examining Committee Members

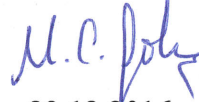|		
Prof. Dr. Erdem YAZGAN (Chair of the Jury)	(TED Univ.)	
Prof. Dr. Yahya Kemal BAYKAL	(Çankaya Univ)	
Assoc. Prof. Dr. Nursel AKÇAM	(Gazi Univ.)	
Assist. Prof. Dr. Serap ALTAY ARPALİ	(Çankaya Univ.)	
Assist. Prof. Dr. Çağlar ARPALİ	(Çankaya Univ.)	

STATEMENT OF NON-PLAGIARISM PAGE

I hereby declare that all information in this document has been obtained and presented in accordance with academic rules and ethical conduct. I also declare that, as required by these rules and conduct, I have fully cited and referenced all material and results that are not original to this work.

Name, Last Name   :   Muhsin Caner GÖKÇE

Signature   :

Date   :   23.12.2016

ABSTRACT

**BEAM SHAPING EFFECTS ON MIMO FREE-SPACE OPTICAL
COMMUNICATION SYSTEMS**

GÖKÇE, Muhsin Caner

Ph.D., Department of Electronic and Communication Engineering

Supervisor: Prof. Dr. Yahya K. BAYKAL

Co-supervisor: Prof. Dr. Murat UYSAL

December 2016, 82 pages

Multiple Input Multiple Output (MIMO) systems are employed in Free Space Optical (FSO) communication links to improve the link reliability in the presence of atmospheric turbulence. In this thesis, we consider a MIMO FSO system with practical transmitter and receiver configurations that consists of a radial laser array with Gaussian beams and a detector array with Gaussian apertures. Using the extended Huygens-Fresnel principle in weak atmospheric turbulence, we have derived formulations to find the average power and the power correlations on the finite sized detectors. This lets us to quantify the performance metrics such as the power scintillation index, the aperture averaging factor and the average bit error rate (<BER>) as a function of system parameters, i.e., transmitter and receiver ring radius, number of Gaussian laser beams, number of detectors, laser source size, detector aperture radius, degree of source coherence, link distance and the structure constant of atmosphere. At first, by the help of the derivations the performance of

multiple-input single-output (MISO) FSO system is investigated using both for coherent and for partially coherent Gaussian sources. Then, we improve our derivations and investigate the performance of MIMO FSO systems. In this way, the performance of MIMO FSO system is compared to that of MISO FSO, single-input multiple-output (SIMO) FSO and single-input single-output (SISO) FSO systems.

MISO systems are then employed in underwater wireless optical communication (UWOC) links to mitigate the degrading effects of oceanic turbulence. To quantify the scintillation index of the MISO UWOC system, the Huygens - Fresnel principle is used with the novel equivalent structure constant of atmosphere. The oceanic turbulence parameters such as rate of dissipation of mean-squared temperature, rate of dissipation of kinetic energy per unit mass of fluid, Kolmogorov microscale, the ratio of temperature to salinity contributions to the refractive index spectrum, link distance and the wavelength which are expressed by the novel equivalent structure constant of atmosphere. Using the Matlab program, we present graphs and investigate the effect of system parameters on the performance metrics.

Keywords: Multiple-Input Multiple-Output Systems, Free Space Optical Communication, Underwater Wireless Optical Communication, Optical Wave Propagation, Oceanic Propagation, Power Scintillation, Aperture Averaging Factor, Bit Error Rate, Laser Arrays.

ÖZ

ÇOK-GİRİŞLİ ÇOK-ÇIKIŞLI SERBEST UZAY OPTİK HABERLEŞME SİSTEMLERİNDE OPTİK HÜZME ŞEKİLLENDİRMENİN ETKİLERİ

GÖKÇE, Muhsin Caner

Doktora, Elektronik ve Haberleşme Mühendisliği Anabilim Dalı

Tez Yöneticisi: Prof. Dr. Yahya K. BAYKAL

Ortak Tez Yöneticisi: Prof. Dr. Murat UYSAL

Aralık 2016, 82 sayfa

Çok-girişli çok-çıkışlı sistemler, atmosferik türbülanslı ortamda gerçekleştirilen serbest uzay optik haberleşme linklerinin, iletişim kalitesini geliştirmek amacıyla kullanılmaktadır. Bu tezde, pratik bir gönderici için dairesel bir Gauss lazer dizisi ve alıcı için Gauss açıklığa sahip dairesel bir detektör dizisi kullanıldı. Zayıf türbülanslı ortamda Huygens-Fresnel prensibi ile detektörler üzerindeki ortalama optik güç ve güç korelasyonu'nu belirleyecek formülasyonlar geliştirildi. Bu sayede, sistem performans ölçütleri; güç pırıldama indisi, alıcı ortalaması faktörü ve bit hata oranı bulundu. Performansı belirleyen optik sistem parametreleri; gönderici ve alıcı halka yarıçapı, Gauss lazer hüzme sayısı, detektör sayısı, lazer kaynak boyutu, detektör açıklığı yarıçapı, kaynak eşfazlılık derecesi, link uzaklığı ve atmosfer yapı sabitidir. Formülasyon yardımıyla ilk olarak çok–girişli tek-çıkışlı sistemlerin performans analizi hem eşfazlı hem de kısmi eşfazlı Gauss kaynağı kullanılarak incelendi. Daha

sonra formülasyon geliştirilip çok-girişli çok-çıkışlı sistemlerin performans analizi gerçekleştirildi. Çok-girişli çok-çıkışlı sistemlerin performası bu sistemlerin özel bir durumu olan çok-girişli tek-çıkışlı, tek-girişli çok çıkışlı ve tek-girişli tek çıkışlı sistemlerin performası ile karşılaştırıldı.

Çok-girişli tek-çıkışlı sistemler daha sonra sualtı kablosuz optik haberleşme linklerinde karşılaşılan okyanus türbülansının iletişimi bozucu etkisini azaltmak amacıyla kullanıldı. Pırıldama indisi, Huygens-Fresnel prensibi ve yeni bir birim olan eşdeğer atmosfer yapı sabiti kullanılarak hesaplandı. Okyanus türbülans parametreleri; ortalama kare sıcaklık yitim oranı, sıvı birim kütlesi başına kinetik enerji yitim oranı, Kolmogorov mikro ölçütü, sıcaklığın tuzluluk katılımı ve kırılma indisine oranı, link uzaklığı ve dalgaboyu eşdeğer atmosfer yapı sabiti yardımıyla ifade edildi. Matlab programı kullanılarak sistem parameterlerinin performans ölçütleri üzerindeki etkileri incelendi ve grafikler sunuldu.

Anahtar Kelimeler: Çok-Girişli Çok-Çıkışlı Sistemler, Serbest Uzay Optik Haberleşmesi, Sualtı Kablosuz Optik Haberleşmesi, Optik Dalga Yayılımı, Okyanus Yayılımı, Güç Pırıldaması, Açıklık Ortalama Faktörü, Bit Hata Oranı, Laser Dizileri

ACKNOWLEDGEMENTS

TABLE OF CONTENTS

LIST OF FIGURES

FIGURES

LIST OF ABBREVIATIONS

FSO	Free Space Optic
MIMO	Multiple-Input Multiple-Output
MISO	Multiple-Input Single-Output
SIMO	Single-Input Multiple Output
SISO	Single-Input Single-Output
UWOC	Underwater Wireless Optical Communication
RF	Radio Frequency
MCF	Mutual Coherence Function
PCB	Partially Coherent Beam
<SNR>	Average Signal to Noise Ratio
<BER>	Average Bit Error Rate
EGC	Equal Gain Combining
IOT	Internet of Things
AUV	Autonomous Underwater Vehicle
ROV	Remotely Operated Vehicles
LED	Light Emitting Diode
PIB	Power in the Bucket
RMS	Root Mean Square
MTF	Modulation Transfer Function
FOV	Field of View
TEM	Transverse Electro-Magnetic

LIST OF SYMBOLS

$u\left(\mathbf{s}, z{=}0\right)$	Laser beam profile
$u\left(\mathbf{s}, z{=}L\right)$	Received optical field
k	Wave number
λ	Wavelength
α_s	Laser source size
$\mathbf{s}$	Source transverse coordinate
$\mathbf{p}$	Receiver transverse coordinate
L	Link distance
$G\left(\mathbf{s},\mathbf{r},z\right)$	Green's function
$\psi\left(\mathbf{s},\mathbf{p}\right)$	The random part of the complex phase of a spherical wave
$\langle\ \rangle$	Ensemble average over the random medium statistics
$\Phi\left(\kappa\right)$	The power spectrum model of turbulence
κ	Scalar spatial frequency
ℓ_0	Inner scale of turbulence
L_0	Outer scale of turbulence
C_n^2	Index-of-refraction structure constant in atmosphere
w	Rms wind speed
h_l	Height from the ground
$\Gamma_2\left(\mathbf{p}_1,\mathbf{p}_2,L\right)$	Mutual coherence function
$\left\langle I\left(\mathbf{p},L\right)\right\rangle$	Average intensity at the receiver
D_ψ	Wave structure function.
ρ_0	Coherence length of a spherical wave

$\Gamma_4\left(\mathbf{p}_1,\mathbf{p}_2,\mathbf{p}_3,\mathbf{p}_4,L\right)$	Fourth-order coherence function
$\left\langle I^2\left(\mathbf{p},L\right)\right\rangle$	Average of the square of the intensity
$\Gamma_4^m\left(\mathbf{s}_1,\mathbf{s}_2,\mathbf{s}_3,\mathbf{s}_4,\mathbf{p}\right)$	Fourth order spherical-wave coherence function of the medium
B_χ	Log amplitude correlation function
$\sigma_{\chi_s}^2$	Spherical wave log amplitude variance
$D_{\chi S}$	Log-amplitude and phase structure function,
$\rho_{\chi S}$	Coherence length of log amplitude and phase
m^2	Scintillation index
m_p^2	Power scintillation index
$\left\langle P\right\rangle$	Average power
$h\left(\mathbf{p}\right)$	Gaussian aperture function
R_r	Receiver aperture radius
$\left\langle I\left(\mathbf{p_1}\right)I\left(\mathbf{p_2}\right)\right\rangle$	Intensity correlation at the receiver
$\left\langle P^2\right\rangle$	Average of the square of the power
G_R	Aperture averaging factor
$p_I\left(.\right)$	Probability density function
r_0	Transmitter ring radius
r_r	Receiver ring radius
N	Number of Gaussian beamlets
H	Number of receiver apertures
ρ_s	Degree of source coherence level
ε	Rate of dissipation of kinetic energy per unit mass of fluid
X_T	Rate of dissipation of mean-squared temperature

η	Kolmogorov inner scale
ω	Ratio of temperature to salinity contributions to the refractive index spectrum

CHAPTER 1

INTRODUCTION

1.1 Background

Free space optical (FSO) communication systems provide a high data rate point-to-point wireless communication solution over distances of a few kilometers. Despite the lack of communication range, FSO presents many potential advantages over radio frequency (RF) and fiber optical counterparts [1]. For example, in comparison to RF systems, the FSO link offers much higher data rates, requires no spectrum license and needs no frequency allocation [2-5]. Further, narrow laser beams are used in FSO systems, and thus inherent security is achieved and interference between end users is prevented. In comparison to fiber optical systems, FSO links are easily set up within hours. On the other hand, fiber deployment takes a long time and is costly [6]. Fiber also requires digging of trenches, which may cause traffic jams, pollution, cutting of trees, and destruction of historical places [7]. Specifically, transmission rates of FSO systems are comparable to that of optical fiber systems [8, 9], and it affords to provide 10 Gb/s over metropolitan distances of a few city blocks to a few kilometers with low probability of errors. There have been a wide range of application areas for FSO system, some of which are last mile access, enterprise (campus) connectivity, backhaul for cellular systems and fiber backup [10, 11]. There are also cutting-edge FSO applications which are employed in military [12], deep space [13], inter-satellite [14], aerostat-to-ground [15], space-to-ground, ground-to-space [16] communication systems.

In spite of the major advantages of FSO system, its performance is affected by deployment challenges such as misalignment loss and geometric loss. Additionally, the transmission media of the FSO links is turbulent atmosphere which exhibits

random behaviors that can affect the attributes of the propagating optical beam, and consequently resulting in atmospheric attenuation and intensity fluctuations (scintillation).

Misalignment or pointing loss occurs due to displacement between the laser beam center and the receiver aperture center, and this mainly causes power loss and thus errors in the received signal. Since FSO systems use highly directional and narrow laser beams, it is difficult to configure line of sight precise pointing between transceiver units, especially in long-distance paths (>1 km) [17]. Building sway, vibration and weak earthquakes are possible causes of misalignment, which constantly interrupts the line-of-sight. These interruptions occur randomly and have a statistical distribution with a variance called jitter [18-19]. In addition, pointing loss may arise due to atmospheric turbulence (i.e., beam wander and beam spreading) [20-23]. For example, beam wander is caused by large-scale turbulence eddies. It may result in random deflections of the optical beam from its original path [24-25]. Another deployment challenge is the excess geometric loss which originates from the divergence angle of the laser beam when propagating through the space [1]. In space, usually, the beam spreads to a size larger than the receive aperture, and as a result, some portion of the optical power is lost. Since most of the laser beams have typically Gaussian intensity profile, the geometric loss can be found under the given divergence angle, wavelength, source size, link distance, and the receiver aperture size [26]. Additionally, laser beam spreads more in the presence of atmospheric turbulence. This extra expansion is called turbulence-induced beam spreading which can be calculated by using the mutual coherent function (MCF) [27]. Lastly, the knowledge of pointing and geometric loss are important to determine the system performance, which have been widely studied in the presence of atmospheric turbulence [18,21-30].

Atmospheric attenuation occurs due to the absorption and the scattering. These terms are usually grouped together under the topic of extinction. Absorption results from gaseous molecules and aerosols in the atmosphere where the incident photon energy is absorbed, causing an attenuation of the optical power. This phenomenon is wavelength dependent and therefore selective [31]. It is known that the atmosphere

has transparent zones of wavelengths (i.e., have an attenuation of <0.2 dB/km) which is called transmission window. The optical signal can be transmitted through this window with minimal attenuation, and therefore the majority of FSO application is utilized to operate in the windows of 0.7–0.8 μm and 1.5–1.6 μm [11,32]. In the near-IR wavelength, absorption originates primarily from the water particles (i.e., moisture) [2,33,34]. Furthermore, these particles also cause light scattering, which is the deflection of incident light from its initial direction. The light scattering results in attenuation of the transmitted signal, as well as causing spatial, angular and temporal spread [26]. Three types of scattering mechanism, i.e., Rayleigh [35], Mie [36] and geometric [37] have been observed during the optical wave propagation. Practically, these scattering types can be classified based on the ratio of particle size to laser wavelength. For example, if this ratio is much less than unity, it is classified as Rayleigh scattering; if it is near unity it is Mie scattering. In addition, geometric scattering occurs when this ratio is much larger than unity. An interesting point to note is that, the FSO transmission is nearly unaffected by the thin rain and the light snow because of the size of raindrops and snowflakes are much larger than the laser wavelength [38]. However, the heavy rain and heavy snow have a major effect on the availability of FSO links [39].

The other and most severe challenge faced in FSO systems is the intensity fluctuations which is quantified by the scintillation index. The scintillation, namely turbulence induced signal fading, results in large fluctuations of the received signal, causing degradation in the link performance [26, 27]. For instance, starwatchers as early as Aristotle have observed the scintillation as a natural phenomena (changes in brightness of the stars due to the turbulent atmosphere). Up to now, many turbulence models have offered and discussed to explain the physical structure of the atmosphere [40-42], one of which is Kolmogorov turbulence theory. According to Kolmogorov turbulence theory, scintillation occurs due to refractive-index fluctuations (also known as atmospheric turbulence) resulting from small temperature fluctuations [40]. In daytime, temperature differences between earth's surface and atmosphere cause fluctuations in the temperature, which in turn constitute turbulence eddies [43-45]. It is assumed that the atmosphere contains different sizes of turbulence eddies which have deleterious effects on the propagating

3

wave. For example, small-scale and large-scale turbulence eddies cause intensity scintillation and beam wander, respectively. It is known that the effect of the scintillation on the performance of FSO system is pronounced. To improve system performance, scintillation effects can be mitigated by the use of partially coherent beams (PCB), aperture averaging or spatial diversity techniques. In the following, we will focus on the performance enhancement techniques to reduce the effect of scintillation.

The use of partially coherent source can reduce intensity scintillation, and therefore the performance of FSO system is enhanced. However, the received power is reduced due to inherent beam spreading [46-48]. There are several ways to generate partially coherent source. As an example, by using a diffuser (i.e., a spatial phase filter with a transmission function) at the transmitter, spatial coherence of the laser beam can be distorted and thus partially coherent source is produced [49]. Theoretically, the mutual coherence function is used to investigate propagation properties of partially coherent beams [50-51]. Further, the scintillation index of the partially coherent source has been widely studied in the literature by considering two different cases. These cases are fast detector (i.e., detection time is less than the source coherence time) and slow detector (i.e., detection time is greater than the source coherence time). For example, the scintillation index of incoherent beam is calculated by Fante for both slow and fast detectors [52]. Similarly, Baykal et al. formulated the scintillation index of the partially coherent beam [53]. In their study, the extended Huygens-Fresnel principle and the exponential approximation for the log-amplitude covariance function were applied. In weak atmospheric turbulence, researchers reported that calculation of the scintillation index is complicated for partially coherent beam compared to that of a coherent beam [46-48]. For this reason, a quadratic approximation is introduced in the two-source structure functions for a spherical wave due to its simplicity [54]. Researchers also reported that experimental works which investigate the scintillation index of the partially coherent source have confirmed the theoretical studies [55-56].

The other and useful technique for scintillation reduction is the aperture averaging that is achieved by enlarging the receiver aperture area. This technique is applied in

FSO systems to smooth out the distorted wavefront as well as to increase the received signal-to-noise ratio. The process of smoothing makes a shift in the irradiance power spectrum (i.e., high spatial frequencies of irradiance is shifted to low spatial frequencies) which in turn results in reduced scintillation. Aperture averaging is first recognized by astronomical observers who want to measure intensity twinkling of starlight in 1950s [57]. They reported that an increase in the telescope aperture area causes the scintillation to decrease. For successful aperture averaging, the receiver lens aperture needs to be larger than the irradiance correlation width. This way, aperture lens sees several uncorrelated signals and average these signal waveforms, leading to reduced scintillation. Furthermore, the performance of aperture averaging is usually quantified by aperture averaging factor which is defined as the ratio of the scintillation index of a finite sized aperture (i.e., power scintillation index) to a point aperture. In the literature, various works have been introduced to investigate the performance of aperture averaging under the assumption of spherical wave (i.e., point source), unbounded plane wave and the Gaussian beam wave propagation. In weak atmospheric turbulence, aperture averaging factor of plane wave was calculated by Fried and Tatarskii by using numerical integration and mathematical formulation, respectively [58,59]. Later, Andrews derived the exact analytical expressions for both spherical and plane wave with the help of interpolation formulas [60]. A similar study was performed for the Gaussian beam wave by using the Huygens - Fresnel principle [61]. Moreover, the performance of aperture averaging has been investigated by employing various beam shapes such as flat topped, multi-Gaussian and annular beams [62-64]. In strong atmospheric turbulence, power scintillation index and aperture averaging factor of plane and spherical waves have been widely studied considering the inner and outer scale of atmospheric turbulence [65, 66]. Aperture averaging analysis of Gaussian beam wave has been performed using both exponential Weibull distribution [67] and Rytov method [26,27]. The performance measure in FSO system related to scintillation can be quantified by some metrics such as <BER>, outage probability and channel capacity. As an example, BER improvement by aperture averaging under the plane, spherical and the Gaussian beam wave models have been studied in [68]. In addition, the combined effects of aperture averaging and the use of partially coherent source on channel capacity have been reported [69]. It was found that the beam size

optimization of partially coherent source and use of larger area of receiver aperture improve the average channel capacity.

Another important technique is spatial diversity which reduces the effects of scintillation and enhances the performance of the FSO links by employing multiple separated beams and/or small aperture detectors. We will focus on the application of spatial diversity techniques as in the case of transmit diversity, also known as MISO, receiver diversity, SIMO, and both transmit and receive diversity, MIMO, systems. The receiver diversity system is achieved by the fact that small aperture detectors are separated by one or more irradiance coherence width to ensure that the received signal undergoes statistically independent signal fades, which in turn provides diversity gain. In a similar manner, seperated laser beams constitue statistically independent signal channels which may provide transmit diversity gain and overcome the limitations on the transmit optical power. The diversity gain increases multiplicatively when transmit and receive diversity are implemented together [70].

The publications of Navidpour et al. [71] and Lee et al. [72] are two of the studies on spatial diversity in which spherical and plane wave propagation are considered. Navidpour et. al. derive general BER formula and express the MIMO system performance in terms of a SISO system with proper scaling in the scintillation assuming both independent and correlated channels among transmitter and receiver apertures [71,73]. Similarly, Lee et. al. derive outage probability for a spatial diversity system as well as assuming the time diversity that consider equal gain combining (EGC), select-max combining and optimal combining [72, 74]. Furthermore, Haas and Shapiro have developed expression to find the ergodic channel capacity of the MIMO FSO link where its efficacy verified through Monte Carlo simulations [75]. Performance gains of these systems have been emphasized in weak atmospheric turbulence. In addition to the weak atmospheric turbulence, Khalighi et. al. investigate the joint effects of receiver diversity and aperture averaging on the system performance considering moderate and strong turbulence regimes. They present substantial reports which compare the performance gains of single and multiple aperture receivers for different turbulence regimes [76]. BER performance of SIMO system is taken into account by considering the pointing errors

in strong atmospheric turbulence [77]. Similarly, many studies have been reported in the literature by considering spherical and plane wave propagation [78-81].

Performance analysis of spatial diversity systems has been mainly investigated with the help of the basic plane and spherical wave assumptions due to their simplicity in mathematical formulations. However, when practical system is considered, the FSO performance becomes relatively different from its theoretical assumptions. For this reason, the source size and shapes of laser beams and their transmitter configurations (i.e., linear, radial, rectangular and star), degree of source coherence, sizes of receiver apertures and their receiver configurations are important when the performance of FSO system is analyzed. Therefore, consideration of performance analysis with the help of beam optics and finite sized receiver apertures are much more realistic [82, 83]. In the literature, propagation properties and beam quality factors of laser array beam for rectangular and radial symmetry have been reported [84, 85]. Field correlation of MISO and MIMO systems has been investigated by using laser arrays with the help of the Huygens-Fresnel principle [86, 87]. In a similar manner, the scintillation index analysis of the MISO FSO system with different beam shapes such as partially coherent multiple Gaussian, off-axis Gaussian, partially coherent annular and flat-topped array, point source array, and the laser beam array has been performed for a point detector [88-93]. Rytov method has been also used to examine the scintillation performance of the MISO FSO system [94]. There are also experimental works which confirm the theoretical studies given above [95, 96]. Another interesting study is that researchers found the optimum number of laser beams in order to minimize scintillation [97]. In addition, the joint effects of spatial diversity and the use of incoherent sources on channel capacity have been reported [98]. Furthermore, Anguita et al. have reported a simple scaling rule to find lowest BER in [99], where relative separation distances of laser beams on the transmitter plane are determined based on the link distance. Similar study has been performed for both collimated and divergent Gaussian beams for MIMO system under different link conditions [100].

More recently, laser array beam and a finite sized Gaussian aperture are employed in MISO FSO system [101-103]. Power and power correlations on the finite sized

detectors are formulated by using the extented Huygens-Fresnel principle in weak atmospheric turbulence. This way, the performance metrics such as power scintillation index, aperture averaging factor and <BER> are found. Then, the formulations of Ref. [102] are developed by using mutual coherence function for the source. Further, in this way, the effect of partial coherence on the performance of MISO FSO system is examined [104,105]. In addition, finite sized detector array and partially coherent radial array beam are employed in MIMO FSO system [106]. Consequently, the performance of SISO, MISO, SIMO and the MIMO systems are investigated in detail and compared with each other.

Underwater wireless optical communication (UWOC) system is an emerging technology which presents many potential advantages over classical acoustic system counterparts [107,108]. This originates from the fact that acoustic and optical waves have different characteristics in underwater medium which affect the communication performance. Optical waves in underwater medium provide incomparably high data rates (up to hundreds of Megabits/sec) [109-112], whereas acoustic signals propagate slowly that cause large latencies leading to low communication data rates (up to few hundreds of kbits/sec) [113,114]. Due to this high data rate superiority, the utilization of UWOC system has gained more popularity in recent years and it has been suggested for human activities (i.e., underwater monitoring, surveillance, archaeology) with the help of autonomous underwater vehicles (AUVs), the concept of internet-of-things (IOT), military applications with the help of remotely operated vehicles (ROVs) and sensor networks which require high data rates [115-118].

As in the atmosphere, the optical signal is affected by absorption, scattering and oceanic turbulence in underwater medium [119-121]. Absorption and scattering result from the presence of sea water constituents such as the dissolved salts, chlorophyll, suspended particulate matter and water molecules, etc. [122] which attenuate the received optical signal, causing a limitation on the link distance (i.e., short communication ranges: distances of few hundreds of meters) [123]. For this reason, researchers have studied and proposed theoretical and experimental studies to determine relatively transparent zones of wavelengths in the seawater [124,125]. It has been reported that wavelengths from 450nm to 550nm which correspond to the

blue and green spectrum are suitable for optical signal transmission with minimum attenuation. Another challenge is oceanic turbulence and its major effect is the intensity fluctuations (scintillation) which severely degrades the communication performance. Generally in clear ocean, absorption and scattering effects are considered small when compared to scintillation effects. Therefore, it is important to understand how oceanic turbulence might affect the performance of the UWOC system. Turbulence mitigation techniques in an FSO system such as aperture averaging, beam focusing, the use of spatially partially coherent source, beam shaping and the spatial diversity are still valid and employed in UWOC system [126-130].

In the literature, fundamentals of many studies such as performance measurements in UWOC system depend on plane and spherical wave assumptions due to its simplicity. The scintillation index of plane and spherical was calculated by using the Rytov method [131] and the fourth-order statistics [132,133] in the weakly turbulent ocean. Furthermore, the spatial diversity is known to be an effective mitigation tool for oceanic turbulence. Using the scintillation index of plane wave and spherical wave, the exact and upper bound BER for MIMO system has been obtained in weak oceanic turbulence in order to precisely calculate the BER performance [134, 135]. It has been found that spatial diversity, especially MISO improves the system performance. Additionally, spatial diversity reduces the scintillation and hence can significantly improve the system performance and remarkably extend the communication range. Furthermore, in [136] BER performance of MISO UWOC system is evaluated by using the combination of log-normal turbulence model and stochastic model in weak turbulence. Moreover, using a light-emitting-diode (LED) and multiple detectors, BER of SIMO system is evaluated with the help of Monte Carlo based statistical simulation method [137]. It is found that scintillation decreases as the number of detectors increase and thus SIMO systems provide significant diversity gain. Also, the channel capacity and SNR are derived for downlink MIMO UWOC system. An interesting point is noted that inter-spacing between transmitter elements may reduce the channel capacity [138].

Plane and spherical wave assumptions are widely used to investigate the performance of the UWOC system. However, in practical UWOC links, Gaussian beam wave is much more realistic than the plane and the spherical waves assumptions. Therefore, several works related to spatial diversity have been performed with the help of Gaussian beams. Additionally, the Gaussian beam wave can also be reduced to the spherical and the plane wave in the limiting case (i.e., in the far field approximation). Using the Huygens-Fresnel principle and power spectrum of oceanic turbulence proposed by Nikishov [139], the average intensity distribution of Gaussian beam array propagating in turbulent ocean has been investigated for coherent and incoherent incidences [140]. Also, the average intensity, beam quality factor, power-in-the-bucket (PIB) and the spreading of radial beam array have been analysed as functions of oceanic turbulence parameters [141, 142]. In a similar manner, the effect of oceanic turbulence on the radius of curvature and the root-mean-square (RMS) beam width of the Gaussian beam array have been examined [143]. In the meantime, spectral degrees of coherence and polarization of array beams with partially coherent flat-topped beamlets have been explored [144]. Recently, Baykal has presented a new technique to express the oceanic turbulence parameters by an atmospheric structure constant [145]. This way, rich archive of formulations of physical entities such as average intensity and the scintillation index, which were derived for FSO system can be valid and used for UWOC system. As an example, the scintillation index of the MISO UWOC system has been derived by using Huygens-Fresnel principle and the equivalent structure constant of atmosphere [146].

A number of experimental studies have also considered for spatial diversity systems. Fading statistics (scintillation) measurement was quantified in [147], where two transmitter and two receiver system were proposed. Furthermore, Kanaev et al. in [148] quantified the wavefront distortion in spatial domain by using LED array. In their study, strength of the turbulence was controlled by temperature fluctuations in water tank and modulation transfer function (MTF) measured by the high-speed camera was demonstrated. Also, using highly directional LED array, field of view (FOV) and SNR performance of MISO UWOC system were measured [149].

In this thesis, we have employed laser array beam and a finite sized Gaussian aperture in MISO FSO system. Average power and average of the square of the power on the finite sized detector are formulated by using the extented Huygens-Fresnel principle in weak atmospheric turbulence. This way, the performance metrics, namely power scintillation index, aperture averaging factor and <BER> are found. Then, our formulation is developed by using mutual coherence function for the source. Further, in this way, we examine the effect of partial coherence on the performance of MISO FSO system. In addition, we employ finite sized receiver apertures and partially coherent radial array beam in MIMO FSO system. Consequently, the performance of SISO, MISO, SIMO and the MIMO systems are investigated in detail and compared with each other. It has been found that MIMO system shows better link performance than those in SIMO, MISO and SISO systems for both coherent and partially coherent sources.

In the second part of the thesis, we have employed laser beam array and a point detector in MISO UWOC system. Oceanic turbulence parameters which were expressed in terms of equivalent structure constant of atmosphere [145] has been used in the study. In this way, we have derived the average intensity and average of the square of the intensity on the point detector by using the extented Huygens-Fresnel principle in weak oceanic turbulence and found the performance metrics, namely scintillation index and <BER>. Thus, the performance of SISO and MISO UWOC systems are investigated in detail and compared with each other. It has been found that MISO UWOC system shows better link performance than that of SISO UWOC system. Note that we mainly focus on the transmit diversity, MISO in underwater turbulence because they provide additional power gain and are easily employed by using multiple laser sources at the transmitter. This can be a significant advantage in terms of the receiver complexity design when compared to the MIMO and SIMO systems which use multiple detectors. In fact, the underwater medium is a challenging environment due to its harsh nature and thus placing multiple detectors in fixed locations to realize SIMO and MIMO is difficult especially for ocean observatories, but on the other hand MISO systems are preferable for their simplicity and less costly advantages when compared to MIMO and SIMO systems. It is also recommended that MISO system is more suitable for AUVs and ROVs [150, 151].

1.2 Objectives

The aim of this thesis is to examine various configurations for mitigating the degrading effects of atmospheric turbulence and hence improve the FSO system performance by employing multiple transmitters with realistic beam shapes and multiple detectors with finite sized apertures in the presence of weak atmospheric turbulence. We also employ aperture averaging and partially coherent laser sources in FSO system as turbulence mitigation technique. Within this context, average intensity, average power, intensity correlation, power correlation are derived on the receiver apertures to calculate the performance indicators, namely scintillation index, power scintillation index and <BER>. In this way, effect of system parameters has been scrutinized on the performance of the SISO, MISO, SIMO and the MIMO FSO system. It is found that the MIMO FSO system shows better performance than those in SISO, MISO and SISO FSO systems. In the second part of the thesis, the turbulence mitigation techniques used in the FSO communication system are then repeated for UWOC system. In fact, performance evaluation in underwater turbulence using realistic beam shapes necessitates solving multiple integrals numerically (for example, to calculate the scintillation index of Gaussian beam wave by Rytov method, the threefold numerical integration is required). An analytical solution can be obtained with the help of the Huygens Fresnel principle. Thus, the previously derived formulations for the MISO FSO system are reformulated for the MISO UWOC system. This is achieved using the equivalent structure constant of atmosphere [146] which describe the atmospheric turbulence in terms of oceanic turbulence parameters. We aimed at demonstrating the effect of oceanic turbulence parameters, as well as system parameters on the performance of the MISO UWOC system. Thus, the average intensity and the average of the square of the intensity on the point detector are found to calculate the scintillation index and <BER> in underwater turbulence. We have observed that MISO UWOC systems show better scintillation and <BER> performance than SISO UWOC systems.

The general aims in order to increase the performance of both FSO and UWOC systems are emphasized as follows

- Use multiple laser sources and multiple detectors in order to obtain transmit and receive diversity gain as well as to increase the received signal to noise ratio and overcome the limitations on the transmit optical power.

- Use larger area of the receiver aperture in order to smooth out the distorted wavefront as well as to increase the received signal to noise ratio.

- Increase the relative distances between laser sources in order to constitute statistically independent signal channels.

- Increase the relative distances between receiver detectors to achieve statistically independent signal channels.

- Use partially coherent source instead of laser source to generate smooth wavefront.

- Arrange beam divergence to fill receiver aperture area with the received optical beam by choosing the source size properly.

1.3 Thesis Outline

The rest of this thesis is organized as follows:

In Chapter 2, we have introduced the laser beam propagation geometry under consideration. Then, some crucial entities used in an FSO communication system such as the mean field, field and intensity correlation, average received intensity and power, scintillation, aperture averaging factor and average <BER> are defined.

In Chapter 3, MISO and MIMO FSO system model are introduced. Performance analyses of spatial diversity systems (i.e., MISO, SIMO and MIMO) have been achieved by formulating received average power and average of the square of the power on the finite-sized receiver detectors. This way, performance metrics, namely the power scintillation index, aperture averaging factor and <BER> are illustrated as a function of system parameters.

In Chapter 4, oceanic turbulence parameters have been expressed in terms of the equivalent structure constant of the atmosphere. By this technique, derived formulations in Chapter 3 can be reused to derive average intensity and the average

of the square of the intensity on the point detector in underwater turbulence. This way, performance analysis of MISO underwater optical communication system has been investigated by means of scintillation index and average bit error rate.

The thesis is finalized with the conclusion in Chapter 5.

CHAPTER 2

LASER BEAM PROPAGATION THROUGH ATMOSPHERE

2.1 Gaussian Beam Wave for a Laser Source

The output emanating from the ideal coherent laser source is assumed to be a Gaussian field profile, which corresponds to transverse electromagnetic field (TEM00 mode). That is

$$u(\mathbf{s}) = u(s_x, s_y) = \exp\left[-k\alpha_n\left(s_x^2 + s_y^2\right)\right], \tag{2.1}$$

where $k=2\pi/\lambda$ is the wave number and λ is the wavelength. $\alpha_n = 1/\left(2k\alpha_s^2\right)$ and α_s is the source size. Here $\mathbf{s} = (s_x, s_y)$ shows the source transverse coordinates. This assumption helps us to easily investigate the propagation properties of a coherent laser source. Note that spherical (point source) and unbounded plane wave are the limiting cases of the Gaussian beam, when the source sizes are chosen as $\alpha_s \to 0$ and $\alpha_s \to \infty$ in Eq. (2.1), respectively.

2.2 Source and Output Plane Parameters

To understand the laser beam propagation, the sample propagation geometry is given in Figure 1 [154]. We consider a source plane where the exit aperture of a laser source is obtained from the source transverse coordinates (i.e., Eq. (2.1)). The laser beam with a source size of α_s propagates and after passing through the space reaches the output plane where the propagation direction is perpendicular to the transmitter and receiver. Link distance between the source plane and the output plane is shown

by *L*. The field at the output plane (beam footprint) $u(\mathbf{p}, z = L)$ is characterized by the receiver transverse coordinate $\mathbf{p} = (p_x, p_y)$. In Figure 1, $\mathbf{s_1}$, $\mathbf{s_2}$ and $\mathbf{p_2}$, $\mathbf{p_2}$ show any points on the transmitter and the receiver plane, respectively.
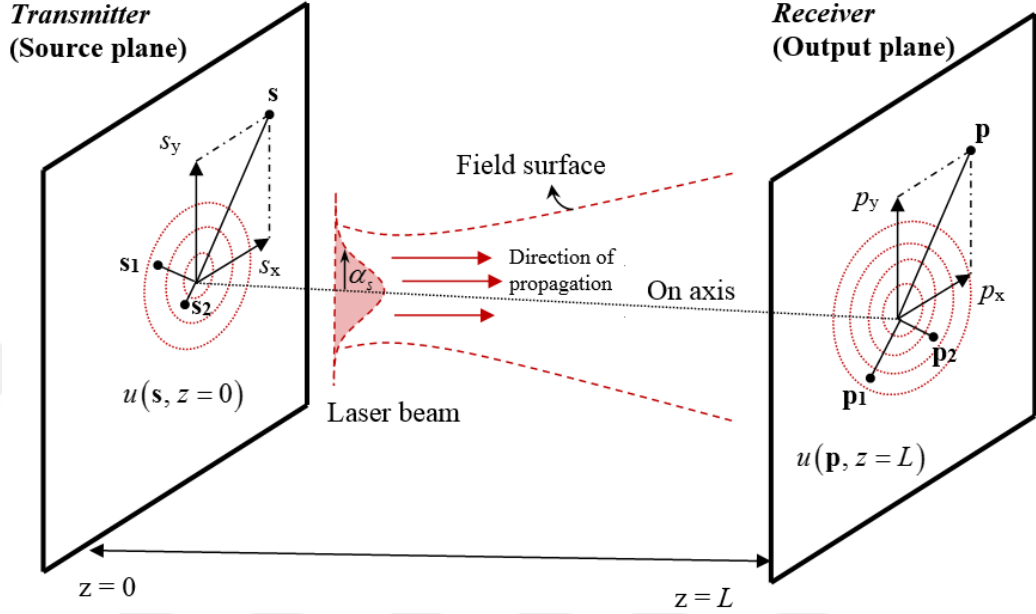
Figure 1 The sample propagation geometry

2.3 Extended Huygens-Fresnel Principle

In free space propagation, laser beam field spreads due to diffraction. The extended Huygens-Fresnel principle which is based on a formal solution of the paraxial wave equation (also known as the parabolic equation) is used to find the received optical field (beam footprint) at the output plane. That is [26]

$$u(\mathbf{p}, z = L) = -2jk \int\limits_{-\infty}^{\infty} \int\limits_{-\infty}^{\infty} d^2\mathbf{s}\, u(\mathbf{s}, z = 0) G(\mathbf{s}, \mathbf{p}, z), \qquad (2.2)$$

where $j = \sqrt{-1}$, $G(\mathbf{s}, \mathbf{p}, z)$ is the Green's function that defines the spherical wave response of the free space medium and given under the paraxial approximation by [26]

16

$$G(\mathbf{s},\mathbf{p},z) \cong \frac{\exp(jkL)}{4\pi L}\exp\left(\frac{jk}{2L}|\mathbf{s}-\mathbf{p}|^2\right) \tag{2.3}$$

Note that Eq. (2.2) is also known as the spatial convolution integral. In the presence of atmospheric turbulence, the optical field at the receiver plane is obtained by applying the spatial convolution integral to the laser beam field and the Green's function of the random medium which is simplified and given as [26].

$$u(\mathbf{p},L) = \frac{\exp(jkL)}{\lambda jL}\int\limits_{-\infty}^{\infty}\int\limits_{-\infty}^{\infty} d^2\mathbf{s}\, u(\mathbf{s},z=0)\exp\left(\frac{jk}{2L}|\mathbf{s}-\mathbf{p}|^2\right)\exp\left[\psi(\mathbf{s},\mathbf{p})\right] \tag{2.4}$$

where $\psi(\mathbf{s},\mathbf{p})$ is the random part of the complex phase of a spherical wave propagating from the source point ($\mathbf{s}$, $z = 0$) to the receiver point ($\mathbf{p}$, L). It should be noted that Eq. (2.4) is given by means of evaluation of many crucial entities used in FSO communication system such as, the mean field, field and intensity correlation, average intensity and power, scintillation and power scintillation, aperture averaging factor and <BER>.

The mean field in the turbulent medium is expressed as [26]

$$\langle u(\mathbf{p},L)\rangle = \frac{\exp(jkL)}{\lambda jL}\int\limits_{-\infty}^{\infty}\int\limits_{-\infty}^{\infty} d^2\mathbf{s}\, u(\mathbf{s},z=0)\exp\left(\frac{jk}{2L}|\mathbf{s}-\mathbf{p}|^2\right)\langle\exp\left[\psi(\mathbf{s},\mathbf{p})\right]\rangle \tag{2.5}$$

where $\langle\ \rangle$ denotes the ensemble average over the random medium statistics. If the random medium is statistically homogeneous and isotropic, the last term of Eq. (2.5) is defined as [27]

$$\langle\exp\left[\psi(\mathbf{s},\mathbf{p})\right]\rangle = \exp\left[-2\pi^2 k^2 L\int\limits_0^{\infty}\kappa\Phi(\kappa)\,d\kappa\right] \tag{2.6}$$

where $\kappa = 2\pi/\ell$ is the scalar spatial frequency, ℓ denotes the size of the turbulent eddy and $\Phi(\kappa)$ is the power spectrum model of turbulence. In the following

17

sections, the performance analyses related to spectrum model will be based on the Kolmogorov power spectrum [26]. Various power spectrum models and turbulence theory are given in Section 2.8.

2.4 Average Optical Intensity at the Receiver

We derive the average received intensity at the output plane with the help of the mutual coherence function (MCF) (also known as the second order moment). That is [27]

$$\Gamma_2\left(\mathbf{p}_1, \mathbf{p}_2, L\right) = \left\langle u\left(\mathbf{p}_1, L\right) u^*\left(\mathbf{p}_2, L\right)\right\rangle \tag{2.8}$$

where $*$ represent the complex conjugate. Note that the spatial coherence and correlation of a field can also be determined by using the MCF. In the case of $\mathbf{p}_1 = \mathbf{p}_2 = \mathbf{p}$ (identical observation points), MCF corresponds to the average intensity [26]

$$
\begin{aligned}
\left\langle I\left(\mathbf{p}, L\right)\right\rangle &= \Gamma_2\left(\mathbf{p}, \mathbf{p}\right) = \left\langle u\left(\mathbf{p}, L\right) u^*\left(\mathbf{p}, L\right)\right\rangle \\
&= \frac{1}{\left(\lambda L\right)^2} \int_{-\infty}^{\infty}\int_{-\infty}^{\infty} \mathbf{d}^2\mathbf{s}_1 \int_{-\infty}^{\infty}\int_{-\infty}^{\infty} \mathbf{d}^2\mathbf{s}_2 u\left(\mathbf{s}_1, z=0\right) u^*\left(\mathbf{s}_2, z=0\right) \\
&= \exp\left(\frac{jk}{2L}\left|\mathbf{s}_1 - \mathbf{p}\right|^2\right)\exp\left(-\frac{jk}{2L}\left|\mathbf{s}_2 - \mathbf{p}\right|^2\right) \\
&= \left\langle \exp\left[\psi\left(\mathbf{s}_1, \mathbf{p}\right)\right]\exp\left[\psi^*\left(\mathbf{s}_2, \mathbf{p}\right)\right]\right\rangle
\end{aligned}
\tag{2.9}
$$

The evaluation of the last line of Eq. (2.9) under the assumption of the Kolmogorov power spectrum yields [50]

$$\left\langle \exp\left[\psi\left(\mathbf{s}_1, \mathbf{p}\right)\right]\exp\left[\psi^*\left(\mathbf{s}_2, \mathbf{p}\right)\right]\right\rangle = \exp\left[-\frac{1}{2}D_\psi\left(\mathbf{s}_1, \mathbf{s}_2\right)\right] \cong \exp\left[-\rho_0^{-2}\left(\mathbf{s}_1 - \mathbf{s}_2\right)^2\right] \tag{2.10}$$

where D_ψ is the wave structure function, $\rho_0 = \left(0.546 C_n^2 k^2 L\right)^{-3/5}$ is the coherence length of a spherical wave propagating in the turbulent medium. In the extended Huygens-Fresnel principle, the field at the receiver is obtained by the convolution of

18

the spherical wave response of the turbulent medium and the source field. This is the reason why in Eq. (2.10), the spatial coherence length ρ_0 is taken for the spherical wave.

2.5 Intensity Scintillation

Fluctuations in the received optical intensity can be quantified in terms of scintillation index as [27]

$$m^2 = \frac{\left\langle I^2\left(\mathbf{p}, L\right)\right\rangle}{\left\langle I\left(\mathbf{p}, L\right)\right\rangle^2} - 1 \tag{2.11}$$

where m^2 is the scintillation index and is also known as the normalized variance of the received irradiance. Here, $\left\langle I\left(\mathbf{p}, L\right)\right\rangle$ is the received optical intensity which was defined in Eq. (2.9). Next, we derive the average of the square of the intensity $\left\langle I^2\left(\mathbf{p}, L\right)\right\rangle$, also known as the second moment of the irradiance, with the help of fourth-order coherence function. That is [27]

$$\Gamma_4\left(\mathbf{p}_1, \mathbf{p}_2, \mathbf{p}_3, \mathbf{p}_4, L\right) = \left\langle u\left(\mathbf{p}_1, L\right) u^*\left(\mathbf{p}_2, L\right) u\left(\mathbf{p}_3, L\right) u^*\left(\mathbf{p}_4, L\right)\right\rangle \tag{2.12}$$

Note that the covariance function of irradiance can also be found by means of the fourth order coherence function. In the case of $\mathbf{p}_1 = \mathbf{p}_2 = \mathbf{p}_3 = \mathbf{p}_4 = \mathbf{p}$ (identical observation points), the fourth order coherence function corresponds to the average of the square of the intensity which is given by [50]

$$\langle I^2(\mathbf{p})\rangle = \Gamma_4(\mathbf{p},\mathbf{p},\mathbf{p},\mathbf{p},L)$$

$$= \frac{1}{(\lambda L)^4} \int\limits_{-\infty}^{\infty}\int\limits_{-\infty}^{\infty} d^2\mathbf{s}_1 \int\limits_{-\infty}^{\infty}\int\limits_{-\infty}^{\infty} d^2\mathbf{s}_2 \int\limits_{-\infty}^{\infty}\int\limits_{-\infty}^{\infty} d^2\mathbf{s}_3 \int\limits_{-\infty}^{\infty}\int\limits_{-\infty}^{\infty} d^2\mathbf{s}_4$$

$$\times u(\mathbf{s}_1)u^*(\mathbf{s}_2)u(\mathbf{s}_3)u^*(\mathbf{s}_4) \qquad\qquad (2.13)$$

$$\times \exp\left[\frac{jk}{2L}\left(|\mathbf{p}-\mathbf{s}_1|^2 - |\mathbf{p}-\mathbf{s}_2|^2 + |\mathbf{p}-\mathbf{s}_3|^2 - |\mathbf{p}-\mathbf{s}_4|^2\right)\right]$$

$$\times \left\langle \exp\left[\psi(\mathbf{s}_1,\mathbf{p})+\psi^*(\mathbf{s}_2,\mathbf{p})+\psi(\mathbf{s}_3,\mathbf{p})+\psi^*(\mathbf{s}_4,\mathbf{p})\right]\right\rangle_m,$$

The last line of Eq. (2.13) is the fourth order spherical-wave coherence function of the medium $\Gamma_4^m(\mathbf{s}_1,\mathbf{s}_2,\mathbf{s}_3,\mathbf{s}_4,\mathbf{p})$. Note that log-amplitude and phase fluctuations are assumed to have Gaussian statistics in weak atmospheric turbulence. We are interested in on axis scintillation and thus evaluating fourth order coherence function of the medium $\Gamma_4^m(\mathbf{s}_1,\mathbf{s}_2,\mathbf{s}_3,\mathbf{s}_4,\mathbf{p})$ at the receiver origin (i.e., at $\mathbf{p}=(p_x,p_y)=(0,0)$ [61, 133])

$$\Gamma_4^m(\mathbf{s}_1,\mathbf{s}_2,\mathbf{s}_3,\mathbf{s}_4,0)=\exp\left[2B_\chi(\mathbf{s}_1-\mathbf{s}_3)+2B_\chi(\mathbf{s}_2-\mathbf{s}_4)\right.$$

$$-\frac{1}{2}D_\psi(\mathbf{s}_1-\mathbf{s}_2)-\frac{1}{2}D_\psi(\mathbf{s}_1-\mathbf{s}_4)-\frac{1}{2}D_\psi(\mathbf{s}_2-\mathbf{s}_3)$$

$$-\frac{1}{2}D_\psi(\mathbf{s}_3-\mathbf{s}_4)+\frac{1}{2}D_\psi(\mathbf{s}_1-\mathbf{s}_3)+\frac{1}{2}D_\psi(\mathbf{s}_2-\mathbf{s}_4) \qquad (2.14)$$

$$\left.+jD_{\chi S}(\mathbf{s}_2-\mathbf{s}_4)-jD_{\chi S}(\mathbf{s}_1-\mathbf{s}_3)\right],$$

where $B_\chi(\mathbf{s}_r-\mathbf{s}_q)=\sigma_{\chi s}^2-0.5(\rho_0^{-2}-\rho_\chi^{-2})(\mathbf{s}_r-\mathbf{s}_q)^2$, $r=1,2,3$ and q=2, 3, 4 is the log amplitude correlation function and $\sigma_{\chi s}^2=0.124k^{7/6}C_n^2L^{11/6}$ is the spherical wave log-amplitude variance and $\rho_\chi=\left(0.425C_n^2k^{13/6}L^{5/6}\right)^{-1/2}$. $D_\psi(\mathbf{s}_r-\mathbf{s}_q)=2\rho_0^{-2}(\mathbf{s}_r-\mathbf{s}_q)^2$ is the wave structure function. The validation of the wave structure function [61] is within the validity $\sqrt{\lambda L}\gg|\mathbf{s_d}|\gg l_0$ where l_0 is the inner scale of turbulence. Note that $l_0=0$ for Kolmogorov spectrum. $|\mathbf{s_d}|$ is the difference of the source transverse coordinates, $\sqrt{\lambda L}$ is the Fresnel zone, $D_{\chi S}(\mathbf{s}_r-\mathbf{s}_q)=\rho_{\chi S}^{-2}(\mathbf{s}_r-\mathbf{s}_q)^2$ is the log-

amplitude and phase structure function, $\rho_{\chi S} = \left(0.114 C_n^2 k^{13/6} L^{5/6}\right)^{-1/2}$ is the coherence length of log-amplitude and phase.

2.6 Power Scintillation and Aperture Averaging Factor

Fluctuations in the received optical power can be quantified in terms of the power scintillation index which is defined as [27]

$$m_p^2 = \frac{\langle P^2 \rangle}{\langle P \rangle^2} - 1, \tag{2.15}$$

where $\langle P \rangle$ is the average power collected by a finite sized aperture. That is [61]

$$\langle P \rangle = \int_{-\infty}^{\infty} \int_{-\infty}^{\infty} \langle I(\mathbf{p}, L) \rangle h(\mathbf{p}) \mathrm{d}^2 \mathbf{p}, \tag{2.16}$$

Here, $\langle I(\mathbf{p}, L) \rangle$ is the received optical intensity which was defined in Eq. (2.9) and $h(\mathbf{p})$ is the Gaussian aperture function with a size of R_r given by

$$h(\mathbf{p}) = \exp\left[-\frac{1}{R_r^2}\left(p_x^2 + p_y^2\right) \right], \tag{2.17}$$

The average of the square of the power as detected by a finite-sized receiver having a Gaussian aperture function is found to be [61]

$$\langle P^2 \rangle = \int_{-\infty}^{\infty} \int_{-\infty}^{\infty} \int_{-\infty}^{\infty} \int_{-\infty}^{\infty} \langle I(\mathbf{p_1}) I(\mathbf{p_2}) \rangle h(\mathbf{p_1}) h(\mathbf{p_2}) \mathrm{d}^2 \mathbf{p_1} \mathrm{d}^2 \mathbf{p_2}, \tag{2.18}$$

To derive intensity correlation $\langle I(\mathbf{p_1}) I(\mathbf{p_2}) \rangle$ appearing in Eq. (2.18), we once again use Eq. (2.12) (fourth-order coherence function) for two observation points which leads to

$$\langle I(\mathbf{p_1})I(\mathbf{p_2})\rangle = \Gamma_4(\mathbf{p_1},\mathbf{p_1},\mathbf{p_2},\mathbf{p_2},L)$$

$$= \frac{1}{(\lambda L)^4} \int_{-\infty}^{\infty}\int_{-\infty}^{\infty} d^2\mathbf{s_1} \int_{-\infty}^{\infty}\int_{-\infty}^{\infty} d^2\mathbf{s_2} \int_{-\infty}^{\infty}\int_{-\infty}^{\infty} d^2\mathbf{s_3} \int_{-\infty}^{\infty}\int_{-\infty}^{\infty} d^2\mathbf{s_4}$$

$$\times u(\mathbf{s_1})u^*(\mathbf{s_2})u(\mathbf{s_3})u^*(\mathbf{s_4}) \qquad (2.19)$$

$$\times \exp\left[\frac{jk}{2L}\left(|\mathbf{p_1}-\mathbf{s_1}|^2 - |\mathbf{p_1}-\mathbf{s_2}|^2 + |\mathbf{p_2}-\mathbf{s_3}|^2 - |\mathbf{p_2}-\mathbf{s_4}|^2\right)\right]$$

$$\times \left\langle \exp\left[\psi(\mathbf{s_1},\mathbf{p_1})+\psi^*(\mathbf{s_2},\mathbf{p_1})+\psi(\mathbf{s_3},\mathbf{p_2})+\psi^*(\mathbf{s_4},\mathbf{p_2})\right]\right\rangle_m.$$

Here, we consider a finite sized aperture. Thus, the fourth order spherical-wave coherence function of the medium appearing in the last line of Eq. (2.19) yields [61]

$$\Gamma_4^m(\mathbf{s_1},\mathbf{s_2},\mathbf{s_3},\mathbf{s_4},\mathbf{p_1},\mathbf{p_2})$$

$$= \left[1 + 2B_\chi(\mathbf{s_1}-\mathbf{s_3},\mathbf{p_d}) + 2B_\chi(\mathbf{s_2}-\mathbf{s_4},\mathbf{p_d})\right]$$

$$\times \exp\left[-0.5D_\psi(\mathbf{s_1}-\mathbf{s_2},0) - 0.5D_\psi(\mathbf{s_3}-\mathbf{s_4},0)\right.$$

$$-0.5D_\psi(\mathbf{s_2}-\mathbf{s_3},\mathbf{p_d}) - 0.5D_\psi(\mathbf{s_1}-\mathbf{s_4},\mathbf{p_d}) \qquad (2.20)$$

$$+0.5D_\psi(\mathbf{s_1}-\mathbf{s_3},\mathbf{p_d}) + 0.5D_\psi(\mathbf{s_2}-\mathbf{s_4},\mathbf{p_d})$$

$$\left.+jD_{\chi S}(\mathbf{s_2}-\mathbf{s_4},\mathbf{p_d}) - jD_{\chi S}(\mathbf{s_1}-\mathbf{s_3},\mathbf{p_d})\right].$$

Here, we have $B_\chi(\mathbf{s_r}-\mathbf{s_q},\mathbf{p_d}) = \sigma_{\chi_s}^2 \exp\left[-\rho_0^{-2}\left(|\mathbf{s_r}-\mathbf{s_q}|^2 + |\mathbf{s_r}-\mathbf{s_q}|\cdot\mathbf{p_d} + \mathbf{p_d}^2\right)\right]$, with r = 1, 2, 3 and q = 2, 3, 4 is the log-amplitude correlation function. $B_x \ll 1$ is taken for approximation in weak turbulence [52] and quadratic approximation is used [153]. $D_\psi(\mathbf{s_d},\mathbf{p_d}) = 2\rho_0^{-2}(\mathbf{s_d}^2 + \mathbf{s_d}\cdot\mathbf{p_d} + \mathbf{p_d}^2)$ is the wave structure function. $D_{\chi S}(\mathbf{s_d},\mathbf{p_d}) = \rho_{\chi S}^{-2}(\mathbf{s_d}^2 + \mathbf{s_d}\cdot\mathbf{p_d} + \mathbf{p_d}^2)$ is the log-amplitude phase structure function.

In the region of weak fluctuations, m_p^2 takes typical values that are quite less than unity.

2.6.1 Aperture averaging factor

The aperture averaging factor quantifies the relative reduction in the fluctuations received by the finite aperture receiver with respect to a point detector. It is described as the ratio of power scintillation normalized by the intensity scintillation at the receiver plane origin. Hence [61]

$$G_R = \frac{m_p^2\big|_{R_r>0}}{m_p^2\big|_{R_r=0}}, \tag{2.21}$$

where $m_p^2\big|_{R_r=0}$ is the intensity scintillation index measured by the point detector given by Eq. (2.11). The power scintillation index detected by finite-sized apertures must be lower than a point aperture for effective aperture averaging.

2.7 Average Bit Error Rate

The performance measure in FSO system related to scintillation or power scintillation is quantified by computing <BER> which is the ultimate indicator of the system performance. It is important that <BER> depends upon the detection type, i.e., direct detection, coherent detection and modulation formats such as on–off keying, pulse amplitude modulation, subcarrier intensity modulation, etc. Assuming on–off keying modulation for direct detection receivers, the <BER> is calculated as [26]

$$\langle \text{BER} \rangle = \frac{1}{2}\int_0^\infty p_I(i)\,\text{erfc}\left(i\frac{\langle \text{SNR}\rangle}{2\sqrt{2}}\right)di, \tag{2.22}$$

where erfc (.) is the complementary error function and <SNR> denotes the average signal-to-noise ratio. Note that the <BER> for on–off-keying modulation is an average over all possible intensity levels of a given probability density function $p_I(.)$. Here, the probability density function and the error function are related to the optical scintillation and the receiver's electronic noise, respectively. In weak

23

turbulence, the intensity I follows the log-normal distribution whose probability density function is given by

$$p_I(I) = \frac{1}{m\sqrt{2\pi}I}\exp\left(-\frac{\left[\ln(I)+0.5m_p^2\right]^2}{2m^2}\right), \; I > 0 \qquad (2.23)$$

where m^2 is the scintillation index. In the following chapter, we will find the scintillation index and investigate the <BER> performance of spatial diversity system. For this purpose, Eq. (2.23) is substituted into Eq. (2.22) and the resulting expression is numerically evaluated for the <BER> calculation.

2.8 Turbulence for an Optical Wave and Power Spectrum Models

Atmospheric and oceanic medium are considered to be viscous and consist of a set of vortices or eddies. Theoretical models of atmospheric and oceanic turbulence have been investigated by a variety of scientists and engineers. Andrey Kolmogorov strengthened our mathematical understanding of atmospheric turbulence. He proposed that the energy in a turbulent fluid varies in proportion to the five-thirds power law [40]. In addition, experimental measurements confirm Kolmogorov was remarkably close to the way turbulent flow works. However, a complete and accurate theory of turbulence that will cover all the media has not been yet proposed.

According to Kolmogorov theory, earth atmosphere heated by the sun generates winds, convection and temperature variations which results in turbulent eddies. It is assumed that the atmosphere contains different sizes of turbulence eddies which have deleterious effects on the propagating optical wave. These effects can be scattering, reflection, refraction and interference which may cause wavefront distortion (i.e., fluctuations in the amplitude and the phase) of the propagating optical wave [154]. The turbulent eddies in the atmosphere behave like lenses ranging from a maximum scale size called the outer scale of turbulence L_0 to a minimum scale size called inner scale of turbulence ℓ_0. Large scale eddies transfer their energy to smaller scale eddies which do likewise to other scales, creating a continuous cascade of scale sizes

(inertial range) between ℓ_0 and L_0. Eventually, the energy is mainly dissipated into heat at the smallest eddies (i.e., known as dissipation range). To clarify as described above, Kolmogorov cascade theory is given in Figure 2 which is taken from Ref. [27].
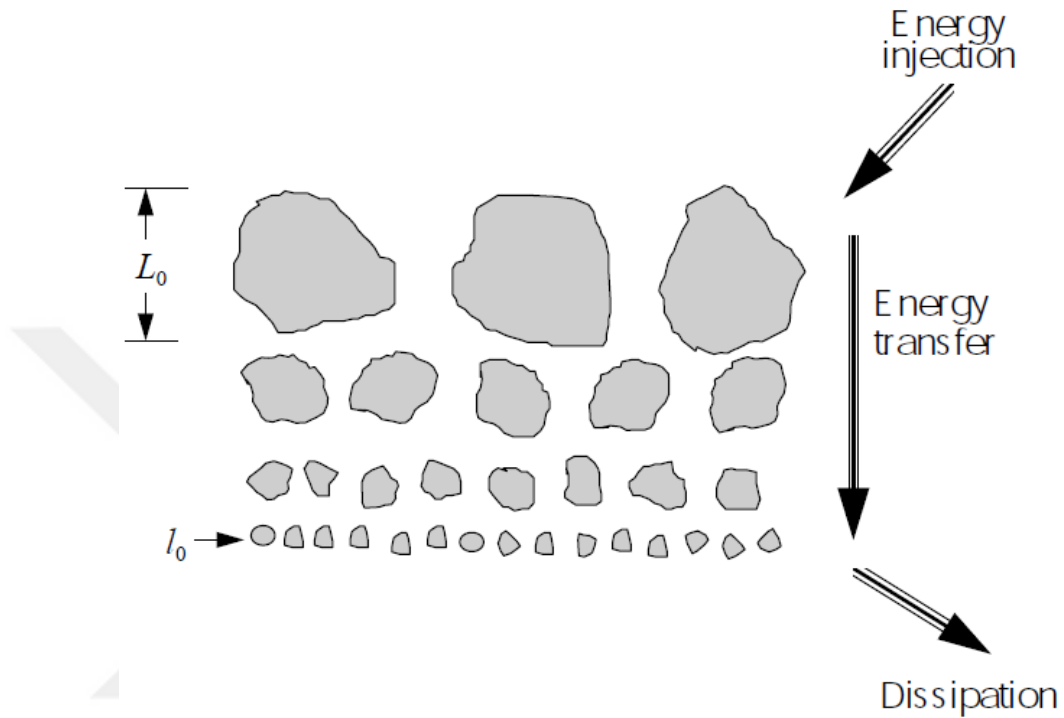
Figure 2 Kolmogorov cascade theory of turbulence.

Near the ground, ℓ_0 normally takes values on the orders of millimeters, on the other hand, the range of L_0 is typically 25 m. It is known that the turbulent eddies are associated with the spatial frequency in the power spectrum of turbulence in which the scale sizes of the eddies are inversely proportional to the spatial frequency. Therefore, ℓ_0 and L_0 correspond to maximum and minimum spatial frequencies, respectively. The effect of the eddies of all scale sizes are integrated in three-dimensional Kolmogorov power spectrum, which is described by [154]

$$\Phi(\kappa) = 0.033 C_n^2 \kappa^{-11/3}, \quad 1/L_0 \le \kappa \le 1/\ell_0 \tag{2.24}$$

Here, ℓ_0 and L_0 are generally taken as $\ell_0 = 0$ and $L_0 = \infty$ for Kolmogorov turbulence model which means that all the spatial frequencies are considered. C_n^2 is the index-of-refraction structure constant that typically characterizes the strength of optical turbulence in atmosphere. Under the assumption of Hufnagle-Valley (H-V) model, height-dependent structure constant is given by [154]

$$C_n^2(h_l) = 0.00594 \left(\frac{w}{27}\right)^2 \left(10^{-5} h_l\right)^{10} \exp\left(-\frac{h_l}{1000}\right) + 2.7 \times 10^{-16} \exp\left(-\frac{h_l}{1500}\right) + A\exp\left(-\frac{h_l}{100}\right)$$

(2.25)

where h_l is the height from the ground expressed in meters. A is the nominal value of $C_n^2(h_l = 0)$ in $m^{-2/3}$, w is the rms wind speed in meters per second (m/s). We also note that the Kolmogorov spectrum is valid for horizontal FSO links where C_n^2 is a constant. Our investigations in this thesis are for horizontal links.

When the effect of inertial range is considered, the use of von Kármán spectrum is frequently preferred which is

$$\Phi_n(\kappa) = 0.033 C_n^2 \frac{\exp\left(\kappa^2/\kappa_m^2\right)}{\left(\kappa^2 + \kappa_0^2\right)^{11/6}}, \qquad 0 \leq \kappa \leq \infty$$

(2.26)

where $\kappa_m = 5.92/\ell_0$ and $\kappa_0 = 2\pi/L_0$. It should be noted that when $\kappa_0 = 0$, the von Kármán spectrum reduces to the Tatarskii spectrum [26].

Lastly, underwater oceanic turbulence under consideration is presented. Under the assumption of equal eddy thermal diffusivity and the diffusion of salt, power spectrum of homogeneous and isotropic oceanic water is given by [145]

$$\Phi_n(\kappa) = 0.388 \times 10^{-8} \varepsilon^{-1/3} \kappa^{-11/3} \left[1 + 2.35(\kappa\eta)^{2/3} \right]$$
$$\times \frac{X_T}{\omega^2} \left(\omega^2 e^{-A_T\delta} + e^{-A_S\delta} - 2\omega e^{-A_{TS}\delta} \right),$$

<div align="right">(2.27)</div>

where ε is the rate of dissipation of kinetic energy per unit mass of fluid, X_T is the rate of dissipation of mean-squared temperature, η is the Kolmogorov microscale (inner scale), ω is a unitless parameter providing the ratio of temperature to salinity contributions to the refractive index spectrum, which ranges from -5 to 0 and refers to the dominating temperature and salinity-induced optical turbulence, respectively, $A_S = 1.9 \times 10^{-4}$, $A_T = 1.863 \times 10^{-2}$, $A_{TS} = 9.41 \times 10^{-3}$ and, $\delta(\kappa,\eta) = 8.284(\kappa\eta)^{4/3} + 12.978(\kappa\eta)^2$.

CHAPTER 3

PERFORMANCE ANALYSIS OF SPATIAL DIVERSITY SYSTEMS IN TURBULENT ATMOSPHERE

3.1 Aperture Averaging in MISO FSO System

In this section of the thesis, we consider a MISO FSO system consisting of a radial transmit array with coherent Gaussian sources and a finite-sized detector with a Gaussian aperture. The power scintillation and aperture averaging performance of MISO FSO system has been investigated by means of Eq. (2.15) and Eq. (2.21), respectively. In the following, we first formulate the average power $\langle P \rangle$ and the average of the square of the power $\langle P^2 \rangle$ on the detectors by using the extended Huygens–Fresnel principle. In this way, the power scintillation index and the aperture averaging factor are quantified on the performance of MISO FSO system. It should be noted that the following results are given based on our papers [101,102].

3.1.1 System model

We consider a MISO FSO system as illustrated in Figure 3. We assume a radial laser transmit array consisting of N Gaussian beamlets, α_s being the source size of the Gaussian beamlets, i.e., the beam-waist radius of each beamlet. Since the Gaussian beamlets are taken to be collimated, the beam-waist radius and the Gaussian source size are equal to each other at the transmitter plane. Beamlets are located at equi-distant from each other on a ring with radius r_0. At the receiver side, there is a finite aperture receiver with radius R_r that has a Gaussian aperture function.
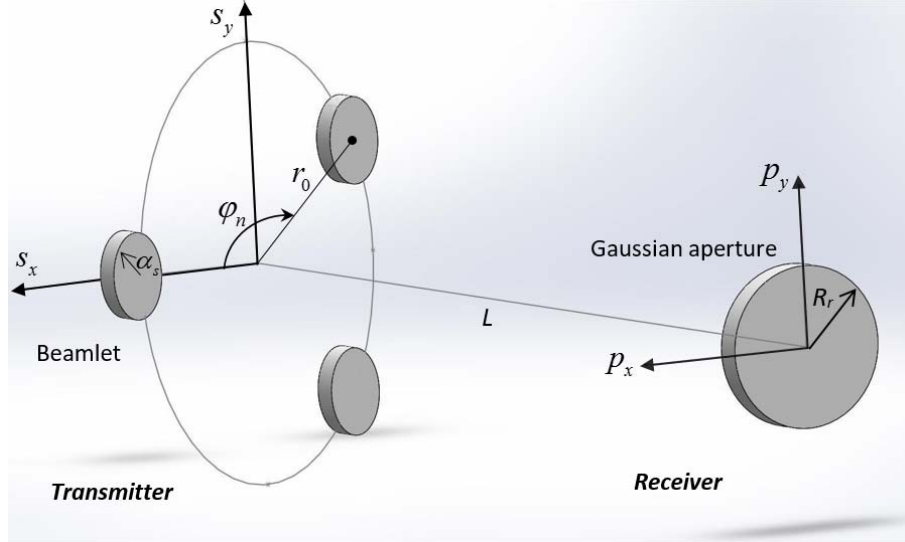
Figure 3 Schematic illustration of MISO FSO system for $N = 3$ radially located sources at the transmitter and an aperture with radius R_r at the receiver.

3.1.2 Derivation of $\langle P \rangle$ for MISO FSO system

We first calculate the average intensity at the receiver plane which is then used to calculate $\langle P \rangle$ and $\langle P^2 \rangle$. This enables us to calculate the power scintillation index and the receiver aperture averaging factor.

The source field expression for a laser array with Gaussian sources can be expressed as [90]

$$u\left(s_x, s_y\right) = \sum_{n=1}^{N} \exp\left\{-k\alpha_n \left[s_x^2 + s_y^2 - 2r_0\left(s_x \cos\varphi_n + s_y \sin\varphi_n - 0.5r_0\right)\right]\right\}, \quad (3.1)$$

where, $\alpha_n = 1/\left(2k\alpha_s^2\right)$, $\varphi_n = 2\pi\left(n-1\right)/N$. From the extended Huygens-Fresnel integral, the average intensity at the receiver plane is obtained from Eq. (2.9). Inserting Eq. (3.1) into Eq. (2.9), the average intensity can be written as

$$\langle I(\mathbf{p}, L)\rangle = \frac{1}{(\lambda L)^2} \int_{-\infty}^{\infty}\int_{-\infty}^{\infty}\int_{-\infty}^{\infty}\int_{-\infty}^{\infty} \mathbf{d}^2\mathbf{s}_1\, \mathbf{d}^2\mathbf{s}_2$$

$$\times \sum_{n=1}^{N} \exp\left\{-k\alpha_n\left[s_{1x}^2 + s_{1y}^2 - 2r_0\left(s_{1x}\cos\varphi_n + s_{1y}\sin\varphi_n - 0.5r_0\right)\right]\right\}$$

$$\times \sum_{m=1}^{M} \exp\left\{-k\alpha_m\left[s_{2x}^2 + s_{2y}^2 - 2r_0\left(s_{2x}\cos\varphi_n + s_{2y}\sin\varphi_m - 0.5r_0\right)\right]\right\} \tag{3.2}$$

$$\times \exp\left\{\frac{jk}{2L}\left[(\mathbf{p}-\mathbf{s_1})^2 - (\mathbf{p}-\mathbf{s_2})^2\right] - \rho_0^{-2}(\mathbf{s_1}-\mathbf{s_2})^2\right\},$$

Solving Eq. (3.2) by the repeated use of Eq. (3.323.2) of [152] we obtain

$$\langle I(\mathbf{p}, L)\rangle = \frac{\pi^2}{(\lambda L)^2} \sum_{n=1}^{N}\sum_{m=1}^{M} \frac{1}{t_1^2 t_2^2} \exp\left(-r_0^2 \alpha_s^{-2}\right)$$

$$\times \exp\left(-\frac{k^2}{4t_1^2 L^2} p_x^2 + \frac{r_0^2\cos^2\varphi_n}{4t_1^2\alpha_s^4} - \frac{r_0\cos\varphi_n}{2t_1^2\alpha_s^2}\frac{jk}{L}p_x\right)$$

$$\times \exp\left(-\frac{k^2}{4t_1^2 L^2} p_y^2 + \frac{r_0^2\sin^2\varphi_n}{4t_1^2\alpha_s^4} - \frac{r_0\sin\varphi_n}{2t_1^2\alpha_s^2}\frac{jk}{L}p_y\right) \tag{3.3}$$

$$\times \exp\left(\frac{w_{2x}^2}{4t_2^2}\right)\exp\left(\frac{w_{2y}^2}{4t_2^2}\right),$$

where

$$t_1 = \left(0.5\alpha_s^{-2} - 0.5jkL^{-1} + \rho_0^{-2}\right)^{0.5}, \quad t_2 = \left(0.5\alpha_s^{-2} + 0.5jkL^{-1} + \rho_0^{-2} - t_1^{-2}\rho_0^{-4}\right)^{1/2},$$

$$w_{2x} = r_0\left(\cos\varphi_m \frac{1}{\alpha_s^2} + \cos\varphi_n \frac{1}{t_1^2\alpha_s^2\rho_0^2}\right) + \frac{jkp_x}{L}\left(1 - \frac{1}{t_1^2\rho_0^2}\right),$$

$$w_{2y} = r_0\left(\sin\varphi_m \frac{1}{\alpha_s^2} + \sin\varphi_n \frac{1}{t_1^2\alpha_s^2\rho_0^2}\right) + \frac{jkp_y}{L}\left(1 - \frac{1}{t_1^2\rho_0^2}\right),$$

The average power detected by a finite sized receiver having Gaussian aperture function is calculated from Eq. (2.16). Substituting Eq. (3.3) in Eq. (2.16) and performing the integrations, we obtain

$$\langle P \rangle = \frac{\pi^3}{(\lambda L)^2} \sum_{n=1}^{N} \sum_{m=1}^{M} \exp\left(-r_0^2 \alpha_s^{-2}\right) \frac{1}{t_1^2 t_2^2 t_p^2}$$

$$\times \exp\left[\frac{r_0^2 \cos^2 \varphi_n}{4t_1^2 \alpha_s^4} + \frac{r_0^2}{4t_2^2}\left(\cos\varphi_m \frac{1}{\alpha_s^2} + \cos\varphi_n \frac{1}{t_1^2 \alpha_s^2 \rho_0^2}\right)^2 \right] \qquad (3.4)$$

$$\times \exp\left(\frac{w_{px}^2 + w_{py}^2}{4t_p^2}\right) \exp\left[\frac{r_0^2 \sin^2 \varphi_n}{4t_1^2 \alpha_s^4} + \frac{r_0^2}{4t_2^2}\left(\sin\varphi_m \frac{1}{\alpha_s^2} + \sin\varphi_n \frac{1}{t_1^2 \alpha_s^2 \rho_0^2}\right)^2 \right],$$

where

$$t_p^2 = R_r^{-2} + \frac{k^2}{4t_1^2 L^2} + \frac{k^2\left(1 - t_1^{-2}\rho_0^{-2}\right)^2}{4t_2^2 L^2},$$

$$w_{px} = \frac{jk}{L}\left[-\frac{r_0 \cos\varphi_n}{2t_1^2 \alpha_s^2} + \frac{r_0}{2t_2^2}\left(\frac{\cos\varphi_m}{\alpha_s^2} + \frac{\cos\varphi_n}{t_1^2 \alpha_s^2 \rho_0^2}\right)\left(1 - \frac{1}{t_1^2 \rho_0^2}\right) \right],$$

$$w_{py} = \frac{jk}{L}\left[-\frac{r_0 \sin\varphi_n}{2t_1^2 \alpha_s^2} + \frac{r_0}{2t_2^2}\left(\frac{\sin\varphi_m}{\alpha_s^2} + \frac{\sin\varphi_n}{t_1^2 \alpha_s^2 \rho_0^2}\right)\left(1 - \frac{1}{t_1^2 \rho_0^2}\right) \right].$$

3.1.3 $\langle P^2 \rangle$ for MISO FSO system

The average of the square of the power as detected by a finite sized receiver having a Gaussian aperture function is found from the Eq. (2.18) after inserting the laser array beam source formula, Eq. (3.1). The derivation and the resulting expression for $\langle P^2 \rangle$ is provided in Appendix A. Thus, by inserting $\langle P \rangle$ given by Eq. (3.4) and $\langle P^2 \rangle$ given by Eq. (A.1) into Eq. (2.15), we find the power scintillation index which is plotted as a function of the MISO FSO system parameters in the following section.

3.1.4 Numerical results

In this section, numerical calculations are made by utilizing the laser beam array field given by Eq. (3.1) and the results are shown that are obtained after evaluating Eqs. (2.15) and (2.21) which simply denote the performance metrics of the power

scintillation index and the aperture averaging factor. We investigate the effects of various system parameters such as the source size, the transmitter ring radius, the number of beamlets, the structure constant and the receiver aperture radius on these performance metrics. It should be noted that the system parameters at the transverse plane are chosen within the validity range of the wave structure function which depend on $(\lambda L)^{1/2} \gg |\mathbf{s_d}| \gg l_0$ where l_0 is the inner scale of turbulence. Therefore, the inequality limits the employed beam diameters and transmitter ring diameters to physically small dimensions. The wavelength in all calculations is $\lambda = 1.55 \ \mu$m and each beamlets on the source array are taken to be collimated. We note here that beam divergence covers the finite-sized receiver aperture.

Figure 4 displays the power scintillation dependence on ring radius, for different number of beamlets. In Figure 4, the link distance is L=5000 meters, N=1, 2, 3, receiver aperture radius R_r= 5 cm. The source size is chosen half of the ring radius as $\alpha_s = r_0/2$ to prevent overlapping of the beamlet field. From Figure 4 it is seen that when the ring radius is increased, the power scintillation decreases. The power scintillation also decreases as the number of beamlets increases.
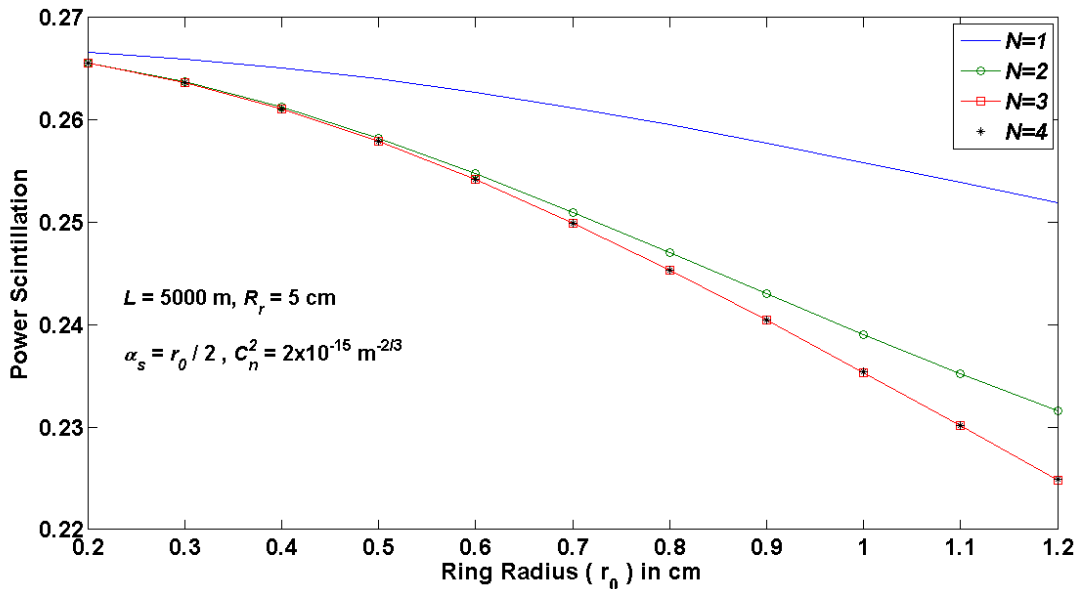
Figure 4 The power scintillation versus the ring radius r_0 assuming $L = 5000$ m, $R_r =$ 5 cm, $C_n^2 = 2 \times 10^{-15} \, \text{m}^{-2/3}$ for different number of beamlets N and the source size α_s values.

Similarly, in Figure 5 the power scintillation is analyzed by increasing the source size, but the transmitter ring radius is kept constant r_0 = 1.2 cm at this time. The other system parameters in Figure 5 are the same as in Figure 4. We observe that an increase in the source size reduces the power scintillation. We also observe that the power scintillation decreases with an increase in the number of beamlets. However, as seen in Figures 4 and 5, the power scintillation does not exhibit clear reductions when the number of beamlets larger than 3 are used.

Figure 5 The power scintillation versus the source size α_s at L = 5000 m, R_r = 5 cm, r_0 = 1.2 cm, $C_n^2 = 2 \times 10^{-15} \, \text{m}^{-2/3}$ for different N values.

Figures 6 and 7 illustrate the power scintillation variation of number of beamlets in a MISO FSO system. This way, the effects of various system parameters, i.e., source size, ring radius and the receiver aperture radius, are investigated on the performance. In both Figures 6 and 7, link distance is L=5000 m. In Figure 6, source size of each beamlets is assumed to change linearly from α_s = 0.5 cm to α_s = 0.8 cm with increments of 0.1 cm. The ring radius and receiver aperture radius are chosen as r_0 = 1, R_r = 5 cm, respectively. It is observed that as the number of beamlets increases, the power scintillation decreases. We found that by incrementing the source size of transmitter array we could obtain a reduction in the power scintillation.

It is also observed that power scintillation saturates to a different level depending on the source size when $N > 3$. Figure 7 is plotted for the cases of $R_r = 5$ cm and $R_r = 6$ cm. The transmitter ring radius is assumed to change linearly from $r_0 = 0.75$ cm to $r_0 = 1.5$ cm with increments of 0.25 cm. In addition, the source size is chosen as $\alpha_s = 0.5$ cm. It is observed from Figure 7 that an increase in the transmitter ring radius causes the power scintillation to decrease. Also, when the receiver aperture radius increases, the power scintillation decreases. The effects of the transmitter ring radius and aperture radius variations on the power scintillation are more noticeable for larger number of beamlets. Here we see the same trends of power scintillation similar to that in Figure 6.
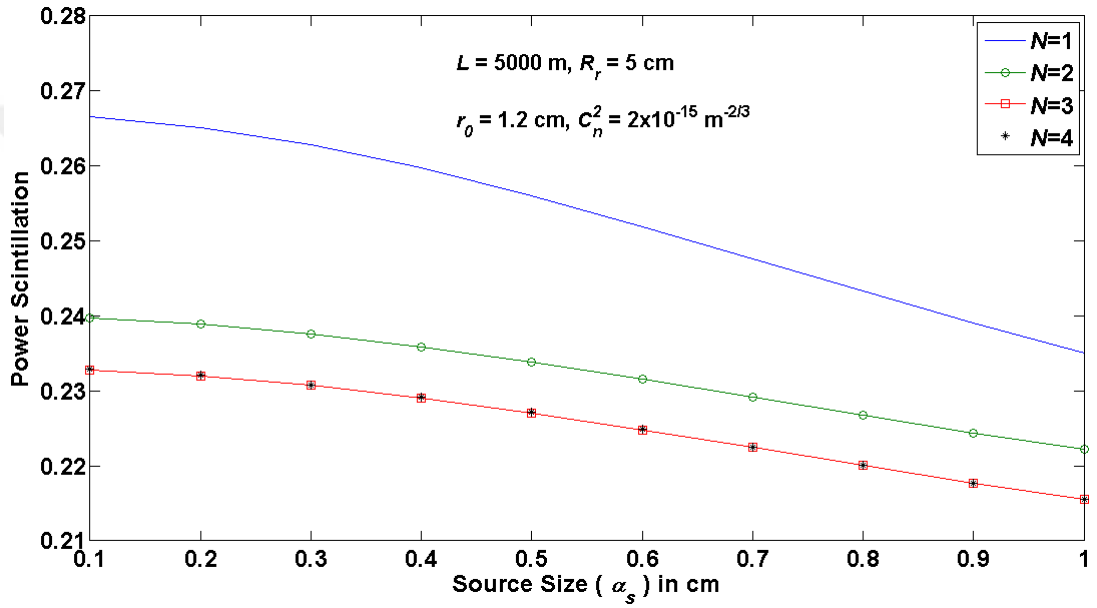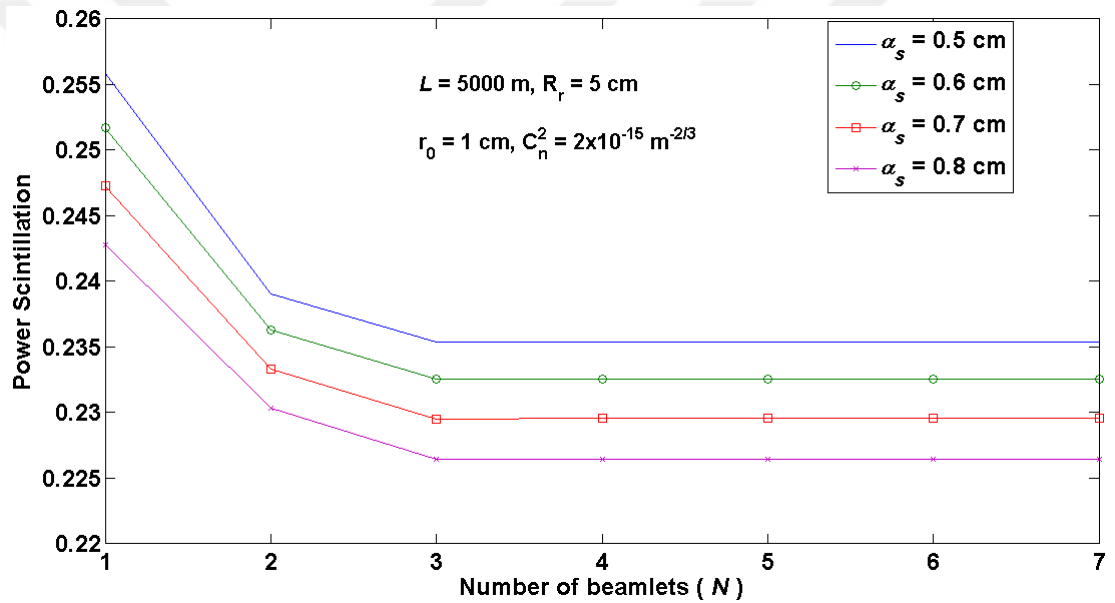

Figure 6 The power scintillation versus the number of beamlets N at $L = 5000$ m, $R_r = 5$ cm, $r_0 = 1$ cm, $C_n^2 = 2 \times 10^{-15}\,\text{m}^{-2/3}$ for different α_s values.
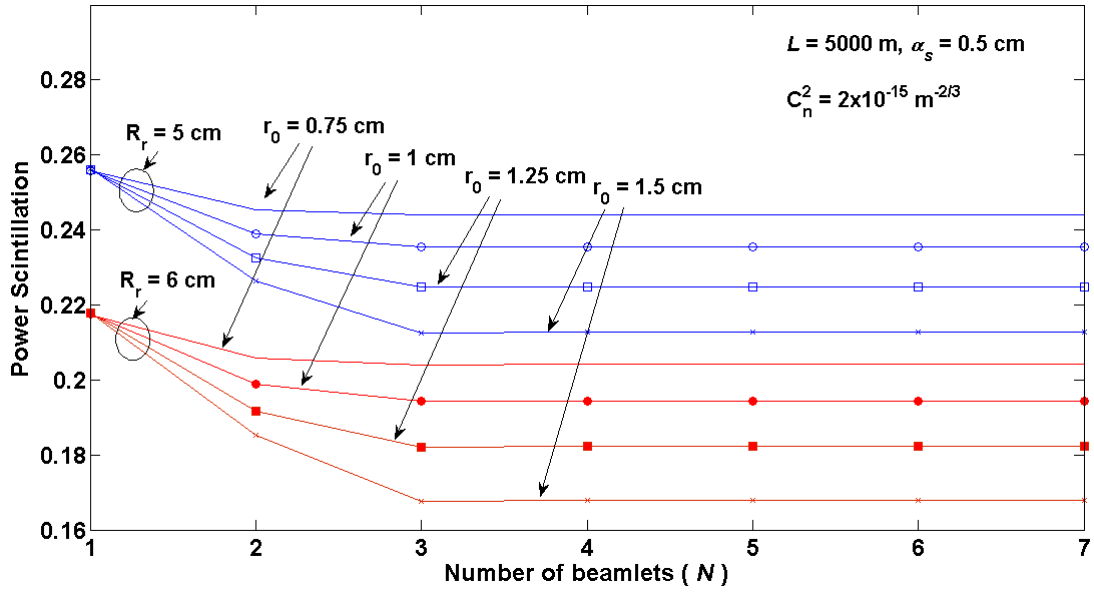
Figure 7 The power scintillation versus the number of beamlets N at $L = 5000$ m, α_s = 0.5 cm, $C_n^2 = 2 \times 10^{-15} \, \mathrm{m}^{-2/3}$ for different r_0 and R_r values.

Figure 8 shows the receiver aperture averaging factor versus the receiver aperture radius R_r for different number of beamlets each having the source size of $\alpha_s = 5$ cm. The link distance and the ring radius are chosen as $L = 5000$, $r_0 = 1$, respectively. From Figure 8, it is understood that an increase in the receiver aperture radius and the number of beamlets reduces the aperture averaging factor. This reduction is similar to the power scintillation index analyzed above for R_r, N variation. This is because, the aperture averaging factor is proportional to the power scintillation index when fixed strength of turbulence is considered.

The results shown in Figures 4-8 indicate that no additional power scintillation index advantage is gained when the number of beamlets are chosen to be greater than 3. As shown in Figures 6 and 7, the power scintillations all tend towards a low asymptotic value for different system parameters. This is due to fact that intensity variations of the received optical field which fall within the receiver aperture do saturate by adding additional beamlet in the transmit array, and thus the additional change in the scintillation is not observed.
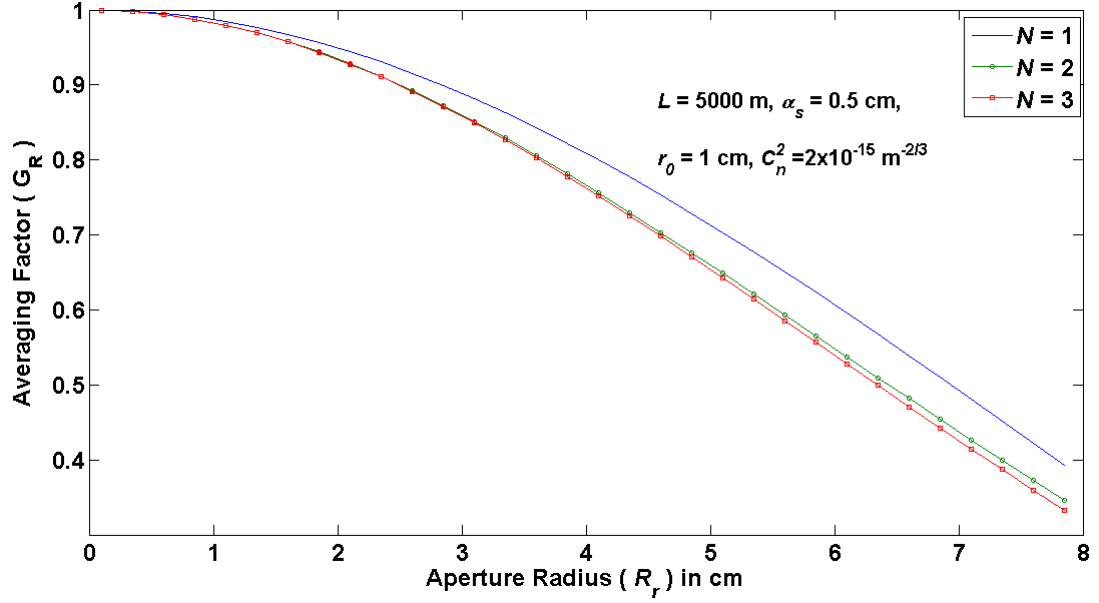
Figure 8 The receiver-aperture averaging factor G_R versus the radius of the receiver aperture R_r at $L = 5000$ m, $\alpha_s = 0.5$ cm, $r_0 = 1$ cm, $C_n^2 = 2 \times 10^{-15}$ m$^{-2/3}$ for different N values.

It should be noted that scintillation reduction is achieved with the help of the aperture averaging and the transmit diversity technique. Our derived expressions yield zero scintillation in the absence of turbulence. Naturally, aperture averaging is of no concern when there is no turbulence.

3.2 <BER> Analysis of MISO FSO Systems

In this section, by making use of our scintillation results presented in Section 3.1, we evaluate <BER> of the MISO FSO system and quantify the effects of several system parameters such as the ring radius, source size, the number of beamlets, the receiver aperture radius and the link distance on the <BER>. It should also be noted that the following results are given based on our paper [103].

3.2.1 Calculation of <BER>

By utilizing the power scintillation index evaluated in Section 3.1, the log-normal probability density function (Eq. (2.23)) is obtained and substituted into Eq. (2.22) and the resulting expression is numerically evaluated for the <BER> calculation. We

36

note that the power scintillation index m_p^2 here is published in [103] as a function of $\alpha_s, N, L, C_n^2, R_r, r_0$.

3.2.2 Numerical results

In this section, we show our numerical evaluations of Eq. (2.22) as a function of MISO system parameters. Note that, the range of validity of the wave structure function restricts the source size and the ring radius, and thus they are chosen physically small [101, 102]. According to Hufnagel-Valley atmospheric model [26], C_n^2 in general varies as a function of altitude. However, since in this section, we analyze the horizontal links, C_n^2 is taken to be constant along the link distance. In Figures 9-14, we assume wavelength $\lambda = 1.55\,\mu\mathrm{m}$ and turbulence condition, i.e., structure constant $C_n^2 = 2 \times 10^{-15}\,\mathrm{m}^{-2/3}$. We choose $\lambda = 1.55\;\mu\mathrm{m}$ because at this wavelength, atmospheric attenuation is minimum and furthermore the eye is less sensitive to light, and thus it is preferable for eye safety. We note that, in our evaluations, weak turbulence condition is satisfied when the Rytov variance for the plane wave, $1.23 C_n^2 k^{7/6} L^{11/6}$ is less than unity [26] where $k = 2\pi/\lambda$. In our results, the plane wave Rytov variances are 0.04, 0.29, 0.76 for the link distances of L=1000, 3000 and 5000 m so fulfill the weak turbulence conditions. Thus, in the <BER> evaluations, the use of the log-normal probability distribution function is justified.

Figure 9 shows <BER> variation of <SNR> for MISO FSO system with radial array Gaussian beam. In Figure 9, the link distance is L=5000 meters, N=1, 2, 3, source size of α_s=1 cm, ring radius of r_0= 1 cm and the receiver aperture radius of R_r=8 cm. As a benchmark, the <BER>s for plane and spherical wave are also provided. We notice that limiting forms of Gaussian beam lead to the plane and spherical wave by choosing the source size $\alpha_s \to \infty$ and $\alpha_s \to 0$, respectively. Figure 9 exhibits that plane and spherical waves underestimate the <BER>. Further, Gaussian beam performance is significantly better than those of plane and spherical waves. It can clearly be understood that there is little variation in <BER> as the number of spherical beamlets are chosen beyond 3. But, at a fixed <SNR>, Gaussian beam array

has favorable <BER> performance over the spherical wave array. It has been also investigated that an increase in the number of transmit apertures improves the <BER> performance slightly. To achieve a <BER> of 10^{-9}, the required <SNR>s are ~15.1 and ~15.3 dB, respectively for N=3 and 2 and this rises to ~15.6 dB for the SISO case (i.e., N=1). This small performance improvement at larger number of beamlets is due to the weak turbulence condition. The behavior depicted in Figure 9 agrees with the known results [90, 94]
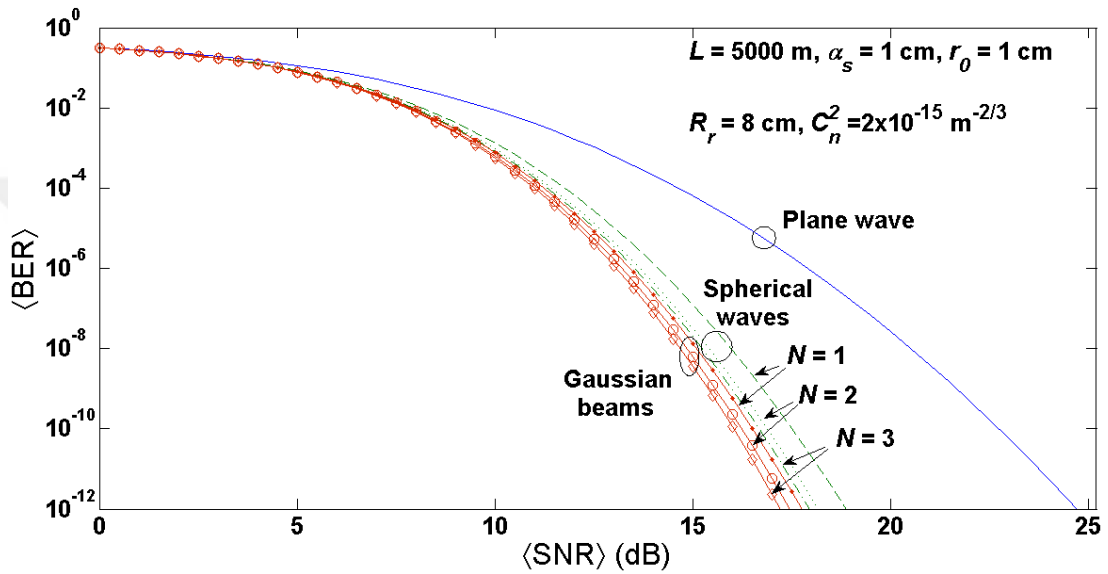
Figure 9 <BER> comparison for plane, spherical and Gaussian waves.

The effect of system parameters on <BER> is discussed by considering Gaussian beam wave assumptions in the following analysis. In Figure 10, we demonstrate the joint effect of aperture averaging and transmit diversity on <BER>. Specifically, we assume the link distance of L = 5000 meters, the ring radius of r_0 = 1 cm, the source size of α_s = 0.5 cm and, investigate the variation of <SNR> on <BER> for different number of beamlets N and various values of receiver aperture radius R_r. It is found that to achieve a <BER> of 10^{-9}, the required <SNR>s are 14.1, 14.6 and 15.1 dB, respectively for N=3 and 2 and 1 at R_r = 9 cm which increase to 16.9, 17.1 and 17.6 dB, respectively for N=3, 2 and 1 at R_r = 7 and to 19.1, 19.2 and 19.6 dB, respectively for N=3, 2 and 1 at R_r = 5. Our findings explicitly demonstrates that for the targeted <BER> value, the required <SNR> values increase with a decrease in both the number of beamlets and the receiver aperture radius. It is concluded that

<BER> can be reduced by increasing the receiver aperture radius and the number of beamlets. We also note that at high <SNR> values, aperture averaging provides better <BER> performance than does the transmit diversity.
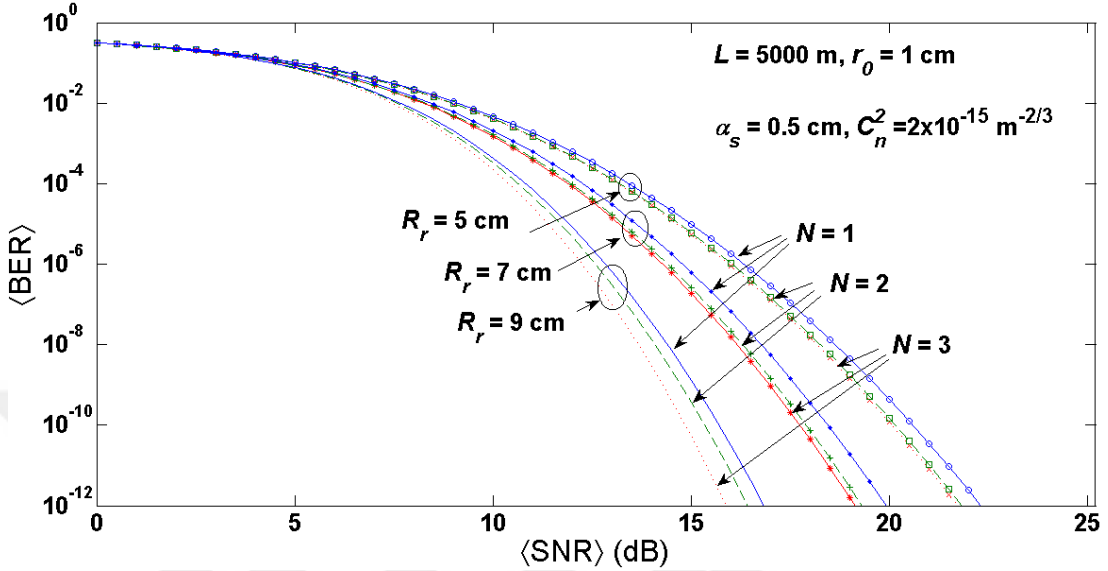
Figure 10 <BER> versus <SNR> for different R_r and N values

Next, the impact of link distance and number of beamlets on the <BER> is shown in Figure 11 where two different link distance of L = 1000 and 3000 meters are considered and the number of beamlets are taken to be N = 1, 2 and 3. The receiver aperture radius is R_r = 5 cm, the ring radius is r_0 = 1 cm and the source size is α_s = 0.5 cm. It is found that to achieve a <BER> of 10^{-9}, the required SNRs are 15.2, 16.3 and 16.7 dB, respectively for N=3, 2 and 1 at L=1000 meters which rise to 20.3, 20.6 and 21.8 dB, respectively for N=3, 2 and 1 at L=3000 meters. This clearly demonstrates that for the targeted <BER> value, the required <SNR> values increase with an increase in the link distance. The conclusion drawn from Figure 11 is that an increase in the number of beamlets reduces the <BER>. As expected, <BER> increases as the link distance increases. We also found that, the ability of N to reduce the <BER> is pronounced at longer distance.
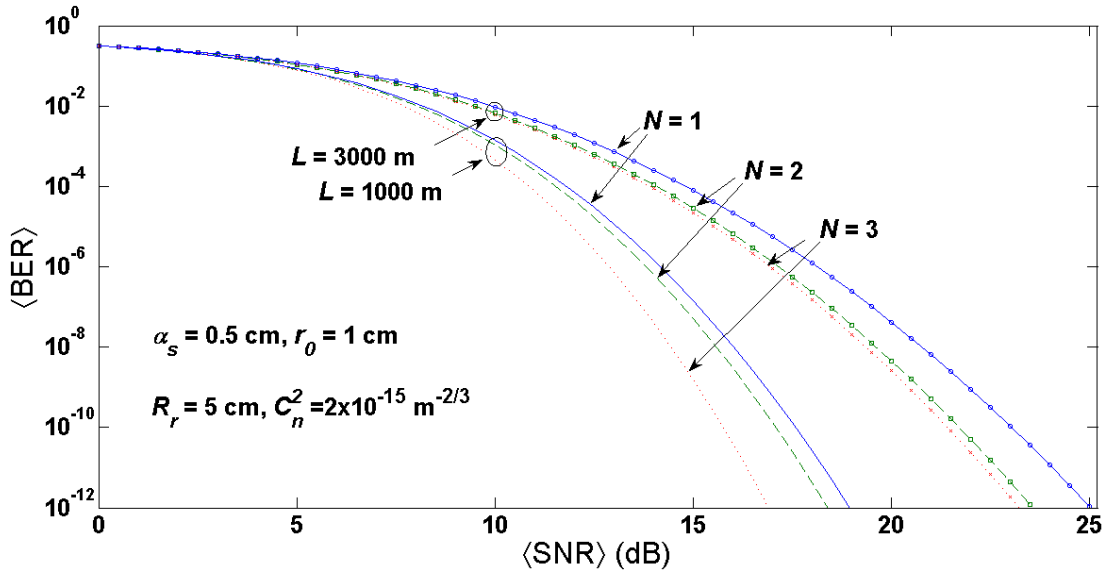
Figure 11 <BER> versus <SNR> for different *N* and *L* values

The influence of source size on <BER> performance is shown in Figure 12 for α_s=0.5 cm and α_s= 1 cm. Specifically, the link distance is taken to be *L*= 3000 m, ring radius is r_0 = 1 cm and the receiver aperture radius is R_r = 5 cm. It is found that to achieve a <BER> of 10^{-9}, the required <SNR>s are 19.3, 19.6 and 20.1 dB, respectively for *N*=3, 2 and 1 at α_s= 1 cm which rise to 20.3, 20.6 and ~21.7 dB, respectively for *N*=3, 2 and 1 at α_s=0.5 cm. This clearly explains that for the targeted <BER> value, the required <SNR> values increase with a decrease in the source size. Note in Figure 12 that the source size has a negligible effect on <BER> under low <SNR> values. However, at high <SNR> values, a larger source size causes the <BER> to decrease.
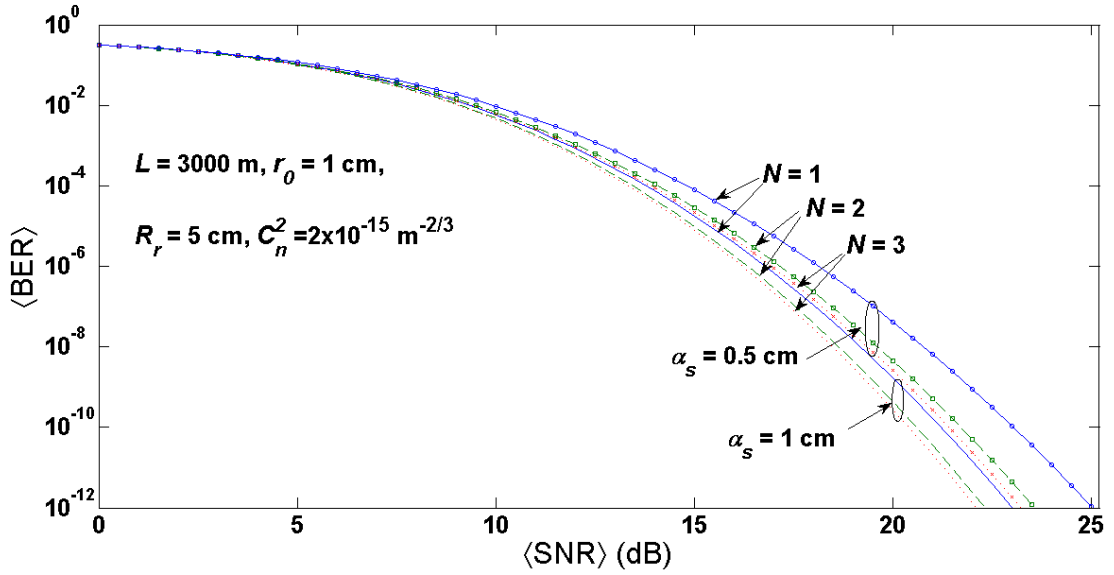
Figure 12 <BER> versus <SNR> for different α_s and N values

In Figures 13 and 14, the influence of transmitter ring radius on <BER> performance is analyzed in two ways. We first show the <BER> versus the mean <SNR> for the case of N=3 with different r_0 values. Next, we illustrate the variation of the <BER> versus the number of transmitter beamlets N for different <SNR> values. In both Figures 13 and 14, link distance is L=3000 m, the source size and the receiver aperture radius are chosen as α_s = 0.5 cm, R_r = 5 cm, respectively. It is found that to achieve a <BER> of 10^{-9} in Figure 13, the required <SNR>s are 19.1, 19.3, 19.6, 19.9, 20.1 and 20.3 dB, respectively for r_0 = 1.5, 1.4, 1.3, 1.2, 1.1 and 1. This explicitly illustrates that for the targeted <BER> value, the required <SNR> values increase with a decrease in the transmitter ring radius. It is concluded that an increase in the transmitter ring radius reduces the <BER> performance slightly. Further, it is seen in Figure 14 that an increase in <SNR> reduces the <BER> as expected. The effect of the ring radius variations on the <BER> performance is more noticeable for larger <SNR> values. Initially, there is a clear drop in <BER> and, as the number of beamlets becomes larger than 3, the <BER> variation nearly disappears.
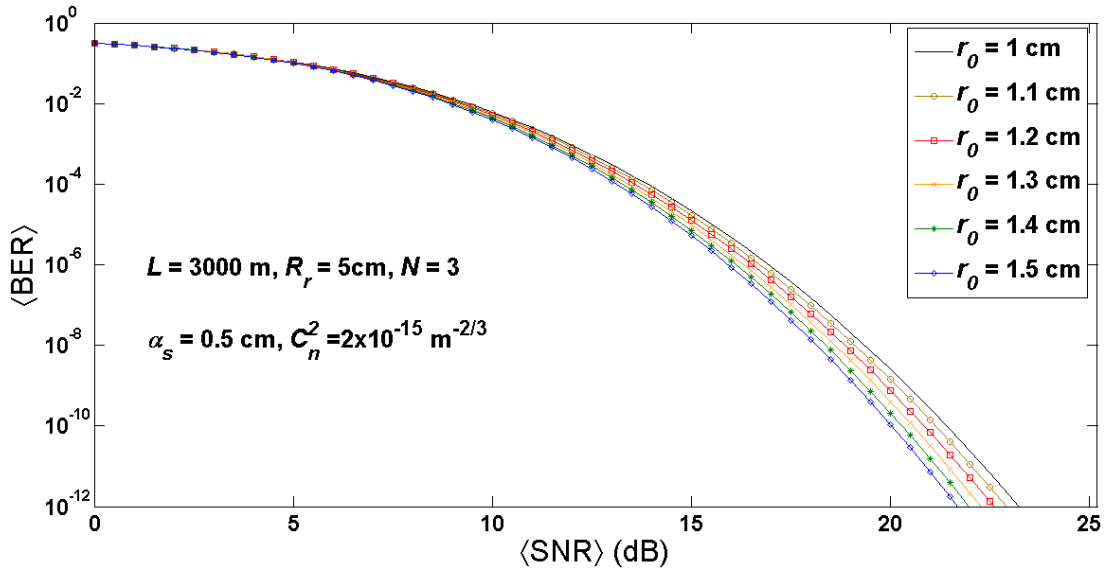
Figure 13 <BER> versus <SNR> for *N*=3 and different r_0 values.
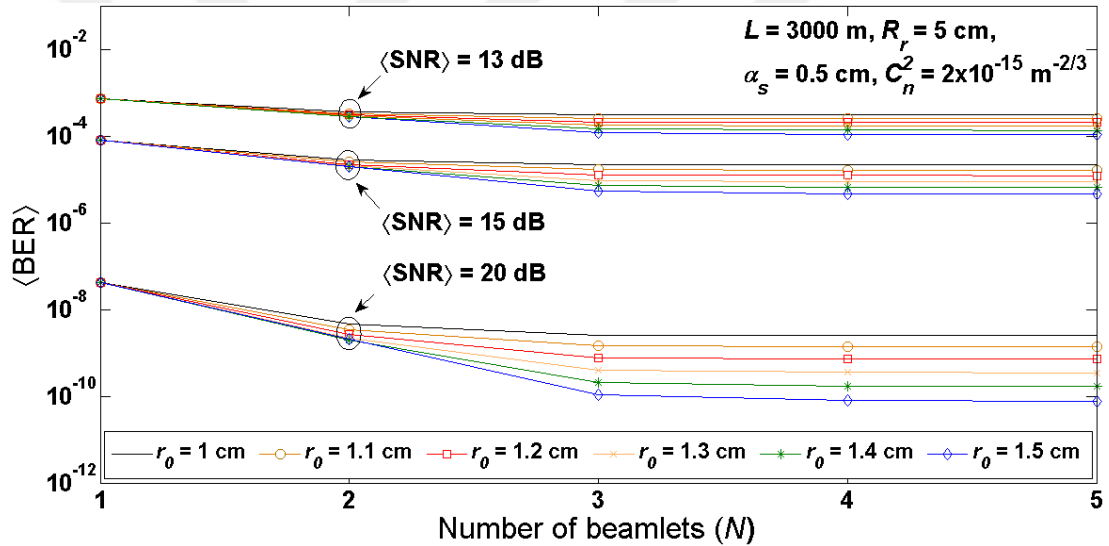
Figure 14 <BER> versus number of beamlets for different <SNR> values.

3.3 Aperture Averaging in MISO FSO Systems Using Partially Coherent Radial Array Beams

In this section, we consider an array of partially coherent Gaussian sources and a finite-sized detector at the transmitter and the receiver, respectively. The power scintillation index (Eq. 2.15) and aperture averaging factor (Eq. (2.21)) of MISO FSO system have been calculated. In the analysis, we follow the given steps provided in Section 2, but this time for the case of partially coherent laser beam array for the

transmitter in which the mutual coherence function for the source is employed. In the following, we derive expressions such as the average power $\langle P \rangle$ and power correlation on the finite-sized receiver aperture by using the extended Huygens–Fresnel principle. This enables us to calculate the power scintillation index and the receiver-aperture averaging factor. Using these calculations, we investigate the effect of several system and channel parameters on the system performance. We note that the following results are presented based on our work in [104, 105].

3.3.1 System model

The schematic diagram of the MISO FSO system model is provided in Figure 3. However, in Section 3.3, we consider a partially coherent radial laser beam array consisting of N Gaussian beamlets, which are located symmetrically on a ring with a radius of r_0. The Gaussian beamlets on the ring have equal source size α_s and equal angle separation φ_n. At the receiver side, we consider a finite sized Gaussian aperture with radius R_r.

3.3.2 Derivation of $\langle P \rangle$ for MISO FSO system using partially coherent sources

The total optical field distribution of the partially coherent laser array beam at the transmitter can be expressed as [90]

$$
\begin{aligned}
u(\mathbf{s}) &= u\left(s_x, s_y\right) \\
&= \sum_{n=1}^{N} \exp\left\{-k\alpha_n\left[s_x^2 + s_y^2 - 2r_0\left(s_x\cos\varphi_n + s_y\sin\varphi_n - 0.5r_0\right)\right]\right\} u_r\left(s_x, s_y\right),
\end{aligned}
\tag{3.5}
$$

where $u_r\left(s_x, s_y\right)$ denotes the random source field through which source partial coherence is introduced. At the receiver plane, average optical intensity distribution is found by using Huygens-Fresnel integral which is given as [88]

$$\left\langle I\left(\mathbf{p},L\right)\right\rangle = \frac{1}{\left(\lambda L\right)^2} \int_{-\infty}^{\infty}\int_{-\infty}^{\infty}\int_{-\infty}^{\infty}\int_{-\infty}^{\infty} \mathbf{d}^2\mathbf{s}_1\, \mathbf{d}^2\mathbf{s}_2\, \Gamma_2^s\left(\mathbf{s_1},\mathbf{s_2}\right)$$

$$\times \exp\left\{\frac{jk}{2L}\left[\left(\mathbf{p}-\mathbf{s_1}\right)^2 - \left(\mathbf{p}-\mathbf{s_2}\right)^2\right] - \rho_0^{-2}\left(\mathbf{s_1}-\mathbf{s_2}\right)^2\right\},$$

(3.6)

where

$$\Gamma_2^s = \left\langle u\left(\mathbf{s}_1, z=0\right) u^*\left(\mathbf{s}_2, z=0\right)\right\rangle_s$$

$$= \left\langle \sum_{n=1}^{N} \exp\left\{-k\alpha_n\left[s_{1x}^2 + s_{1y}^2 - 2r_0\left(s_{1x}\cos\varphi_n + s_{1y}\sin\varphi_n - 0.5r_0\right)\right]\right\}\right.$$

$$\times \sum_{m=1}^{N} \exp\left\{-k\alpha_m\left[s_{2x}^2 + s_{2y}^2 - 2r_0\left(s_{2x}\cos\varphi_m + s_{2y}\sin\varphi_m - 0.5r_0\right)\right]\right\}$$

$$\left.\times u_r\left(\mathbf{s}_1, z=0\right) u_r^*\left(\mathbf{s}_2, z=0\right)\right\rangle_s$$

(3.7)

$$= \sum_{n=1}^{N} \exp\left\{-k\alpha_n\left[s_{1x}^2 + s_{1y}^2 - 2r_0\left(s_{1x}\cos\varphi_n + s_{1y}\sin\varphi_n - 0.5r_0\right)\right]\right\}$$

$$\times \sum_{m=1}^{N} \exp\left\{-k\alpha_m\left[s_{2x}^2 + s_{2y}^2 - 2r_0\left(s_{2x}\cos\varphi_m + s_{2y}\sin\varphi_m - 0.5r_0\right)\right]\right\}$$

$$\times \left\langle u_r\left(\mathbf{s}_1, z=0\right) u_r^*\left(\mathbf{s}_2, z=0\right)\right\rangle_s,$$

In Eq. (3.7), the last line presents the Gaussian mutual coherence function for the source, which is expressed as [50]

$$\left\langle u_r\left(\mathbf{s}_1, z=0\right) u_r^*\left(\mathbf{s}_2, z=0\right)\right\rangle_s = \exp\left[-\frac{1}{4\rho_s^2}\left(\mathbf{s}_1 - \mathbf{s}_2\right)^2\right],$$

(3.8)

where ρ_s denotes the measure for the degree of source coherence level [26]. Inserting Eqs. (3.7) and (3.8) into Eq. (3.6) and solving Eq. (3.6) by the repeated use of Eq. 3.323.2 of [152], we obtain

$$\left\langle I\left(\mathbf{p},L\right)\right\rangle = \pi^2\left(\lambda L\right)^{-2} \sum_{n=1}^{N}\sum_{m=1}^{M} \frac{1}{\zeta_1^2\zeta_2^2} \exp\left(-r_0^2\alpha_s^{-2}\right)$$

$$\times \exp\left[-\frac{r_0 jk}{2\zeta_1^2\alpha_s^2 L}\left(p_x\cos\varphi_n + p_y\sin\varphi_n\right)\right]$$

(3.9)

$$\times \exp\left[-\frac{k^2}{4\zeta_1^2 L^2}\left(p_x^2 + p_y^2\right) + \frac{r_0^2}{4\zeta_1^2\alpha_s^4} + \frac{1}{4\zeta_2^2}\left(\omega_{2x}^2 + \omega_{2y}^2\right)\right],$$

where

$$\zeta_1^2 = 0.5\alpha_s^{-2} - 0.5jkL^{-1} + \rho_0^{-2} + 0.25\rho_s^{-2},$$

$$\zeta_2^2 = 0.5\alpha_s^{-2} + 0.5jkL^{-1} + \rho_0^{-2} + 0.25\rho_s^{-2} - \zeta_1^{-2}\left(\rho_0^{-2} + 0.25\rho_s^{-2}\right)^2,$$

$$\omega_{2x} = r_0\left[\alpha_s^{-2}\cos\varphi_m + \zeta_1^{-2}\alpha_s^{-2}\cos\varphi_n\left(\rho_0^{-2} + 0.25\rho_s^{-2}\right)\right]$$
$$+ jkL^{-1}p_x\left[1 - \zeta_1^{-2}\left(\rho_0^{-2} + 0.25\rho_s^{-2}\right)\right],$$

$$\omega_{2y} = r_0\left[\alpha_s^{-2}\sin\varphi_m + \zeta_1^{-2}\alpha_s^{-2}\sin\varphi_n\left(\rho_0^{-2} + 0.25\rho_s^{-2}\right)\right]$$
$$+ jkL^{-1}p_y\left[1 - \zeta_1^{-2}\left(\rho_0^{-2} + 0.25\rho_s^{-2}\right)\right],$$

The average power collected by a finite sized Gaussian aperture is found from the Eq. (2.16). Thus, by inserting Eq. (3.9) into Eq. (2.16) and performing the integrations over the receiver aperture, we obtain

$$\langle P \rangle = \frac{\pi^3}{\left(\lambda L\right)^2}\sum_{n=1}^{N}\sum_{m=1}^{M}\frac{1}{\zeta_1^2\zeta_2^2\zeta_p^2}\exp\left(-r_0^2\alpha_s^{-2}\right)$$
$$\times \exp\left[0.25\zeta_p^{-2}\left(\omega_{px}^2 + \omega_{py}^2\right) + 0.25r_0^2\zeta_1^{-2}\alpha_s^{-4}\right]$$
$$\times \exp\left\{\frac{r_0^2}{4\zeta_2^2}\left[\cos\varphi_m\frac{1}{\alpha_s^2} + \cos\varphi_n\frac{1}{\zeta_1^2\alpha_s^2}\left(\rho_0^{-2} + 0.25\rho_s^{-2}\right)\right]^2\right\} \quad (3.10)$$
$$\times \exp\left\{\frac{r_0^2}{4\zeta_2^2}\left[\sin\varphi_m\frac{1}{\alpha_s^2} + \sin\varphi_n\frac{1}{\zeta_1^2\alpha_s^2}\left(\rho_0^{-2} + 0.25\rho_s^{-2}\right)\right]^2\right\},$$

where

$$\zeta_p^2 = \frac{1}{R_r^2} + \frac{k^2}{4\zeta_1^2 L^2} + \frac{k^2}{4\zeta_2^2 L^2}\left[1 - \zeta_1^{-2}\left(\rho_0^{-2} + 0.25\rho_s^{-2}\right)\right]^2,$$

$$\omega_{px} = \frac{jk}{L}\left\{-\frac{r_0\cos\varphi_n}{2\zeta_1^2\alpha_s^2} + \frac{r_0}{2\zeta_2^2}\left[\frac{\cos\varphi_m}{\alpha_s^2} + \frac{\cos\varphi_n}{\zeta_1^2\alpha_s^2}\left(\rho_0^{-2} + 0.25\rho_s^{-2}\right)\right]\right.$$
$$\left.\times\left[1 - \frac{1}{\zeta_1^2}\left(\rho_0^{-2} + 0.25\rho_s^{-2}\right)\right]\right\},$$

$$\omega_{py} = \frac{jk}{L} \left\{ -\frac{r_0 \sin \varphi_n}{2\zeta_1^2 \alpha_s^2} + \frac{r_0}{2\zeta_2^2} \left[\frac{\sin \varphi_m}{\alpha_s^2} + \frac{\sin \varphi_n}{\zeta_1^2 \alpha_s^2} \left(\rho_0^{-2} + 0.25 \rho_s^{-2} \right) \right] \right.$$

$$\left. \times \left[1 - \frac{1}{\zeta_1^2} \left(\rho_0^{-2} + 0.25 \rho_s^{-2} \right) \right] \right\},$$

3.3.3 $\langle P^2 \rangle$ for MISO FSO system using partially coherent sources

The average of the square of the power as detected by a finite sized receiver having a Gaussian aperture function is found from the Eq. (2.18) after inserting the partially coherent laser array beam source formula, Eq. (3.5). The derivation and the resulting expression for $\langle P^2 \rangle$ is provided in Appendix B. This way, by inserting the average power $\langle P \rangle$ given by Eq. (3.10) and the average of the square of the power $\langle P^2 \rangle$ given by Eq. (B.3) into Eq. (2.15), we find the power scintillation index which is plotted as function of the MISO FSO system parameters in the following section. We also note that the aperture averaging factor (related to the power scintillation) is calculated by means of Eq. (2.21)

3.3.4 Numerical results

In this section, the numerical calculations are given to illustrate the variation of the power scintillation index and the aperture averaging factor versus MISO FSO system parameters. The numerical results which are obtained from our derived equations closely match the work reported in [90] (the scintillation indices of laser array beam for point detector) by setting the receiver aperture radius of $R_r = 0$. Furthermore, using our derived equations, the scintillation index values of Ref. [88] (partially coherent multiple Gaussian beam) and Ref. [89] (partially coherent off-axis Gaussian beam) can be obtained for a point detector, respectively, by setting $N=1$, $r_0 = 0$, $R_r = 0$ and $N=1$, $r_0 > 0$, $R_r = 0$. Note that the degree of source coherence describes the partial coherence features of the laser source. For instance, when $\rho_s \rightarrow \infty$, the laser source is perfectly coherent whereas if $\rho_s < \alpha_s$, the source is stated as partially coherent. Additionally, the case $\rho_s > \alpha_s$ represents that source is becoming more coherent. In

Figures 15-18, we assume the structure constant of the atmosphere is $C_n^2 = 1 \times 10^{-15} \, \text{m}^{-2/3}$. In Figures 15-21, the wavelength is assumed to be $\lambda = 1.55 \, \mu\text{m}$ and weak fluctuation conditions are satisfied by setting the system parameters $\sigma_R^2 = 1.23 C_n^2 k^{7/6} L^{11/6} < 1$ where σ_R^2 denotes the Rytov variance of the plane wave. Specifically, in Figures 15-18, $\sigma_R^2 = 0.14$, and the maximum $\sigma_R^2 = 0.74$ in Figure 19, $\sigma_R^2 = 0.44$ in Figure 20, $\sigma_R^2 = 0.76$ in Figure 21.

In Figure 15, we illustrate the power scintillation index for both coherent ($\rho_s = 100$ cm) and partially coherent source ($\rho_s = 10^{-2}$ cm) as a function of source size for various number of transmitter beamlets. We have assumed that the transmitter ring radius which is taken to be $r_0 = 2\alpha_s$ leads to good separation of beamlet fields on the transmitter plane (non-overlapped beamlet fields). The conclusion drawn from Figure 15 is that an increase in the source size of partially coherent beam reduces the power scintillation index, whereas for the coherent beam the power scintillation increases as the source size becomes larger. It should be noted that as the number of partially coherent source in the transmit array increases, the power scintillation decreases. But, there is little variation in the power scintillation for the source size from 0 to 10 cm, whereas for the coherent source in the transmit array, the power scintillation increase with an increase in the number of beamlets and source size. An interesting point to note is that the largest and the smallest power scintillation for coherent source are obtained for $N=1$ and $N=2$, respectively, while the graph for $N = 3$ is observed between the other two. In fact, this is due to the diffraction and configurations of laser array beams and the size of receiver aperture. For example, partially coherent source array spreads (beam divergence) much more than the coherent beam in the presence of turbulence. On the other hand, this extra expansion can help fill receiver aperture area with the received optical beam. However, when coherent source array are used receiver aperture area may be half-filled which result in an increase in the power scintillation. Therefore, the power scintillation increases with an increase in the number of beamlets. The behaivor illustrated here agrees with the known results [90]. Also, detailed explanations can be found in Ref. [86].
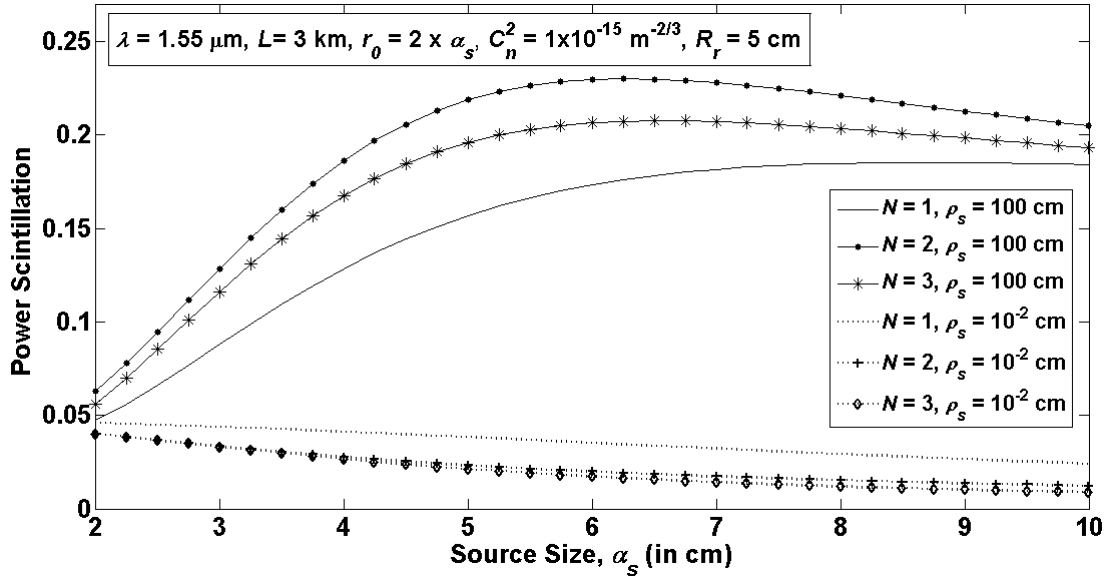
Figure 15 The power scintillation versus the source size α_s for different number of N and ρ_s values.

Similarly in Figure 16 the power scintillation is analyzed as a function of the source size for various ρ_s values. The number of beamlets in the transmit array are fixed to $N=3$. The other MISO FSO system variables in Figure 16 are kept the same as in Figure 15. We found that as ρ_s decreases, the laser source becomes to be a partially coherent source as expected, and thus a decrease in the degree of source coherence causes a decrease in the power scintillation. Variation in the power scintillation is small when ρ_s approaches the wavelength. A similar conclusion was previously reported in our earlier work [104].
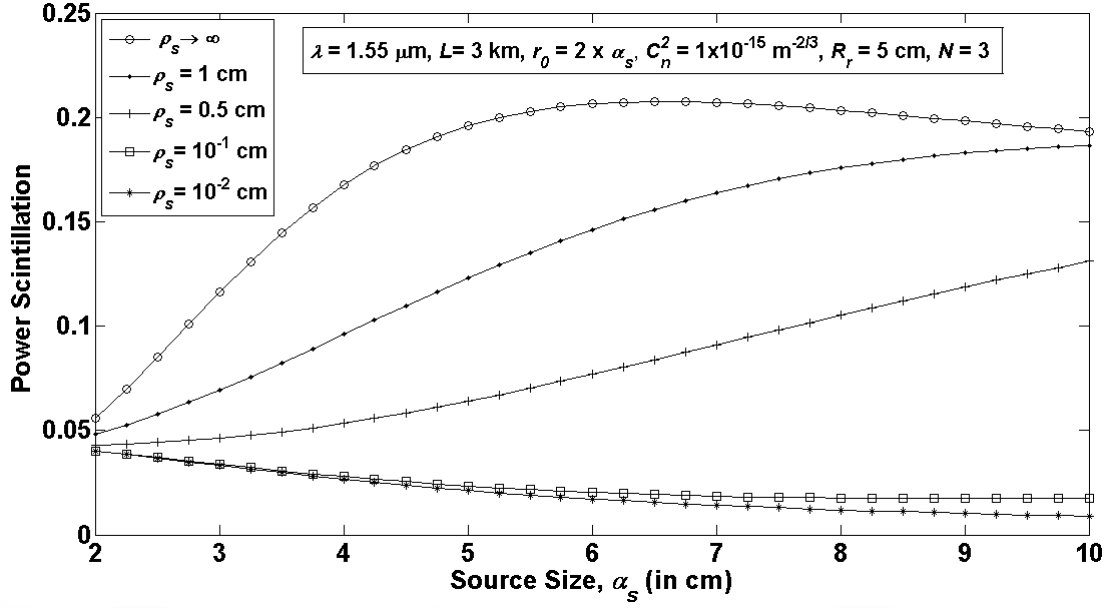
Figure 16 The power scintillation versus the source size α_s for different ρ_s values when $N = 3$.

In Figure 17, the power scintillation index for both coherent ($\rho_s = 100$ cm) and partially coherent source ($\rho_s = 10^{-2}$ cm) are plotted as a function of transmitter ring radius for various number of beamlets. The assumed link distance is $L = 3000$ m, the source size for each beamlet is $\alpha_s = 2$ cm. We also assume that receiver aperture radius of $R_r = 5$ cm. According to Figure 17, depending on the values of ρ_s, the power scintillation may decrease or increase. At a fixed length of r_0, we found that the scintillation of partially coherent MISO system is constant for $N=1$ and also minumum power scintillation is found when $N=3$ whereas for the coherent MISO system, the minumum power scintillation is obtained when $N=1$. An interesting point to note from these results is that beam divergence of the coherent source array is physically small with respect to partially coherrent source array. Therefore it experiences less beam spreading, and thus half-filled receiver aperture area which results in performance degradation. Nonetheless, beam divergence further depends on the source size. For this reason, the source sizes in the transmit array are taken to be physically small in Ref. [102] so as to fill the receiver aperture area with the received optical beam. However, in Figure 17, beam divergence of coherent array is small which results half-filled receiver aperture causing an increase in the power scintillation with an increase in the ring radius.
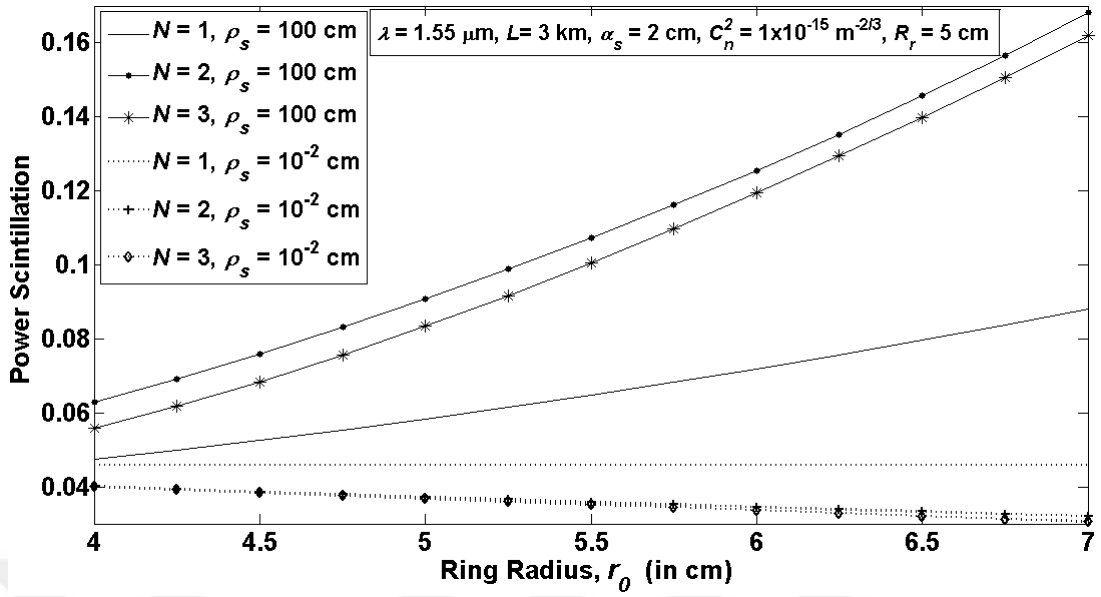
Figure 17 The power scintillation versus the ring radius r_0 for different N and ρ_s values.

In Figure 18, we plot the power scintillation index for partially coherent source ($\rho_s = 10^{-2}$ cm) as a function of receiver aperture radius R_r for various number of transmitter beamlets N and ring radius r_0 values. We find that an increase in the R_r reduces the power scintillation. At a fixed size of R_r, power scintillation begins to fall as the ring radius and the number of beamlets increase, except for N=1, which represents pointing error for the conventional SISO system and the variation of the scintillation is small due to inherent beam spreading [47]. Based on the previous results and Figure 18, it is concluded that partially coherent SISO and MISO system present favourable power scintillation performance. Further, small variation of power scintillation (approximately 0.05) is observed when MISO system is employed instead of SISO system. For this reason, partially coherent SISO system is adequate to reduce the power scintillation.

In Figure 19, the aperture averaging factor is illustrated as a function of receiver aperture radius for various structure constants. The ring radius and the number of beamlets are fixed to $r_0 = 5$ cm, N=3, respectively. The other MISO FSO system variables in Figure 19 are kept the same as in Figure 18. Note that G_R is unitless, takes values between 0 and 1 and is defined as the ratio of power scintillation (flux

50

variance) to that of a point scintillation. Due to aperture averaging effect, the power scintillation of finite sized aperture detector is generally less than that of point detector. Thus, G_r is intended to be less than 1. It is observed from Figure 19 that as the turbulence strength (structure constant of atmosphere) increases, effective averaging takes place and thus the aperture averaging factor begins to decrease.
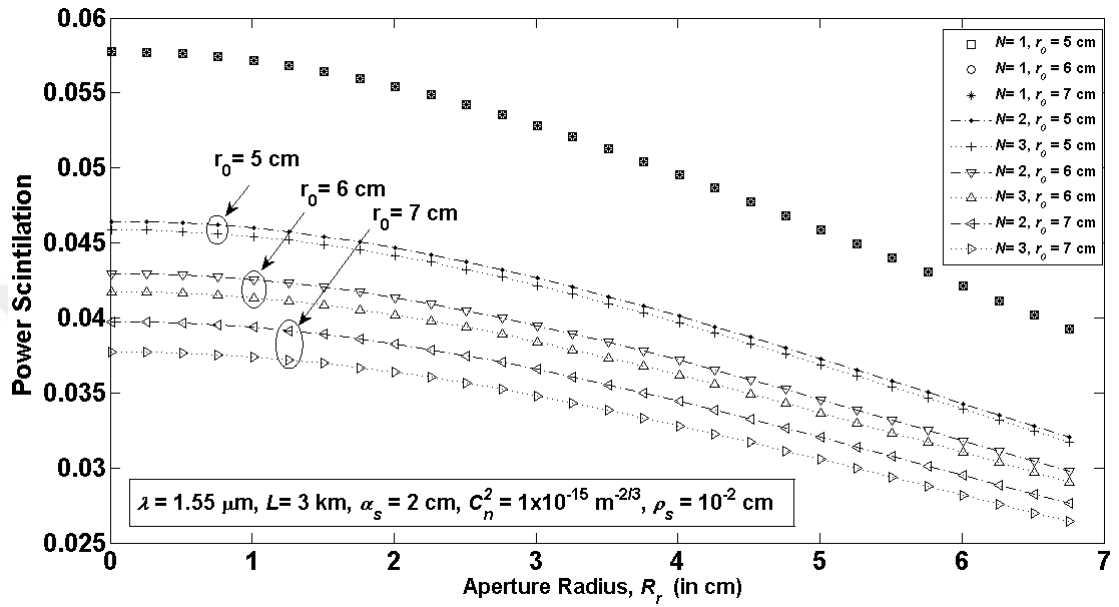
Figure 18 The power scintillation versus the receiver aperture radius R_r for different number of partially coherent beamlets N and r_0 values.
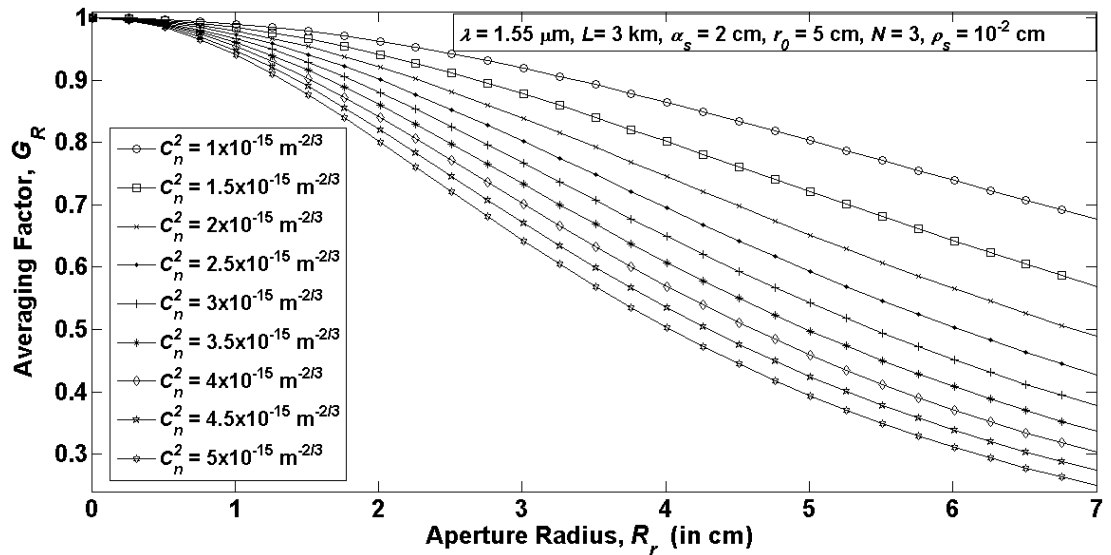
Figure 19 The receiver-aperture averaging factor G_r versus the receiver aperture radius R_r for different C_n^2 values when $\rho_s = 10^{-2}$ cm.

Figure 20 demonstrates the power scintillation as a function of number of beamlets. Additionally, the power scintillation is analyzed for several ring radius and structure constants. It is assumed that transmitter array consists of partially coherent sources with degree of $\rho_s = 10^{-2}$ cm we found that the power scintillation increases with an increase in the structure constant. On the other hand, effective reduction occurs when N and r_0 increase. We also found that the power scintillation initially drops, then saturates (variation nearly disappears) to different levels depending on r_0 and C_n^2 values. The conclusion drawn from Figure 20 is that the partially coherent MISO system with larger ring radius provides a good reduction in the power scintillation when strength of turbulence increases.
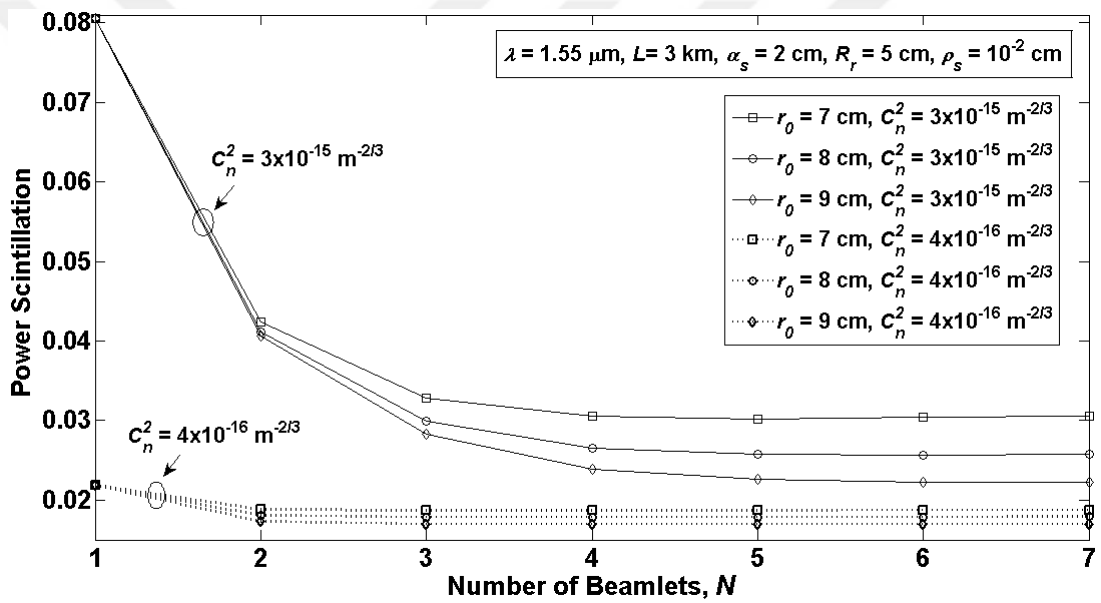
Figure 20 The power scintillation versus the number of partially coherent beamlets N for different r_0 and C_n^2 values.

Finally in Figure 21, the effects of ρ_s and L are examined on the power scintillation. The number of beamlets in the transmit array is taken to be $N = 3$. Note that the source size is fixed to $\alpha_s = 2$ cm, and thus partially coherent and coherent source are stated when $\rho_s < 2$ cm and $\rho_s > 2$ cm, respectively. As shown in Figure 21, the power scintillations initially rise, then saturate (variation nearly disappears) to different scintillation levels depending on ρ_s and L values. An increase in the link distance causes an increase in the power scintillation as expected. Variation in the link distance results in a remarkable change in the power scintillation when $\rho_s > 2$ cm.
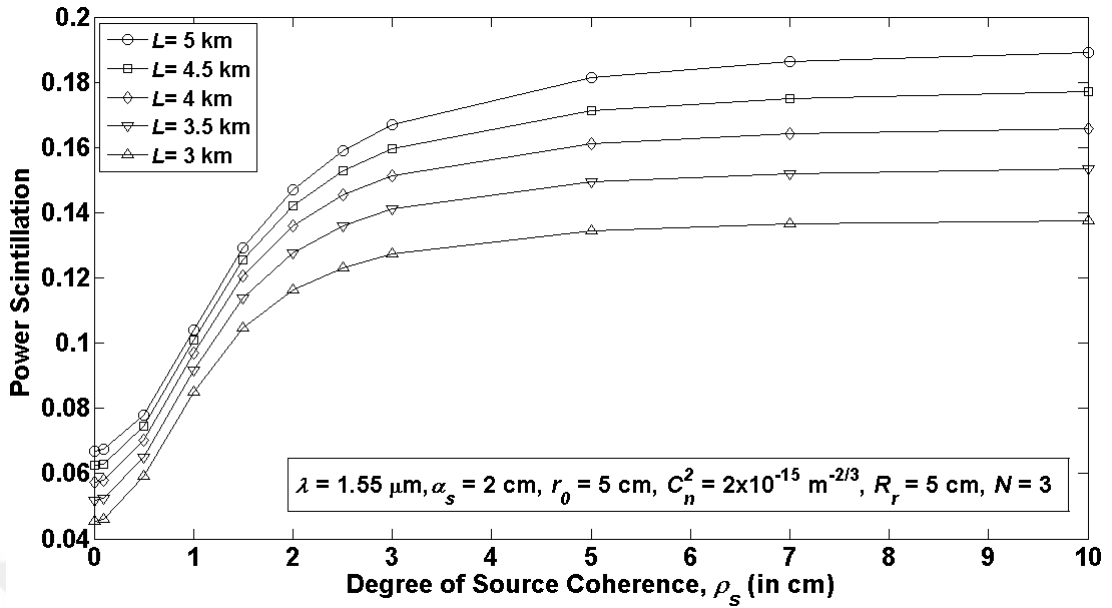
Figure 21 The power scintillation versus the degree of source coherence ρ_s for different L values.

The conclusion drawn from this study is that the use of partially coherent source can significantly reduce the power scintillation, and therefore the performance of FSO system is enhanced. In addition, the performance of MISO system is similar to that of SISO system when partially coherent beamlets are employed. This is due to the weak turbulence conditions. On the other hand, MISO system provides larger scintillation performance than SISO system when coherent beamlets are employed. As a result, this observation on MISO system is only under weak turbulence conditions and further research is required to address the improvement in the performance in moderate and strong turbulence conditions.

3.4 Performance Analysis of MIMO FSO Systems with Partially Coherent Gaussian Beams and Finite-Sized Detectors

In this section, we consider a MIMO FSO system, which consists of a radial laser array with partially coherent Gaussian beams at the transmitter and a detector array with Gaussian apertures at the receiver. The power scintillation index and aperture averaging factor of MIMO FSO system have been formulated by utilizing Eq. (2.15) and Eq. (2.21), respectively. In the analysis, the given steps provided in Section 3.3.2

53

are followed, but this time for the case of finite-sized detector array for the receiver in which the multi Gaussian aperture function is employed. In the following, we first formulate the average power $\langle P \rangle$ and the average of the square of the power $\langle P^2 \rangle$ on the detectors by using the extended Huygens–Fresnel principle. This let us quantify the performance metrics such as the power scintillation index, the aperture averaging factor, and the <BER> which is provided in the Eq. (2.22). It should be noted that the following results are presented in our paper [106].

3.4.1 System model

Figure 22 illustrates a schematic diagram of a MIMO FSO system model with N equal transmitters (an array of partially coherent Gaussian beamlets) and H equal receivers (an array of Gaussian apertures). We assume that beamlets are symmetrically located on the ring with a radius of r_0. Each of the Gaussian beamlets on the ring has a source size of α_s and angle separation of φ_n. At the receiver side, Gaussian apertures with size of R_r are placed on a ring having the radius of r_r with equal angle spacing φ_h.
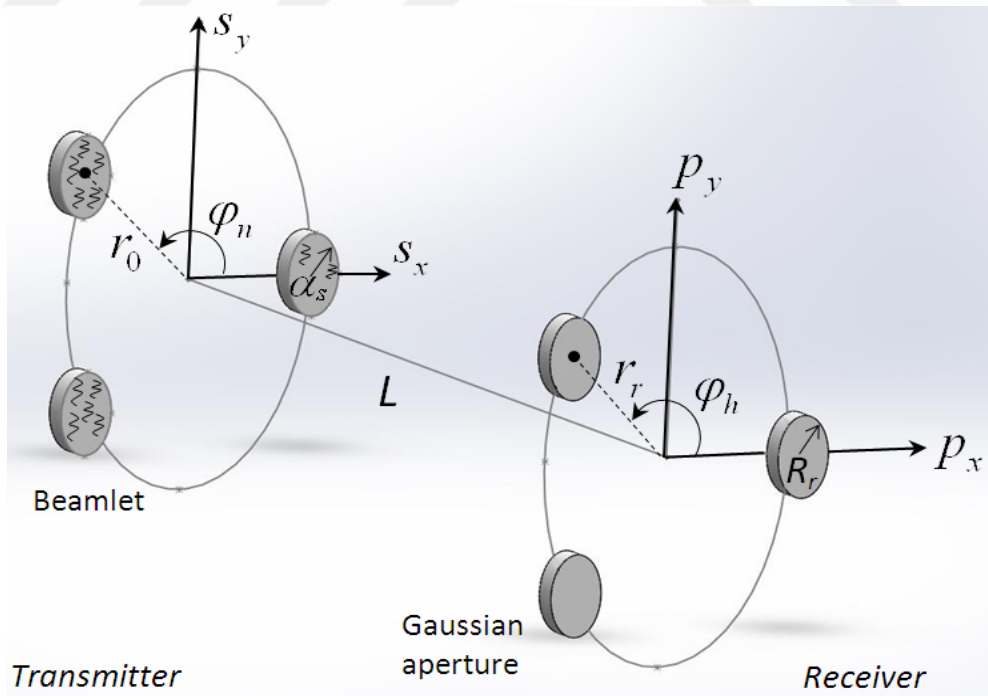
Figure 22 Schematic diagram of MIMO FSO system for $N = 3$ partially coherent beamlets at the transmitter and $H = 3$ Gaussian apertures at receiver.

3.4.2 Derivation of $\langle P \rangle$ for MIMO FSO system

The total optical field distribution at the transmitter plane for the partially coherent laser array beam is given in Eq. (3.5). Finite sized receivers, i.e., radial array of Gaussian apertures, are used to collect the optical intensity and by employing the similar expression used for the laser array at the transmitter plane [90], we defined the multi-Gaussian aperture function for the radial array at the receiver plane to be

$$h(\mathbf{p}) = \sum_{h=1}^{H} \exp\left\{ -\frac{1}{R_r^2}\left[p_x^2 + p_y^2 - 2r_r\left(p_x \cos\varphi_h + p_y \sin\varphi_h \right) + r_r^2 \right] \right\}, \quad (3.11)$$

where $\varphi_h = 2\pi(h-1)/H$. SISO, MISO, SIMO and MIMO systems can be described respectively as (N=1, r_0=0 & H=1, r_r=0), (N>1, r_0>0 & H=1, r_r=0), (N=1, r_0=0 & H>1, r_r>0) and (N>1, r_0>0 & H>1, r_r>0), respectively. The average intensity at the receiver plane resulting from the partially coherent source array is given in Eq. (3.9) which will be used to calculate the total average power $\langle P \rangle$ and the average of the square of the power $\langle P^2 \rangle$ on the detector array. This enables us to calculate the power scintillation index, the receiver-aperture averaging factor and the average bit error rate. The average power collected by a finite sized multi Gaussian aperture is found from the Eq. (2.16). Thus, by inserting Eq. (3.9) and Eq. (3.11) into Eq. (2.16) and performing the integrations over the receiver aperture, we obtain

$$\begin{aligned}
\langle P \rangle &= \frac{\pi^3}{(\lambda L)^2} \frac{1}{\zeta_1^2 \zeta_2^2 \zeta_p^2} \exp\left(-r_0^2 \alpha_s^{-2} - r_r^2 R_r^{-2} \right) \\
&\times \exp\left(\frac{r_0^2}{4\zeta_1^2 \alpha_s^4} \right) \sum_{h=1}^{H} \sum_{n=1}^{N} \sum_{m=1}^{M} \exp\left[\frac{1}{4\zeta_p^2}\left(\omega_{pmx}^2 + \omega_{pmy}^2 \right) \right] \\
&\times \exp\left\{ \frac{r_0^2}{4\zeta_2^2}\left[\cos\varphi_m \frac{1}{\alpha_s^2} + \cos\varphi_n \frac{1}{\zeta_1^2 \alpha_s^2}\left(\rho_0^{-2} + 0.25\rho_s^{-2} \right) \right]^2 \right\} \\
&\times \exp\left\{ \frac{r_0^2}{4\zeta_2^2}\left[\sin\varphi_m \frac{1}{\alpha_s^2} + \sin\varphi_n \frac{1}{\zeta_1^2 \alpha_s^2}\left(\rho_0^{-2} + 0.25\rho_s^{-2} \right) \right]^2 \right\},
\end{aligned} \qquad (3.12)$$

where

$$\omega_{pmx} = \frac{jk}{L}\left\{ -\frac{r_0\cos\varphi_n}{2\zeta_1^2\alpha_s^2} + \frac{r_0}{2\zeta_2^2}\left[\frac{\cos\varphi_m}{\alpha_s^2} + \frac{\cos\varphi_n}{\zeta_1^2\alpha_s^2}\left(\rho_0^{-2} + 0.25\rho_s^{-2}\right)\right]\left[1 - \frac{1}{\zeta_1^2}\left(\rho_0^{-2} + 0.25\rho_s^{-2}\right)\right]\right\}$$
$$+\frac{2r_r\cos\varphi_h}{R_r^2},$$

$$\omega_{pmy} = \frac{jk}{L}\left\{ -\frac{r_0\sin\varphi_n}{2\zeta_1^2\alpha_s^2} + \frac{r_0}{2\zeta_2^2}\left[\frac{\sin\varphi_m}{\alpha_s^2} + \frac{\sin\varphi_n}{\zeta_1^2\alpha_s^2}\left(\rho_0^{-2} + 0.25\rho_s^{-2}\right)\right]\left[1 - \frac{1}{\zeta_1^2}\left(\rho_0^{-2} + 0.25\rho_s^{-2}\right)\right]\right\}$$
$$+\frac{2r_r\sin\varphi_h}{R_r^2},$$

and ζ_1^2, ζ_2^2, ζ_p^2 are as previously defined in Eqs. (3.9) and (3.10).

3.4.3 $\langle P^2 \rangle$ for MIMO FSO system

The average of the square of the power as detected by a finite-sized receiver array having Gaussian apertures function is found from the Eq. (2.18) after inserting the multi-Gaussian aperture function, Eq. (3.11) and partially coherent laser array beam source formula, Eq. (3.5). The derivation and the resulting expression for $\langle P^2 \rangle$ is provided in Appendix C. Inserting the average power $\langle P \rangle$ given by Eq. (3.12) and the average of the square of the power $\langle P^2 \rangle$ given by Eq. (C.1) into Eq. (2.15), we find the power scintillation index on the detector array. In a similar manner, aperture averaging factor is obtained by using Eq. (2.21). We also note that the performance of MIMO FSO system in terms of <BER> (related to the power scintillation) can be calculated by means of the Eq. (2.22)

3.4.4 Numerical results

In this section, the numerical calculations based on Eq. (2.15), Eq. (2.21) and Eq. (2.22) are given to illustrate the variation of power scintillation index, the aperture averaging factor and the <BER> versus MIMO FSO system parameters. Note that the results reported in Ref. [88] and Ref. [90] can be obtained by invoking the change

of variables, (N= 1, r_0= 0, H=1, R_r= 0 and r_r= 0: point detector SISO), (N> 1, r_0= 0, H=1, R_r= 0 and r_r= 0: point detector MISO), respectively, in our derived equation. In Figures 23-32, the wavelength is assumed as λ= 1.55 μm and the weak fluctuation conditions are satisfied by setting the system parameters $\sigma_R^2 = 1.23 C_n^2 k^{7/6} L^{11/6} < 1$ where σ_R^2 denotes the Rytov variance of the plane wave.

In Figure 23, the employment of multiple beamlets and receiver apertures are investigated as a means to reduce the power scintillation of FSO links. For comparison, the power scintillation of MISO, SIMO and MIMO system are illustrated versus the link distance for various N and H values. As a reference, the power scintillation of conventional single-input single-output system is also given. Note that the employment of aperture averaging is performed by choosing a finite sized receiver aperture, that is, $R_r = 3$ cm. Each beamlet on the transmitter array has an equal source size of $\alpha_s = 1$ cm, and is uniformly situated on a ring having the radius of $r_0 = 2$ cm so as to have statistically independent channels. In a similar manner, receiver ring radius and receiver aperture radius are chosen as $r_r = 5$ cm, R_r = 3 cm, respectively. The structure constant is fixed to $C_n^2 = 1 \times 10^{-15}$ m$^{-2/3}$ and each beamlet is assumed to be coherent laser source $\rho_s \rightarrow \infty$. The numerical results demonstrate that for all the spatial diversities, an increase in the link distance causes an increase in the power scintillation as expected. Figure 23 reveals that powerful performance improvement is achieved by increasing both N and H. At a fixed L, MIMO system seems to be more advantageous compared to the SIMO and MISO systems. Also, as can be seen, the performance of SIMO is better than MISO for the given set of system parameters.
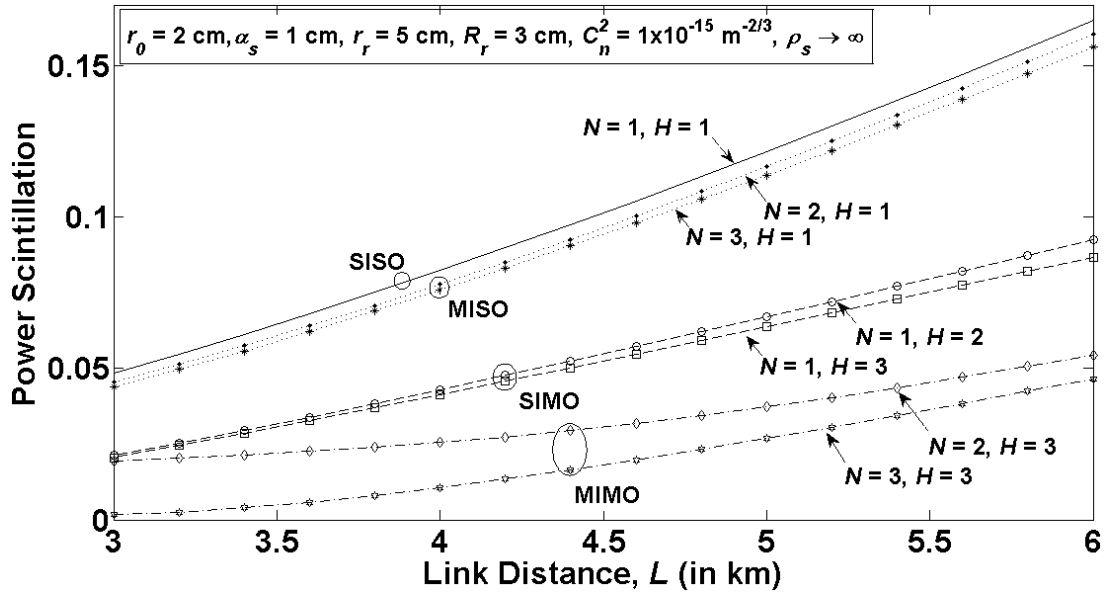
Figure 23 Power scintillation versus the link distance L for different N and H values.

The variations of power scintillation as a function of receiver aperture radius R_r are provided in Figure 24 for various N and H values where it is plotted for the same parameters as in Figure 23, except that the link distance is kept constant at $L= 5$ km. We notice from Figure 24 that the power scintillation tends to decrease with the increase of N, H and R_r values. The reduction in the power scintillation due to R_r variation is relatively small compared to the reduction in the power scintillation due to N and H values. This is because of the weak turbulence condition and the limited variation of R_r. In the comparisons shown in Figure 24, we find that performance of MIMO is greater than that of SIMO and MISO system and receiver diversity seems to be more advantages than the transmit diversity for the given set of system parameters.
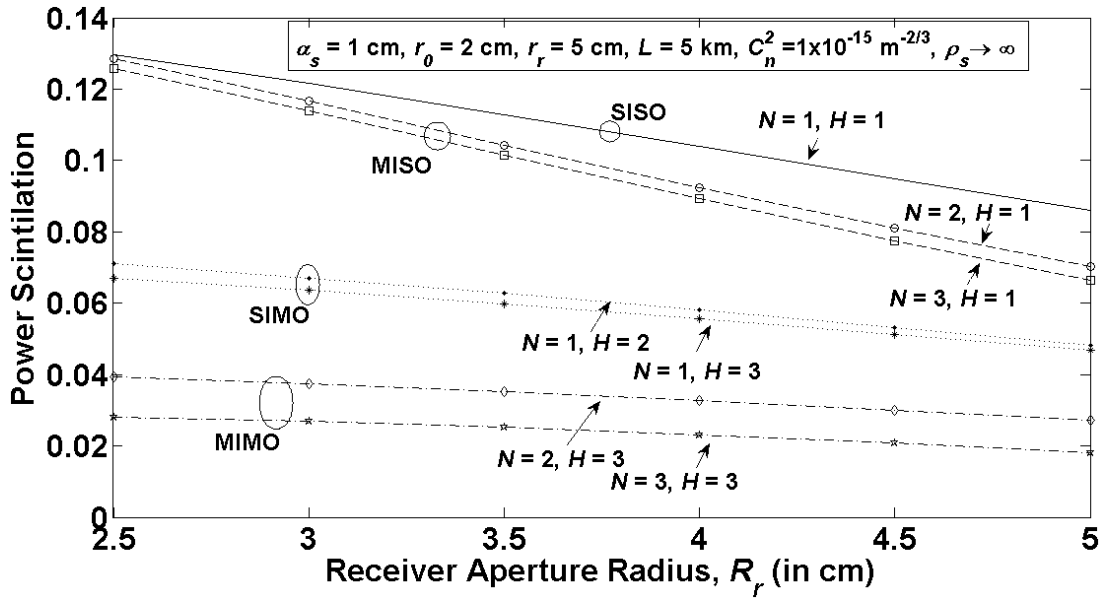
Figure 24 Power scintillation versus the receiver aperture radius R_r for different N and H values.

In Figure 25, we aimed at showing the effect of number of receiver aperture on the power scintillation. Therefore, only receiver diversity is considered by setting the system parameters as $N=1$ and $r_0 = 0$ (i.e., single Gaussian beam is placed on the axis) and each aperture on the receive array has an equal radius of $R_r = 1$ cm and uniformly situated on a ring having the radius of $r_r = 5$ cm so as to obtain minimum field correlation between receiver apertures and thus the receive diversity benefit. Further, the source size of single coherent beamlet is taken to be $\alpha_s = 1$ cm. As seen from Figure 25, the power scintillation decreases rapidly due to the increase in H, and eventually saturates at different levels depending on C_n^2 values. Variation in the power scintillation nearly disappears when the number of receiver aperture exceeds 3. The behaviours depicted in Figure 25 were also observed for MISO FSO system where 3 transmit apertures were found to be enough to saturate the power scintillation. It is also seen that the effect of H on the power scintillation is more pronounced when C_n^2 increases.
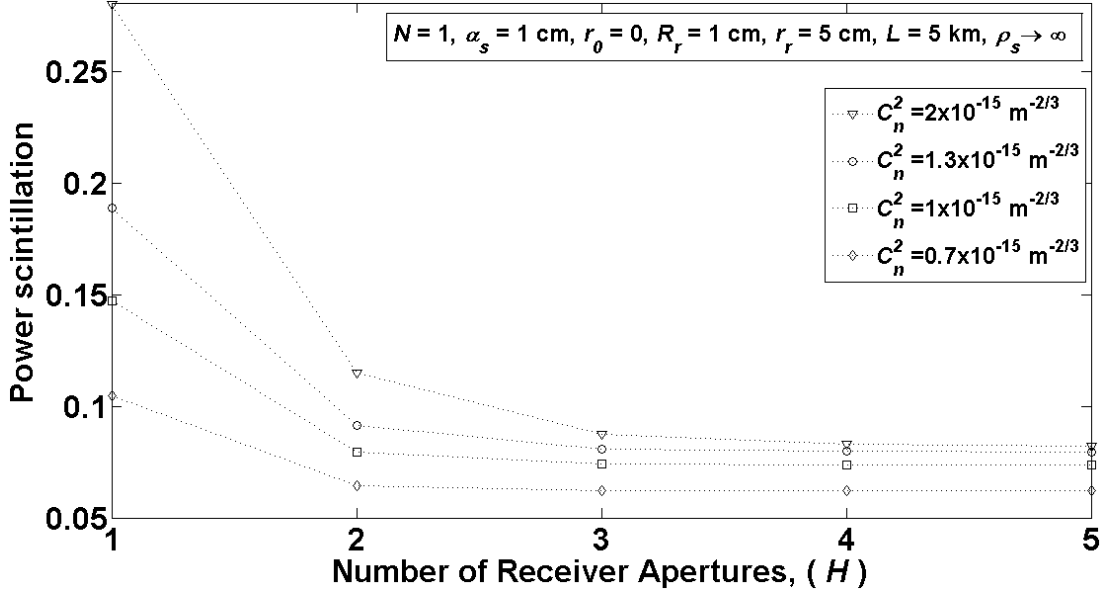
Figure 25 Power scintillation versus the number of receiver apertures *H* for different C_n^2 values.

Figure 26 is drawn for the same parameters as in Figure 25 except for *H*. We investigate the effect of the receiver ring radius r_r on the power scintillation, thus *H* is fixed to 3 and r_r is linearly increased. This way, the variation of power scintillation is illustrated as a function of r_r for different C_n^2 values. Note that when $r_r = 0$, the beamlets are overlapped but the relative distance between the receiver apertures increases with an increase in r_r. We notice from Figure 26 that as the ring radius increases, the power scintillation decreases. This can be explained by the fact that the field correlation between the receiver apertures gradually decreases with an increase in the receiver ring radius (i.e., obtaining statistically less dependent channels) which result in a decrease in the power scintillation. We also notice that the effect of r_r on the power scintillation is more pronounced for larger C_n^2.

Figure 27 is aimed at demonstrating the effect of source size variation on the power scintillation for various *N* and *H* values. We consider an array of partially coherent sources, each having the degree of source coherence value of $\rho_s = 10^{-2}$ cm. The ring radius is chosen twice that of the source size as $r_0 = 2\alpha_s$ to prevent overlapping of the beamlet field. The performance of SISO is also illustrated as a reference but to facilitate a fair comparison, the performance of SIMO system is not shown. As seen

from Figure 27, increase in the source size, meaning that the transmitter ring radius increases, results in decreased power scintillation for MISO system. In addition to this, employing multiple transmit and receive apertures (i.e., MIMO) in FSO system causes an extra reduction in the power scintillation. We notice that larger source size of MISO is enough to reduce power scintillation and there is no need to use MIMO system.
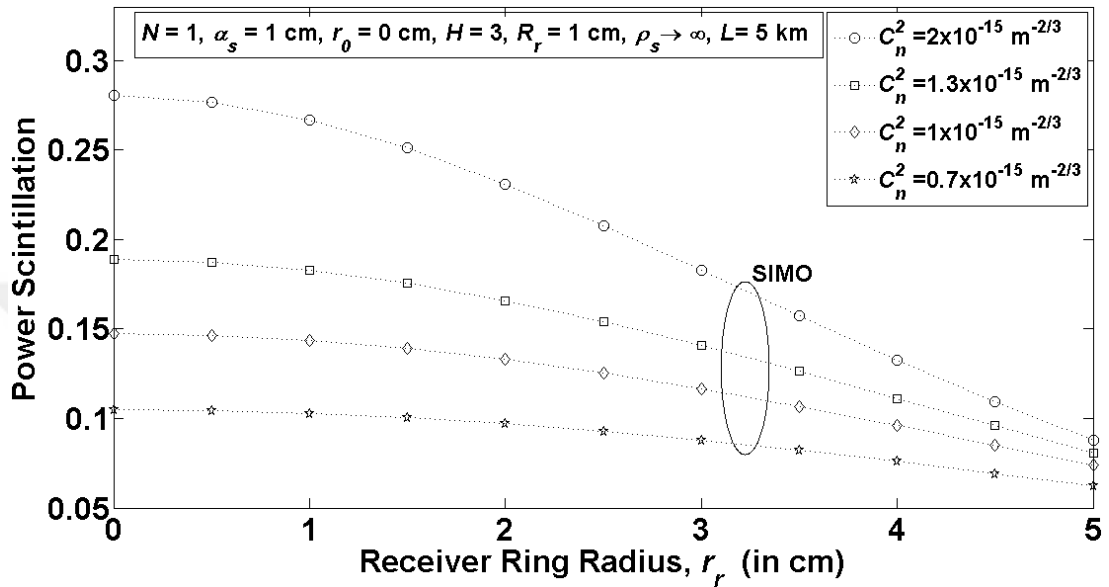
Figure 26 Power scintillation versus the receiver ring radius r_r for different C_n^2 values.
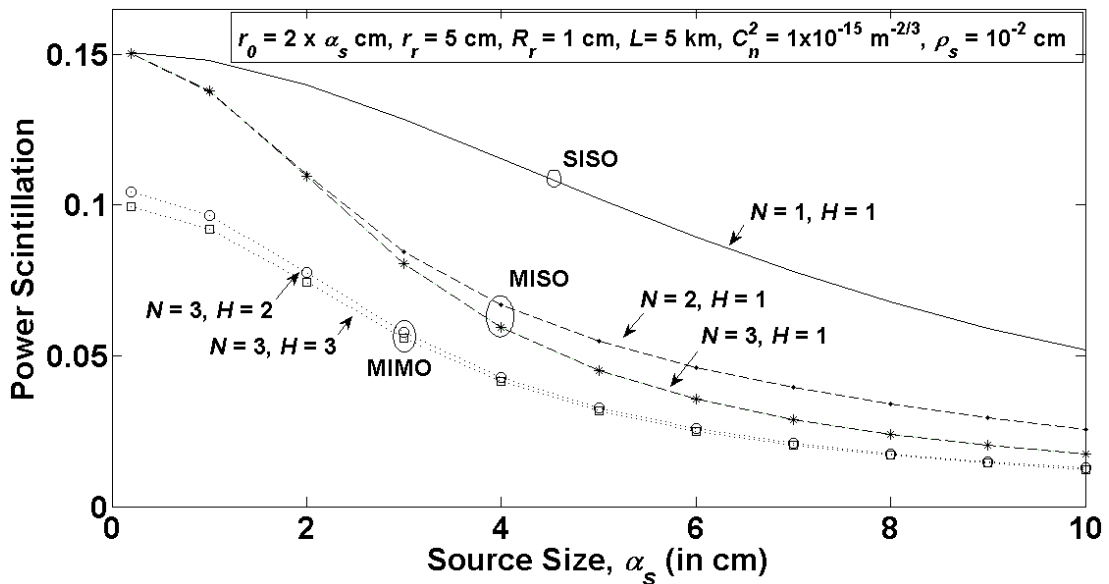
Figure 27 Power scintillation versus the source size α_s for different number of partially coherent beams N and receiver apertures H.

61

Finally, we focus on the aperture averaging factor which is defined as the ratio of the power scintillation of finite sized aperture to a point aperture on the axis. Note that G_R is unitless. Due to the averaging effect, the power scintilllation of finite sized aperture detector is generally less than that of point detector. Thus, G_r normally takes values less than 1. Figure 28 reveals that as the receiver aperture radius increases, averaging effect increases and thus the aperture averaging factor begins to decrease. Although the decrease in the aperture averaging factor is small for SIMO and MIMO system, they present better performance than that of SISO and MISO systems. This can be explained by the fact that MIMO exhibits least power scintillation for all the conditions, resulting in minimum aperture averaging factor.
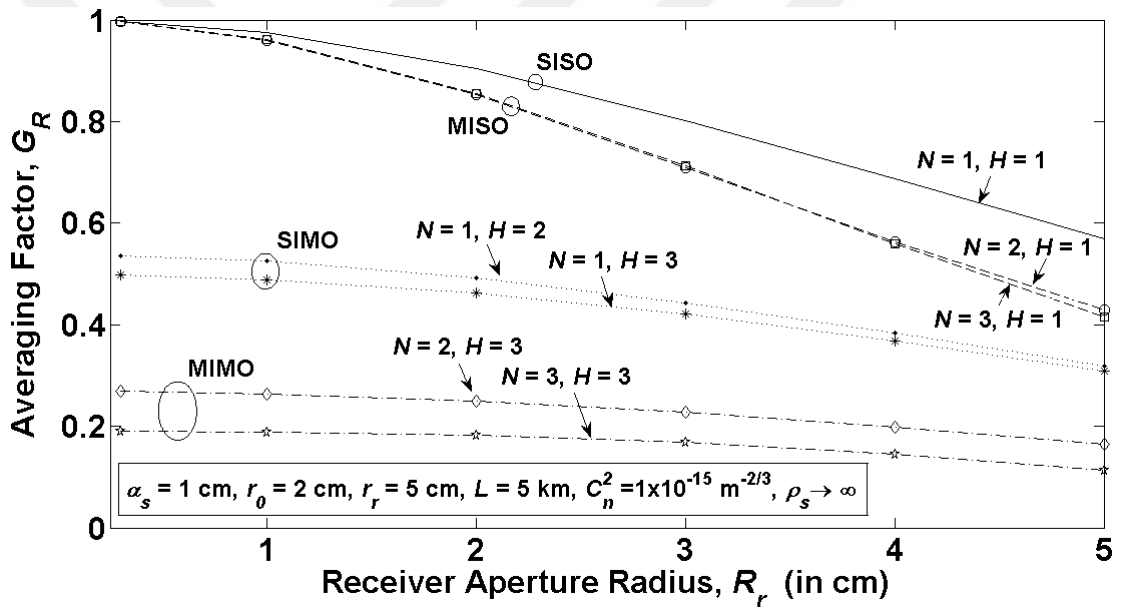
Figure 28 Receiver aperture averaging factor G_R versus the receiver aperture radius R_r for different N and H values.

In the next part of the numerical analysis, the performance of spatial diversity systems is evaluated in terms of the <BER> versus <SNR> for various system parameters. The <BER> values are numerically calculated with the help of Matlab program based on Eq. (2.22) and the corresponding power scintillation index for Eq. (2.15) are obtained from Figures 23-27. In Figures 29-32, we consider fixed structure constant $C_n^2 = 1 \times 10^{-15} \, \text{m}^{-2/3}$ and fixed link distance $L=5$ km. As a reference, the

<BER> performance of conventional single-input single-output system is also illustrated.

To demonstrate the effect of N and H on the average <BER> performance, we illustrate in Figure 29 that the plots of <BER> versus <SNR> for MISO, SIMO and MIMO systems. At the transmitter, the source size and ring radius are chosen as $\alpha_s = 1$ cm and $r_0 = 2$ cm, respectively. The beamlets in the transmit array are assumed to be coherent source ($\rho_s \to \infty$). At the receiver, aperture radius and ring radius are fixed to $R_r = 3$ cm and $r_r = 5$ cm, respectively. It is found that there is little <BER> difference as either N or H increases. However, significant <BER> reduction is observed when N and H increase together. Furthermore, performance of SIMO system is better than MISO sytem for the given set of system parameters. We also see that MIMO presents lowest <BER> performance as compared to others. To achieve a <BER> of 10^{-9}, the required SNRs are 12.4 and 12.8 dB, respectively for ($N=H=3$ and $N=2$, $H=3$) MIMO system which rises to 14.1 and 14.2 dB, respectively for ($H=3$ and 2) SIMO system and to 15.7 and 15.8 dB, respectively for ($N=3$ and 2) MISO sytem.
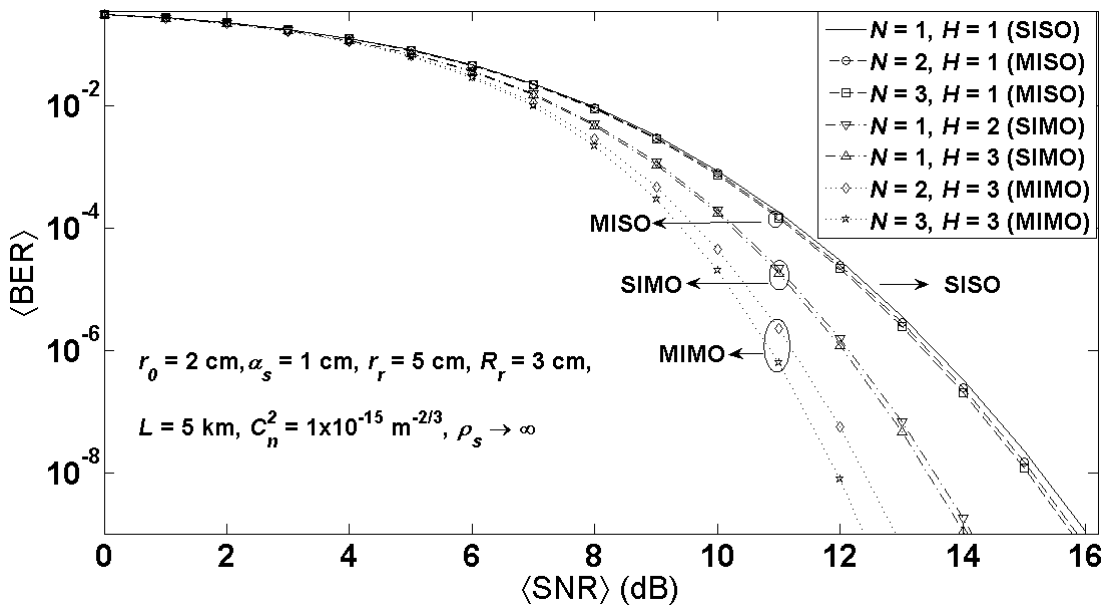
Figure 29 <BER> versus <SNR> for different N and H values.

Next, the impact of receiver ring radius r_r on the <BER> is shown in Figure 30. In Figure 30, SIMO system with α_s = 1 cm, N=1, R_r= 1 cm and H = 3 is considered. Note that the single beamlet at the transmitter is assumed to be coherent source (ρ_s →∞). It is found that when the receiver ring radius increases, the <BER> decreases. Variation in <BER> is small due to weak turbulence condition. To achieve a <BER> of 10^{-9}, the required <SNR>s are 12.5, 13.5, 14.4, 15.2 and 15.8 dB are required respectively for r_r = 7, 6, 5, 4 and 3 cm. This explains that for the targeted <BER> value, the required SNR values increase with a decrease in the receiver ring radius.
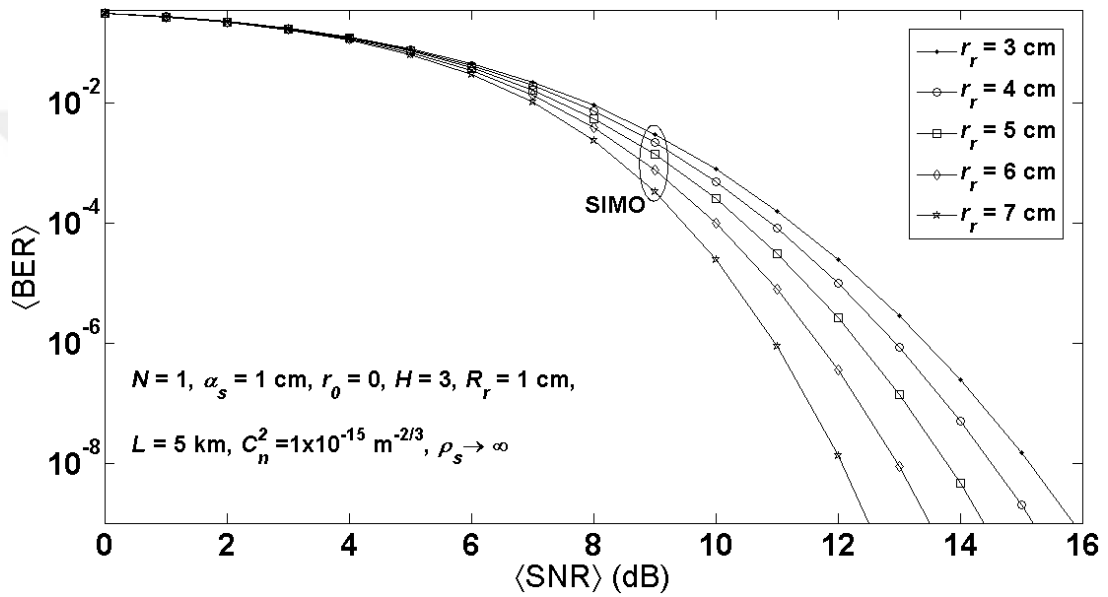
Figure 30 <BER> versus <SNR> for different r_r values.

Figure 31 is aimed at demonstrating the effect of the source size α_s on the variation of <BER> for a SIMO system which has a partially coherent source (ρ_s =10^{-2} cm) at the transmitter. We notice from Figure 31 that an increase in the source size causes a decrease in the <BER>. To achieve a <BER> of 10^{-9}, the required <SNR>s are 12.8, 13.6, 14.2, 14.8 and 15.2 dB are required respectively for α_s = 10, 7, 5, 3 and 1 cm. This clarifies that for the targeted <BER> value, the required <SNR> values increase with a decrease in the source size.

Figure 31 <BER> versus <SNR> for different α_s values of a partially coherent beam.

A comparison of MIMO performances for $N=H=2$ and 3 are further illustrated in Figure 32. Note that the performances of SISO system are given as a benchmark and were obtained by setting the system parameters as ($N=1$, $r_0=0$ & $H=1$, $r_r=0$). In Figure 32, we assume that the transmit array consists of partially coherent sources ($\rho_s =10^{-2}$ cm), each having equal source size of $\alpha_s = 1$ cm and is located on a ring with a radius of $r_0 =5$ cm. At the receiver, the ring radius is set as $r_r =5$ cm. The performances of SISO and MIMO systems are presented for two different receiver aperture radius which are $R_r =1$ and 5 cm. As seen from Figure 32, an increase in both N and H reduces the <BER> slightly. On the other hand, <BER> explicitly decreases when the receiver aperture radius increases. It is also observed that SISO system is more sensitive to changes in the receiver aperture radius. To achieve a <BER> of 10^{-9}, the required SNRs are 13.6 and 13.7 dB, respectively, for $N=H=3$ and $N=H=2$ at $R_r= 5$ cm (MIMO) which rises to 14.1 and 14.4 dB, respectively, for $N=H=3$ and $N=H=2$ at $R_r= 1$ cm (MIMO) and to 15.3 and 16.8 dB, respectively, for ($N=H=1$, $R_r= 5$cm) and ($N=H=1$, $R_r= 1$ cm) (SISO). This clarifies that for the targeted <BER> value, the required <SNR> values increase with decrease in R_r, N and H. It is concluded that the increase in R_r shows remarkable effect on the performance of <BER>.
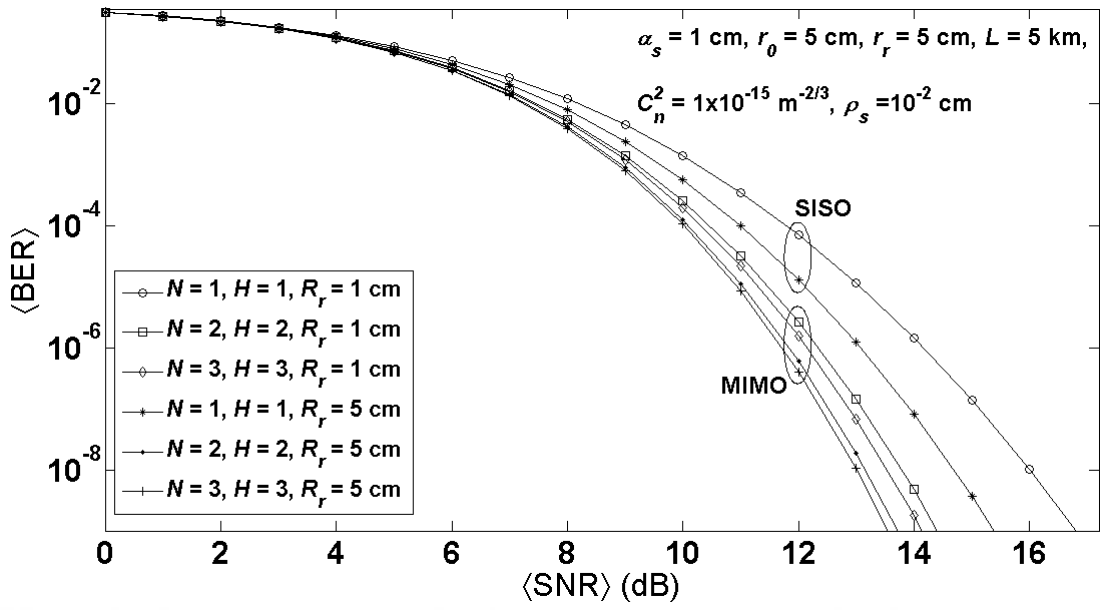
Figure 32 <BER> versus <SNR> for different partially coherent sources and number of receiver apertures, $N = H = 1$, 2 and 3.

CHAPTER 4

PERFORMANCE ANALYSIS OF TRANSMIT DIVERSITY SYSTEMS IN UNDERWATER TURBULENCE

4.1 Scintillation Analysis of MISO Underwater Optical Links

In this section, we investigate the scintillation index and the <BER> performance of MISO UWOC system employing coherent laser beam array and a point detector. The oceanic turbulence parameters have been expressed in terms of the equivalent structure constant of the atmosphere [145]. With this approach, derived formulations in Chapter 3 can be valid in both free-space optics and UWOC systems. In Section 3.1, the MISO system was employed in FSO links to reduce the scintillation effects of atmospheric turbulence, and therefore we have derived several formulations which were obtained by the Huygens–Fresnel principle. Employing the equivalent structure constant [145], existing atmospheric turbulence scintillation index formulations are redefined in this section to formulate the scintillation index in the UWOC link. In the analysis, equivalent structure constant concerned with the oceanic turbulence parameters is used in the formulations and the given steps provided in Section 2 are followed, but this time for the case of point detector for the receiver in which the point aperture is employed. In the following, we first formulate the average intensity $\langle I(L) \rangle$ and the average of the square of the intensity $\langle I^2(L) \rangle$ at the receiver's origin by using the second and fourth-order moments of irradiance (i.e., respectively $\Gamma_2(0,0,L)$ and $\Gamma_4(0,0,0,0,L)$). This lets us quantify the performance metrics such as the scintillation index and the <BER> which are given in Eq. (2.11) and Eq. (2.22), respectively. We note that the following results are published in [106].

4.2 System Model and Formation of the Scintillation

The schematic diagram of the MISO UWOC system model is given in Figure 33. Here, an array of N Gaussian laser beamlets with an equal source size of α_s is used. It is assumed that the beamlets are placed on a ring having the radius r_0 with equal angle separation φ_n. A point detector is mounted at $z=L$ meters away from the source transverse plane where z is the propagation distance.
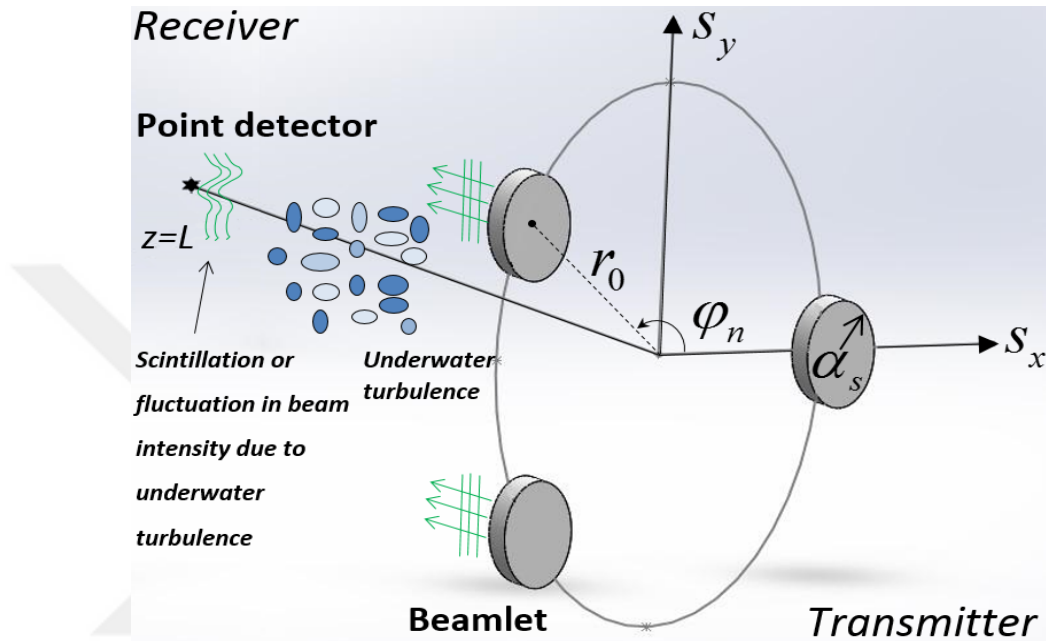
Figure 33 The illustration of MISO UWOC system with $N = 3$ and formation of the scintillation.

The optical field distribution of the laser array beam in the source plane is given in Eq. (3.1). Note that the scintillation occurs due to oceanic turbulence, mainly due to the fluctuations in the temperature and the salinity in underwater. Temperature and salinity fluctuations are characterized by turbulent eddies that are modelled by lenses of sizes ranging from the inner scale of turbulence up to the outer scale of turbulence. These lenses deflect the incident light from its initial direction, causing degradation in the wavefront of the optical beam which in turn results in the fluctuations in the received intensity. The scintillation index is a measure of the intensity fluctuations which are aimed to be reduced in a UWOC system in order to improve the link performance in underwater medium. For this purpose, in the next section, we derive the scintillation index and <BER> at the detector.

4.3 Derivation of the Scintillation Index

We have previously formulated the scintillation index and the aperture averaging factor in MISO links operating in atmospheric turbulence (see Section 3.1). The derivation here reported for the scintillation index in underwater turbulence follows similar lines as in Section 3.1 with the inclusion of the equivalent structure constant [145]. The main lines of the scintillation index formulation are here reported. In this respect, we first present the average intensity, then the average of the square of the intensity at the receiver plane in underwater turbulence, both of which are used to calculate the scintillation index at the receiver origin.

By inserting $\mathbf{p} = (p_x, p_y) = (0,0)$ into Eq. (2.9), the average intensity in underwater turbulence is presented at the receiver origin to be

$$\langle I(L) \rangle = \frac{1}{(\lambda L)^2} \int_{-\infty}^{\infty} \int_{-\infty}^{\infty} \int_{-\infty}^{\infty} \int_{-\infty}^{\infty} d\mathbf{s}_1^2 d\mathbf{s}_2^2 \; u(\mathbf{s}_1) u^*(\mathbf{s}_2)$$
$$\times \exp\left[\frac{jk}{2L} \left(|\mathbf{s}_1|^2 - |\mathbf{s}_2|^2 \right) - \rho_0^{-2} (\mathbf{s}_1 - \mathbf{s}_2)^2 \right],$$

(4.1)

where $\rho_0 = (0.546 C_n^2 k^2 L)^{-3/5}$ is the coherence length of a spherical wave propagating in the turbulent medium. Here, C_n^2 is the equivalent structure constant which has been obtained by equating the spherical wave scintillation index solutions in the oceanic and atmospheric turbulences [145]. Thus, we express the oceanic turbulence parameters by the equivalent structure constant which is given by [145]

$$C_n^2 = 16\pi^2 k^{-7/6} L^{-11/6} \, \mathrm{Re}\left\{ \int_0^L d\varsigma \int_0^\infty \kappa d\kappa \left[E(\varsigma, \kappa, L) \right. \right.$$
$$\times E(\varsigma, -\kappa, L) + \left| E(\varsigma, \kappa, L) \right|^2 \right] 0.388 \times 10^{-8} \varepsilon^{-1/3} \kappa^{-11/3}$$

(4.2)

$$\times \left[1 + 2.35 (\kappa \eta)^{-2/3} \right] \frac{\chi_T}{\omega^2} \left(\omega^2 e^{-A_T \delta} + e^{-A_S \delta} - 2\omega e^{-A_{TS} \delta} \right) \bigg\},$$

We should note that Eq. (4.2) is valid for horizontal oceanic links in which the turbulence parameters do not vary with the height. For the intensity calculation, first Eq. (4.2) is numerically evaluated and inserted into Eq. (4.1) together with the Eq. (3.1). Then, solving Eq. (4.1) at the receiver origin by the repeated use of Eq. 3.323.2 of [152], we obtain

$$\langle I(L) \rangle = \frac{\pi^2}{(\lambda L)^2} \sum_{n=1}^{N} \sum_{m=1}^{M} \exp\left[-kr_0^2 \left(\alpha_n + \alpha_m\right)\right]$$
$$\times \frac{1}{t_1^2 t_2^2} \exp\left(\frac{k^2 r_0^2 \alpha_n^2}{t_1^2}\right) \exp\left(\frac{\upsilon_{2x}^2 + \upsilon_{2y}^2}{4 t_2^2}\right),$$

(4.3)

where

$$\upsilon_{2x} = 2k\alpha_m r_0 \cos\varphi_m + \frac{2k\alpha_n r_0 \cos\varphi_n}{t_1^2 \rho_0^2},$$

$$\upsilon_{2y} = 2k\alpha_m r_0 \sin\varphi_m + \frac{2k\alpha_n r_0 \sin\varphi_n}{t_1^2 \rho_0^2},$$

and t_1^2, t_2^2 are as previously defined in Eq. (3.3).

By inserting $\mathbf{p} = (p_x, p_y) = (0,0)$ into Eq. (2.13), the average of the square of the intensity at the receiver origin is found to be

$$\langle I^2(L) \rangle = \frac{1}{(\lambda L)^4} \int_{-\infty}^{\infty}\int_{-\infty}^{\infty} d^2\mathbf{s}_1 \int_{-\infty}^{\infty}\int_{-\infty}^{\infty} d^2\mathbf{s}_2 \int_{-\infty}^{\infty}\int_{-\infty}^{\infty} d^2\mathbf{s}_3 \int_{-\infty}^{\infty}\int_{-\infty}^{\infty} d^2\mathbf{s}_4$$
$$\times u(\mathbf{s}_1) u^*(\mathbf{s}_2) u(\mathbf{s}_3) u^*(\mathbf{s}_4)$$
$$\times \exp\left[\frac{jk}{2L}\left(|\mathbf{s}_1|^2 - |\mathbf{s}_2|^2 + |\mathbf{s}_3|^2 - |\mathbf{s}_4|^2\right)\right]$$
$$\times \Gamma_4^m (\mathbf{s}_1, \mathbf{s}_2, \mathbf{s}_3, \mathbf{s}_4),$$

(4.4)

The last line of Eq. (4.4) is the fourth order coherence function of the medium which is given in Eq. (2.14). To find the average of the square of the intensity on the axis, Eq. (2.14) and (3.1) are inserted into Eq. (4.4) and solving Eq. (4.4), we obtain

$$\langle I^2(L)\rangle = \pi^4 \frac{\exp\left(4\sigma_{\chi_s}^2\right)}{(\lambda L)^4} \times \sum_{n=1}^{N}\sum_{m=1}^{N}\sum_{l=1}^{N}\sum_{o=1}^{N} \frac{1}{\beta_1^2 \beta_2^2 \beta_3^2 \beta_4^2}$$

$$\times \exp\left[-r_0^2 k\left(\alpha_n + \alpha_m + \alpha_l + \alpha_o\right)\right]\exp\left(\frac{k^2\alpha_n^2 r_0^2}{\beta_1^2}\right) \qquad (4.5)$$

$$\times \exp\left(\frac{Q_{1x}^2 + Q_{1y}^2}{4\beta_2^2} + \frac{Q_{2x}^2 + Q_{2y}^2}{4\beta_3^2} + \frac{Q_{3x}^2 + Q_{3y}^2}{4\beta_4^2}\right),$$

where

$$Q_{1x} = \frac{2\cos\varphi_n k\alpha_n r_0}{\beta_1^2 \rho_0^2} + k\alpha_m 2r_0 \cos\varphi_m,$$

$$Q_{2x} = \frac{Q_{1x}Q_4}{2\beta_2^2} - \frac{\cos\varphi_n k\alpha_n r_0 2T}{\beta_1^2} + \cos\varphi_l k\alpha_l 2r_0,$$

$$Q_{3x} = \frac{Q_{2x}Q_6}{2\beta_3^2} + \frac{Q_{1x}Q_5}{2\beta_2^2} + \cos\varphi_n k\alpha_n r_0 \frac{2}{\beta_1^2 \rho_0^2} + \cos\varphi_o k\alpha_o 2r_0,$$

$$Q_4 = \frac{2}{\rho_0^2} - \frac{2T}{\beta_1^2 \rho_0^2}, \quad Q_5 = \frac{2}{\beta_1^2 \rho_0^4} - 2R,$$

$$Q_6 = \frac{Q_4 Q_5}{2\beta_2^2} - \frac{2T}{\beta_1^2 \rho_0^2} + \frac{2}{\rho_0^2},$$

Here, Q_{1y}, Q_{2y}, and Q_{3y} are obtained by replacing all the cosine functions in Q_{1x}, Q_{2x}, and Q_{3x}, respectively, by the sine functions. β_1^2, β_2^2, β_3^2, β_4^2, T and R are as given in Appendix A.

By inserting Eq. (4.3) and Eq. (4.5) into Eq. (2.11), the on axis scintillation index detected by a point detector is found. By utilizing the scintillation index of MISO UWOC system, the log-normal probability density function (Eq. (2.23)) is obtained and substituted into Eq. (2.22) and the resulting expression is numerically evaluated for the <BER> calculation.

4.4 Numerical Results

In this section, the scintillation of MISO UWOC system based on Eq. (2.11) is investigated in terms of oceanic turbulence parameters. Similarly, the <BER> of MISO UWOC system is numerically evaluated based on Eq. (2.22) and illustrated. It should be noted that weak fluctuation conditions are satisfied by setting the system

parameters $\sigma_R^2 = 1.23 C_n^2 k^{7/6} L^{11/6} < 1$ where σ_R^2 denotes the Rytov variance of the plane wave and notice that C_n^2 denotes the equivalent structure constant (Eq (4.2)). In all the following analyses, constant source size $\alpha_s = 0.5$ cm, constant transmitter ring radius $r_0 = 1.5$ cm and constant wavelength $\lambda = 0.532$ μm are assumed unless otherwise mentioned. We note here that the range of validity of the wave structure function is restricted to the source size and the ring radius, and thus they are chosen physically small [101, 102]. Further, the wavelength of transmit lasers are chosen to be $\lambda = 0.532$ μm because minimum intensity attenuation occurs at this wavelength. It should be noted that by setting $N = 1$ and $r_0 = 0$, we obtain the scintillation index of SISO system where it can be seen in Figures 34-41 as a reference. Further, the scintillation index of MISO can be obtained by setting $N = 2$ and 3 which have an equal r_0.

In Figures 34 through 41, all the necessary link, oceanic turbulence and MISO parameters of interest are separately illustrated in the figure legends. Figure 34 shows the variation of scintillation index as a function of the ratio of temperature to salinity contributions to the refractive index spectrum ω for various number of beamlets N. As noted earlier, the temperature fluctuations dominate the underwater turbulence when $\omega = -5$ and the salinity fluctuations dominate the underwater turbulence when $\omega = 0$. Figure 34 reveals that ω does not largely affect the scintillation performance when it is small. However, the increase in scintillation is more apparent when ω approaches zero, where the reduction in scintillation due to number of beamlets N can easily be seen.

Figure 35 presents the variation of scintillation index as a function of link distance L for various number of beamlets N. The other system parameters are the same as that described for Figure 34. We notice from Figure 35 that an increase in the link distance causes an increase in the scintillation index. The reduction in the scintillation index due to multiple beamlets is more noticeable when L increases.
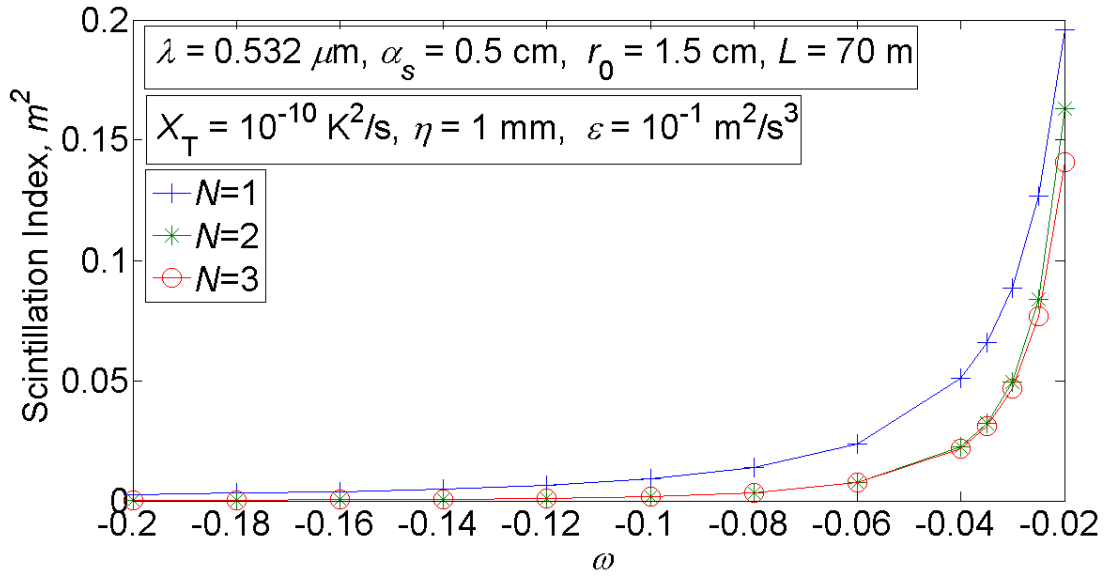
Figure 34 Scintillation index versus the ratio of temperature to salinity contributions to the refractive index spectrum ω for different N values.

Similarly in Figure 36 the scintillation index is analyzed as a function of link distance for various r_0 values. The number of beamlets in the transmit array are fixed to $N=3$. The other MISO UWOC system variables in Figure 36 are kept the same as in Figure 35. We found that as r_0 increases, the scintillation index decreases. This is due to the fact that an increase in the ring radius (i.e., relative distances between transmit beamlets) and the link distance cause a decrease in the received field correlation which in turn leads to reduction in the scintillation index at the detector. Therefore, when L increases, reduction in scintillation index due to ring radius variation is apparently seen in the Figure 36. A similar conclusion for the field correlation was previously reported by Baykal [86].
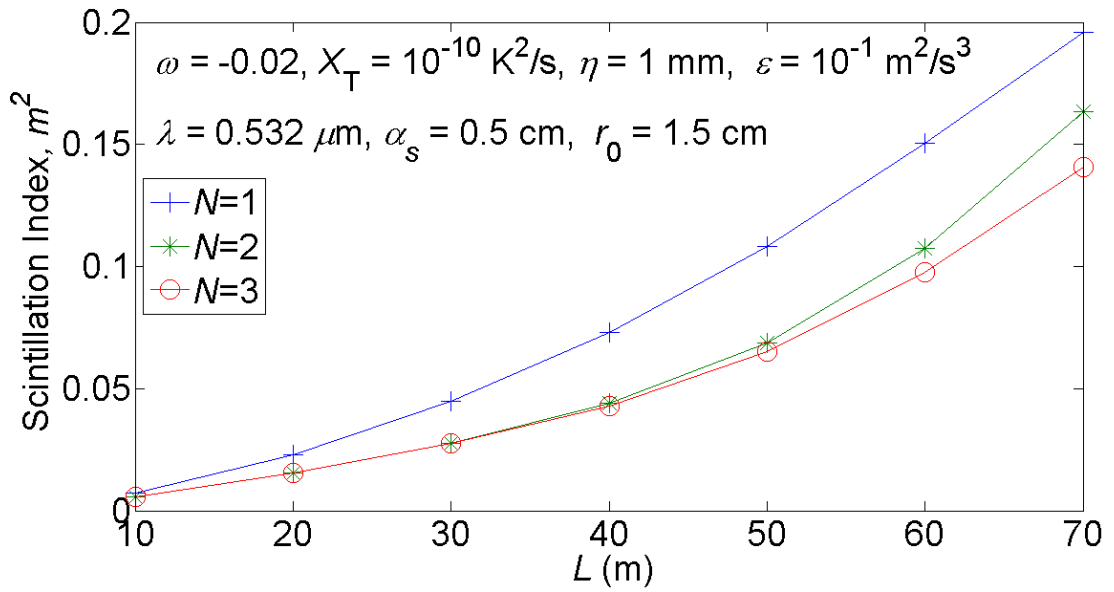
Figure 35 Scintillation index versus the link distance L for different N values.
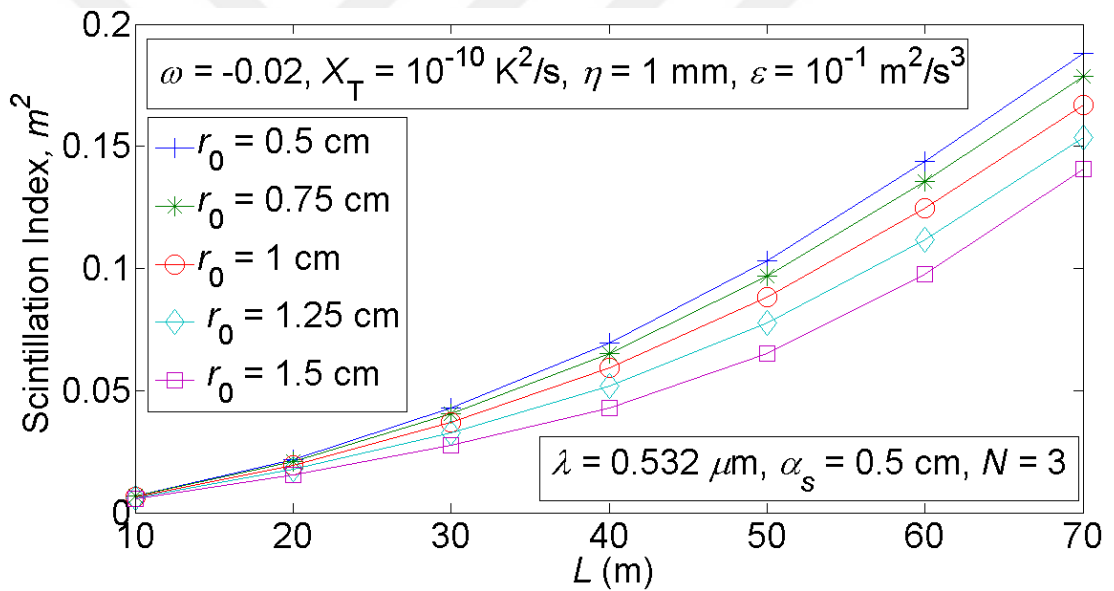
Figure 36 Scintillation index versus the link distance L for different r_0 values.

In Figure 37, the scintillation index is illustrated with respect to the rate of dissipation of the turbulent kinetic energy per unit mass of fluid ε for various number of beamlets N. Note that the link distance is fixed to $L = 50$ m. We notice from Figure 37 that the scintillation index decreases when ε increases. MISO system experiences less intensity fluctuations compared to SISO system for the given set of system parameters.

The effect of Kolmogorov inner scale η in the scintillation index is examined in Figure 38. Note that the rate of dissipation of the turbulent kinetic energy per unit mass of fluid is fixed to $\varepsilon = 10^{-1}\ \mathrm{m}^2/\mathrm{s}^3$ and the other UWOC link variables in Figure 38 are kept the same as in Figure 37. We find that as the Kolmogorov inner scale increases, the scintillation indices initially rise then saturate at different scintillation levels depending on the N values. As expected, the scintillation index decreases when N increases.
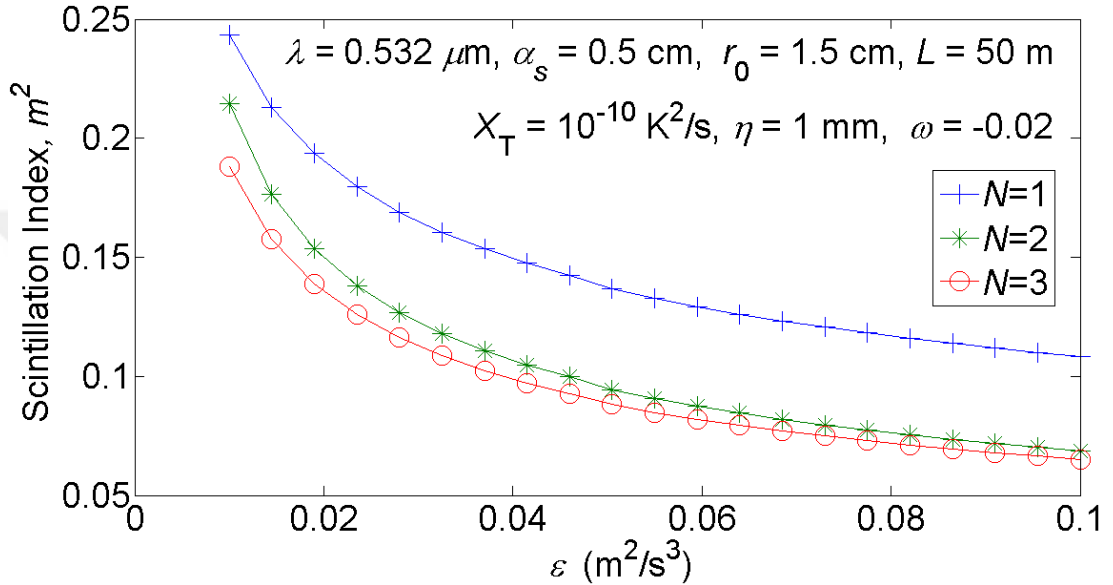
Figure 37 Scintillation index versus the rate of dissipation of the turbulent kinetic energy per unit mass of fluid ε for different N values.
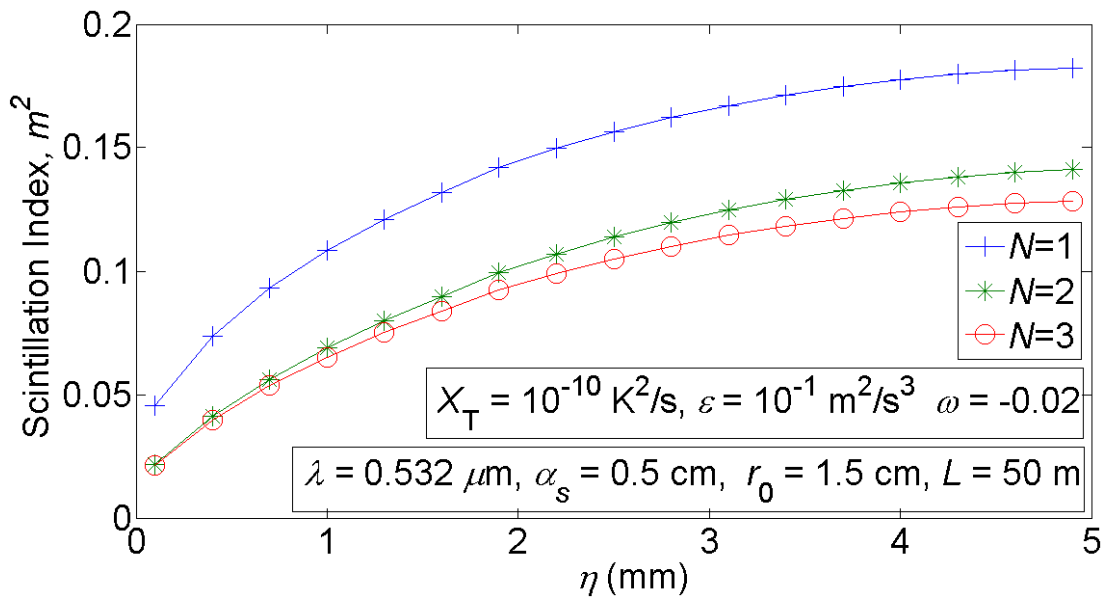
Figure 38 Scintillation index versus the Kolmogorov inner scale η for different N values.

In Figure 39, the effect of the rate of dissipation of the mean-squared temperature X_T on the scintillation index is shown for different N values. It is found that when X_T rises, the scintillation index increases. The reduction in the scintillation index due to multiple beamlets is pronounced when X_T rises.
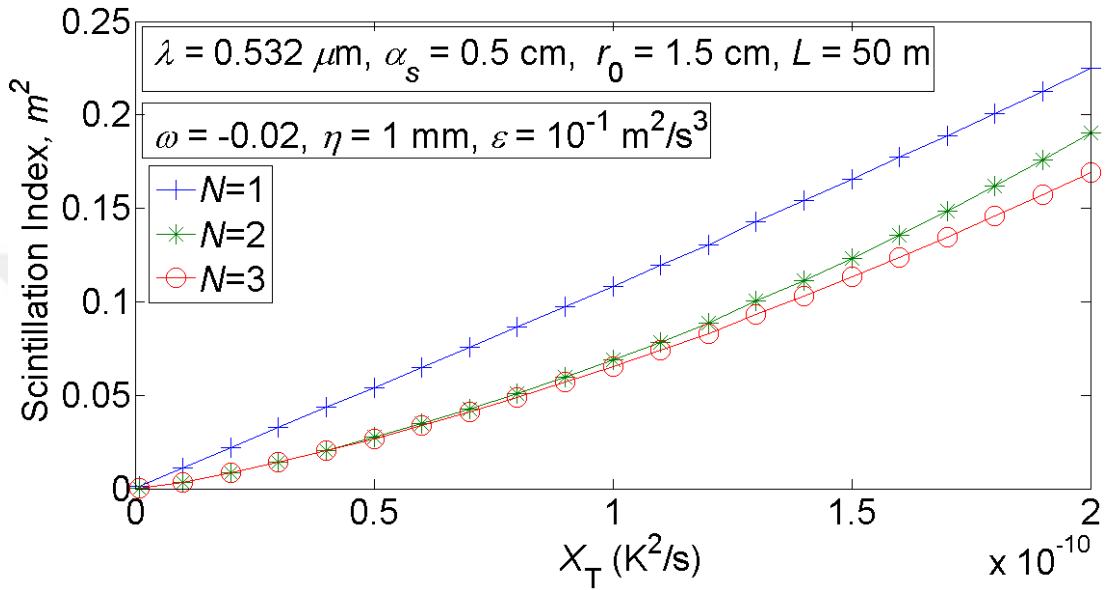
Figure 39 Scintillation index versus the rate of dissipation of the mean-squared temperature X_T for different N values.

In Figure 40, the scintillation index is plotted as a function the wavelength λ for various number of beamlets N. The rate of dissipation of the mean-squared temperature is kept as $X_T = 10^{-10} \, \text{K}^2/\text{s}$ and the other UWOC link variables are kept the same as in Figure 39. It is concluded that by incrementing the parameter N, the scintillation can be decreased. Also, increase in the wavelength of laser source reduces the scintillation index.
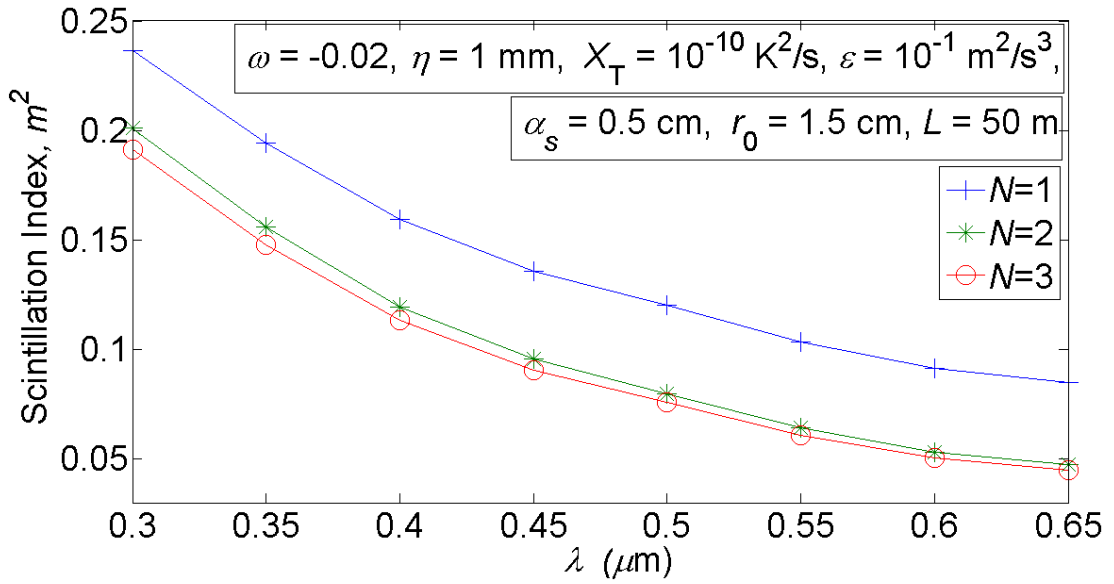
Figure 40 Scintillation index versus the wavelength λ for different N values.

Finally, the performance of the MISO UWOC system is analyzed in terms of <BER> based on the graphs of Figure 35 where the corresponding scintillation index values are taken for $N=$ 1, 2 and 3 at $L=$ 50 and 70 m. The other link variables in Figure 41 are the same as in Figure 35. This way, in Figure 41, the mean <BER> versus the mean <SNR> is illustrated for various N and L values. Note that to achieve a <BER> of 10^{-9}, the required <SNR>s are 14, 14.2 and 15.6 dB, respectively for $N=3$, 2 and 1 at $L = 50$ m which rise to 16.6, 17.2 and 18.1 dB, respectively for $N=3$, 2 and 1 at $L = 70$ m. This clearly explains that for the targeted <BER> value (10^{-9}), the required <SNR> values increase with a decrease in the number of beamlets as well as an increase in the link distance. Furthermore, <BER> decreases as the number of beamlets increases and also as the link distance decreases.
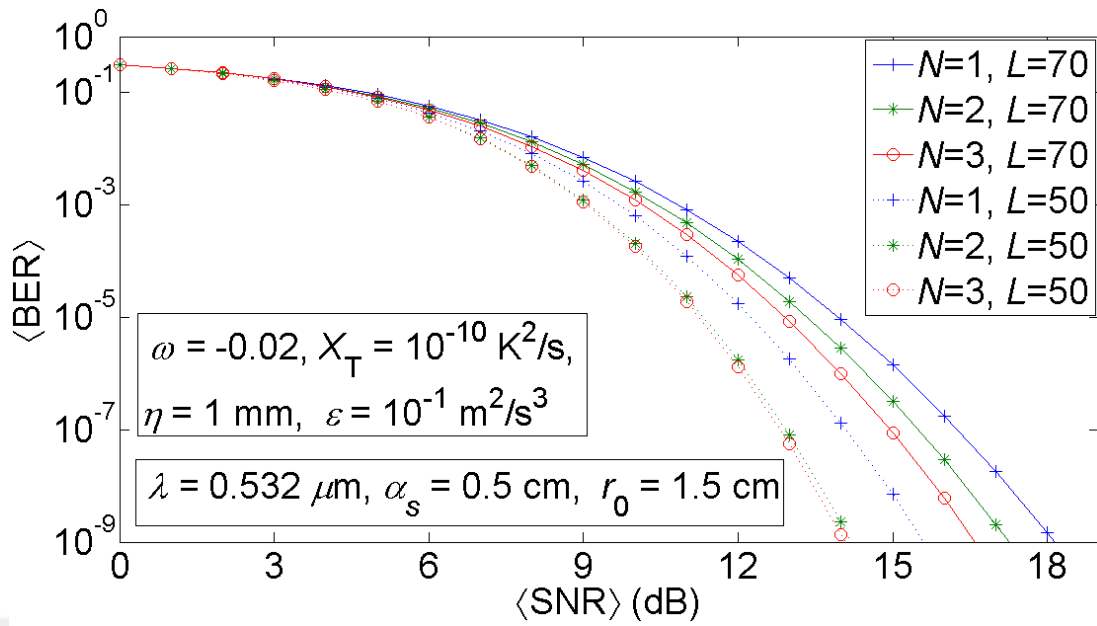
Figure 41 <BER> versus <SNR> for different *N* and *L* values.

In this section, we have shown the advantages of the MISO link which is used as a turbulence mitigation technique for oceanic turbulence. The results given in this section is helpful for the design of UWOC systems.

CHAPTER 5

CONCLUSION

In this thesis, the effect of spatial diversity on the performance of FSO system is investigated by considering multiple transmitters with laser array beam and multiple detectors with radial array apertures in the presence of weak atmospheric turbulence. Turbulence mitigation techniques, namely the use of partially coherent source and the aperture averaging are also taken into account. In finding the performance indicators, the extended Huygens - Fresnel principle is used to formulate the received mean field, average optical intensity, intensity correlation, average power and power correlation at the receiver apertures. In this way, performance indicators, namely the power scintillation index, aperture averaging factor and <BER> are examined as a function of FSO system parameters. In the derivation of the received mean field, Kolmogorov power spectrum is used where the inner and outer scale of turbulence are taken as $\ell_0 = 0$ and $L_0 = \infty$, respectively. Due to weak turbulence condition in horizontal link, log-amplitude correlation function is taken as $B_x \ll 1$ and quadratic approximation is used in the wave structure function. In Chapter 3, we initially formulate the average received intensity and average power and then the average of the square of the power on the receiver aperture to evaluate the performance indicators. At first, by the help of the formulations the performance of multiple-input single-output FSO system is investigated for both coherent and partially coherent Gaussian sources. Then, we improve our formulations and investigate the performance of multiple-input multiple-output FSO system. To ensure the correctness of the formulations, we check the scintillation index values of point detector with the existing results in the literature to be sure of their validity.

In our performance evaluations, we have found in the MISO FSO system (see Section 3.1) is that as the number of transmitter beamlets N increases, the power scintillation decreases. However, when N is chosen larger than 3, there is no

variation in the power scintillation. This is due to fact that intensity variations of the received optical field which fall within the receiver aperture area do saturate by adding an additional beamlet in the transmit array, and thus change in the power scintillation is not observed. Further, an increase in the transmitter ring radius causes a decrease in the power scintillation. Similar to ring radius variations, an increase in the source size is also observed to reduce the power scintillation. We note here that source size is chosen physically small so as to fill the receiver aperture area with received optical beam (i.e., small source size means large beam divergence which results in larger footprint). Also, when the receiver aperture area is increased, the power scintillation begins to decrease. This further results in a decrease the aperture averaging factor. We also investigated the average bit error rate of the MISO FSO system resulting from the power scintillation (see Section 3.2). It was found that when the source size, the ring radius and the receiver aperture radius increase, <BER> decreases. The ring radius variation is pronounced for larger number of beamlets.

The performance of the MISO FSO system using partially coherent laser beam array and an aperture is demonstrated in Section 3.3. It is found that when the degree of source coherence is reduced, laser beam array turns into the partially coherent source array which remarkably provides a reduction in the power scintillation. An increase in the structure constant causes an increase in the power scintillation. Despite this fact, effective aperture averaging takes place, and consequently, the aperture averaging factor begins to decrease. The effect of partially coherent source array on the system performance is compared with the laser beam array. It is concluded that in reducing the power scintillation, partially coherent source array is advantageous as compared to coherent beam array.

In Section 3.4, the effects of multiple input multiple output system on the performance of the FSO communication link have been scrutinized by employing a partially coherent laser beam array and a detector array. It is found that when the number of receiver detectors H increase, the power scintillation decreases asymptotically into the saturation level. This saturation especially occurs when H is chosen larger than 3. Further, an increase in the receiver ring radius causes a

decrease in the power scintillation. This phenomenon can be explained by the fact that receiver detectors see statistically different channels by increasing the receiver ring radius which in turn results in a reduction in the signal fading. This way, uncorrelated optical noise at the receiver detectors is mitigated by summing the optical powers of all the detector apertures and this causes a decrease in the power scintillation. We also investigated the performance of MIMO FSO system in terms of <BER>. It is observed that <BER> decreases as the receiver ring radius, the receiver aperture radius and the number of receiver apertures increase. The performance of MIMO FSO system is also compared to that of MISO and the SIMO FSO system. It is concluded that MIMO system shows better performance than those in SISO, MISO, and SIMO systems.

In Chapter 4, the transmit diversity technique used in the FSO communication system is repeated in UWOC system. This way, the effect of oceanic turbulence parameters, as well as system parameters are investigated on the performance of the MISO UWOC system. At first, the average intensity and the average of the square of the intensity of coherent laser beam array are derived at the receiver axis. Then, the performance evaluation based on the scintillation index and the bit error rate has been demonstrated. The evaluation of the scintillation index is dependent on the evaluation of the equivalent structure constant of atmosphere which expresses the atmospheric turbulence structure constant in terms of the oceanic turbulence parameters. Examining the oceanic and MISO UWOC system parameters on the system performance, it is observed that when the rate of dissipation of the turbulent kinetic energy per unit mass of fluid increases, the scintillation index asymptotically decreases. Similarly, an increase in the laser wavelength provides a reduction in the scintillation. Furthermore, an increase in the transmitter ring radius and the number of transmitter beamlets reduce the scintillation index. On the other hand, an increase in the link distance, the rate of dissipation of the mean squared temperature, Kolmogorov microscale and the ratio of temperature to salinity contributions to the refractive index spectrum (which means that the oceanic turbulence strength is increased) cause an increase in the scintillation index. It should be noted that the ability of the number of beamlets to reduce the scintillation is pronounced when the strength of oceanic turbulence is increased. We also investigated the performance of

the MISO UWOC system in terms of the average bit error rate and we found that <BER> decreases as the <SNR> and the number of beamlets increase. From the numerical results presented in Chapter 4, it is concluded that MISO UWOC systems show better scintillation and <BER> performance than SISO UWOC systems.

REFERENCES

1. **Khalighi M. A., Uysal M., (2014),** "*Survey on free space optical communication: a communication theory perspective*", IEEE Commun. Surv. Tutorials, vol. 16, pp. 2231-2258.

2. **Chan, V. W. S., (2006),** "*Free-space optical communications*", J. Lightwave Technol., vol. 24, pp. 4750-4762.

3. **Das, S., Henniger H., Epple B., Moore, C. I., Rabinovich W., Soba, R., Young, D., (2009),** "*Requirements and challenges for tactical free-space lasercomm*", in Proceedings of IEEE, MILCOM 2008, pp. 1-10.

4. **Bouchet O.**, **Sizun H., Boisrobert C., Fornel F., Favennec P. N., (2006),** "*Free-Space Optics: Propagation and Communication*", ISTE, London.

5. **Majumdar A. K. and Ricklin J. C., (2008),** "Free-Space Laser Communications Principles and Advances", Springer, New York.

6. **Willebrand H. A. and Ghuman B. S., (2001),** "*Fiber optics without fiber*", IEEE Spectrum, vol. 38, no. 8, pp. 40-45.

7. **Willebrand H. and Ghuman B., (2001),** "*Free Space Optics: Enabling Optical Connectivity in Today's Networks*", Sams, Indianapolis USA.

8. **Ciaramella E.**, **Arimoto Y., Contestabile G., Presi M., D'Errico A., Guarino V., Matsumoto M., (2009),** "*1.28-Tb/s (32×40 Gb/s) free-space optical WDM transmission system*", IEEE Photon.. Technol. Lett., vol. 21, no. 16, pp. 1121-1123.

9. **Su K., Moeller L., Barat R. B., Federici J. F., and Arnon S., (2004),** "*Experimental comparison of performance degradation from terahertz and infrared wireless links in fog,*", J. Opt. Soc. Am. A, vol. 29, no. 2, pp. 179-184.

10. **Kedar D. and Arnon S., (2004),** "*Urban optical wireless communication networks: The main challenges and possible solutions*", IEEE Commun. Mag., vol. 42, no. 5, pp. 2-7.

11. **Bloom S., Korevaar E., Schuster J., Willebrand H., (2003),** "*Understanding the performance of free-space optics*", J. Opt. Netw., vol. 2, no. 6, pp. 178-200.

12. **Juarez J. C, Dwivedi A., Hammons A. R., Jones S. D., Weerackody V., Nichhols R. A, (2006),** "*Free-space optical communications for next-generation military networks*", IEEE Commun. Mag., vol. 44, no. 11, pp. 46-51.

13. **Hemmati H., Biswas A., Djordjevic I. B., (2011),** "*Deep space optical communications: Future perspectives and applications*", Proceedings of the IEEE, vol. 99, no. 11, pp. 2020-2039.

14. **Sodnik Z., Lutz H., Furch B., Meyer R., (2010),** "*Optical satellite communications in Europe*", Proc. SPIE, vol. 7587, pp. 758705.

15. **Sova R. M., Lutz H., Furch B., Meyer R., (2010),** "*80 Gb/s free-space optical communication demonstration between an aerostat and a ground terminal*", Proc. SPIE, vol. 6304, pp. 630414.

16. **Yamakawa S., Hanada T., Kohata H., Fujiwara Y., (2010),** "*JAXA's efforts toward next generation space data-relay satellite using optical inter-orbit communication technology*", Proc. SPIE, vol. 7587, pp. 75870P.

17. **Liao R., (2011),** Ph.D. Thesis, Dept. of Elec. Comp. Eng., Michigan Technological Uni., USA.

18. **Farid A. A, Hranilovic S., (2007),** "*Outage capacity optimization for free-space optical links with pointing errors*", J. Lightw. Technol, vol. 25, no. 7, pp. 1702-1710.

19. **Fried D. L., (1973),** "*Statistics of laser beam fade induced by pointing jitter*", Appl. Opt., vol. 12, no. 2, pp. 422-423.

20. **Kim I. I., Stieger R., Koontz J. A., Moursun C., Barclay M., Adhikari P., Schuster J., Korevaar E., Ruigrok R., DeCusatis C., (1998),** "*Wireless optical transmission of fast Ethernet, FDDI, ATM, and ESCON protocol data using the TerraLink laser communication system* ", Opt. Eng., vol. 37, no. 12, pp. 3143-3155.

21. **Arnon S., (2003),** "*Effects of atmospheric turbulence and building sway on optical wireless communication systems*", Opt. Lett., vol. 28, no. 2, pp. 129-131.

22. **Borah D. K., Voelz D. G., (2009),** "*Pointing error effects on free-space optical communication links in the presence of atmospheric turbulence*", J. Lightw. Technol, vol. 27, no. 18, pp. 3965-3973.

23. **Abushagur A. A. G., Abbou F. M., Abdullah M., Misran N., (2011),** "*Performance analysis of a free-space terrestrial optical system in the presence of absorption, scattering, and pointing error* ", Opt. Eng., vol. 50, no. 7, pp. 075007.

24. **Çil C. Z., Baykal Y., Eyyuboğlu, H. T., Cai, Y., (2009),** "*Beam wander characteristics of cos and cosh-Gaussian beams*", Appl. Phys. B, vol. 95, no. 4, pp. 763-771.

25. **Dios F., Rubio J. A., Rodriduez A., Cameron A., (2014),** "*Scintillation and beam-wander analysis in an optical ground station-satellite uplink*", Appl. Opt. vol. 43, no. 19, pp. 3866-3872.

26. **Andrews L. C. and Philips R. L., (2005),** "*Laser Beam Propagation through Random Media*", SPIE, Washington.

27. **Andrews L. C.**, **Philips R. L., Hopen C. Y., (2001),** "*Laser Beam Scintillation with Applications*", SPIE, Washington.

28. **Sandalidis H. G., Tsiftsis T. A., Karagiannidis G. K., Uysal M., (2008),** "*BER performance of FSO links over strong atmospheric turbulence channels with pointing errors*", IEEE Commun. Lett., vol. 12, no. 1, pp. 44-46.

29. **Ren Y., Dang A., Luo B., Guo H., (2010),** "*Capacities for long-distance free-space optical links under beam wander effects*", IEEE Photon. Technol. Lett., vol. 22, no. 14, pp. 1069-1071.

30. **Sandalidis H. G., (2008),** "*Optimization models for misalignment fading mitigation in optical wireless links*", IEEE Commun. Lett., vol. 12, no. 5, pp. 395-397.

31. **Ghassemlooy Z, Popoola W., Rajbhandari S., (2013),** "*Optical Wireless Communications: System and Channel Modelling with Matlab*", CRC Press, Boca Raton, Florida.

32. **Jaksic Zoran (2014),** "*Micro and Nanophotonics for Semiconductor Infrared Detectors: Towards an Ultimate Uncoded Device*", Springer.

33. **McCartney E. J., (1976),** "*Optics of the Atmosphere*", Wiley, Hoboken.

34. **O'Brien D. C., Quasem S., Zikic S., Faulkner G. E., (2006),** "*Multiple input multiple output systems for optical wireless: Challenges and possibilities*", Proc. SPIE, vol. 6304, pp. 630416.

35. **Bates D. R., (1984),** "*Rayleigh scattering by air*", Planet. Space Sci., vol. 32, no. 6, pp. 785-790.

36. **Kim I. I.**, **McArthur B., Korevaar E., (2001),** "*Comparison of laser beam propagation at 785 nm and 1550 nm in fog and haze for optical wireless communications*", Proc. SPIE, vol. 4214, pp. 26-37.

37. **Hemmati H., (2006),** "*Deep Space Optical Communications: Deep Space Communications and Navigation Series*", Wiley-Interscience, California.

38. **Muhammad S. S., Flecker B., Leitgeb E., Gebhart M., (2007),** "*Characterization of fog attenuation in terrestrial free space optical links*", Opt. Eng., vol 46, no.6, pp. 066001.

39. **Malik A., Singh P., (2015),** "*Free space optics: Current applications and future challenges*", Int. J. Opt., vol. 2015, no. 945483, pp.1-7.

40. **Kolmogorov A. N, (1941),** "*The local structure of turbulence in incompressible viscous fluid for very large Reynolds numbers*", Doklady Akademiia Nauk SSSR, vol. 30, no. 4, pp. 301-305.

41. **Hill R. J., (1978),** "*Models of the scalar spectrum for turbulent advection*", J. Fluid Mech. vol. 88, pp. 541-662.

42. **Ishimaru A., (1978),** "*Wave Propagation and Scattering in Random Media: vol. 2*", Academic Press, New York.

43. **Richardson L. F., (1922),** "*Weather Prediction by Numerical Process*", Cambridge University Press, Cambridge.

44. **Barat J., (1982),** "*Some characteristics of clear-air turbulence in the middle stratosphere*", J. Atmos. Sci. vol. 39, pp. 2553-2564.

45. **Hocking W. K., (1985),** "*Measurements of turbulent energy dissipation rates in the middle atmosphere by radar techniques: A review*", Radio. Sci. vol. 20, no. 6, pp. 1403-1422.

46. **Wang F., Liu X., Cai Y., (2015)** "*Propagation of partially coherent beam in turbulent atmosphere: A review*", Prog. Electromagn. Res., vol. 150, pp. 123-143.

47. **Voelz D., Xiao X., (2009),** "*A brief review of spatially partially coherent beams for FSO communications*", Proc. SPIE, vol. 7200, pp. 72000C.

48. **Gbur G., (2014),** "*Partially coherent beam propagation in atmospheric turbulence [invited]*", J. Opt. Soc. Am. A., vol. 31, no. 9, pp. 2038-2045.

49. **Wang F., Liu X., Yuan Y., Cai Y., (2013)** "*Experimental generation of partially coherent beams with different complex degrees of coherence*", J. Opt. Lett., vol. 38, no. 11, pp. 1814-1816.

50. **Wang S. C H., Plonus M. A., (1979)** "*Optical beam propagation for a partially coherent source in the turbulent atmosphere*", J. Opt. Soc. Am, vol. 69, no. 9, pp. 1297-1304.

51. **Ricklin J. C., Davidson F. M., (2002),** "*Atmospheric turbulence effects on a partially coherent Gaussian beam: implications for free-space laser communication*", J. Opt. Soc. Am., vol. 19, no. 9, pp. 1794-1802.

52. **Fante R. L.**, **(1981),** "*Intensity fluctuations of an optical wave in a turbulent medium Effect of source coherence*", Opt. Acta., vol. 28, pp. 1203-1207.

53. **Baykal Y., Plonus M. A., Wang S. J., (1983),** "*The scintillations for weak atmospheric turbulence using a partially coherent source*", Radio Sci., vol. 18, no. 4, pp. 551-556.

54. **Feizulin Z. I., Kravtsov Y. A., (1967),** "*Broadening of a laser beam in a turbulent medium*", Quantum Electron., vol. 10, no. 1, pp. 33-35.

55. **Efimov A., Velizhanin K., Gelikonov G., (2014),** "*Simultaneous scintillation measurements of coherent and partially coherent beams in an open atmosphere experiment*", Proc. SPIE, vol. 8971, pp. 897105.

56. **Polynkin P., Peleg A., Rhoadarmer T., Moloney J.**, **(2007),** "*Optimized multiemitter beams for free-space optical communications through turbulent atmosphere*", Opt. Lett, vol. 32, pp. 885-887.

57. **Mikesell, A. H., Hoag A. A. Hall J. S., (1951),** "*The scintillation of starlight*", J. Opt. Soc. Am., vol. 41, no. 10, pp. 689-695.

58. **Fried D. F., (1967)** "*Aperture averaging of scintillation*", J. Opt. Soc. Am., vol. 57, no. 2, pp. 169-175.

59. **Tatarskii V. I., (1971)** "*The effects of the turbulent atmosphere on wave propagation*", National Technical Information Service, Springfield.

60. **Andrews L. C., (1992)** "*Aperture-averaging factor for optical scintillation of plane and spherical waves in the atmosphere*", J. Opt. Soc. Am A, vol. 9, no. 4, pp. 597-600.

61. **Wang. S. J., Baykal Y., Plonus M. A., (1983),** "*Receiver-aperture averaging effects for the intensity fluctuation of a beam wave in the turbulent atmosphere*", J. Opt. Soc. Am. A, vol. 73, pp. 831-837.

62. **Kamacıoğlu C., Baykal Y., Yazgan E., (2013),** "*Averaging* of receiver aperture for flat-topped incidence", Opt. Laser Technol, vol. 52, pp. 91-95.

63. **Kamacıoğlu C., Baykal Y., Yazgan E., (2013),** "*Aperture averaging of focused multi-Gaussian beams*", in Proceedings of PIERS, Stockholm, Sweeden, pp. 1623-1626.

64. **Kamacıoğlu C., Baykal Y., Yazgan E., (2013),** "*Receiver-aperture averaging of annular beams propagating through turbulent atmosphere*", Opt. Eng., vol. 52, pp. 126103.

65. **Andrews L. C., Philips R. L., Hopen C. Y., (2000),** "*Aperture averaging of optical scintillations: power fluctuations and the temporal spectrum*", Wave Random Media, vol. 10, no. 1, pp.53-70.

66. **Zhang Y., Zhu T., Tao C., (2004),** "*Aperture-averaging effects for weak to strong scintillations in turbulent atmosphere*", Chin. Opt. Lett., vol. 2, no.7, pp. 373-375.

67. **Barrios R., Dios F**, **(2012),** "*Exponentiated Weibull distribution family under aperture averaging for Gaussian beam waves*", Opt. Express, vol. 20, pp. 13055-13064.

68. **Khalighi M. A., Aitamer N., Schwartz N., Bourennane S., (2009),** "*Turbulence mitigation by aperture averaging in wireless optical systems*", in Proceedings of IEEE, Telecommunications (ConTEL), accession number 10859534, pp. 59-66.

69. **Lee I. E., Ghassemlooy Z., Ng W. P., Khalighi M. A., Liaw S. K., (2016),** "*Effects of aperture averaging and beam width on a partially coherent Gaussian beam over free-space optical links with turbulence and pointing errors*", Appl. Opt., vol. 55, no.1, pp. 1-9.

70. **Safari M., Uysal M., (2008),** "*Diversity gain analysis of free-space optical communication systems*", in Proceedings of IEEE, Electrical and Computer Engineering, Niagara Falls, Canada, pp. 001239-001244.

71. **Navidpour S. M., Uysal M., Kavehrad M., (2007),** "*BER performance of free-space optical transmission with spatial diversity*", IEEE Trans, Wireless Commun. vol. 6, pp. 2813-2819.

72. **Lee E. J., Chan V. W. (2004),** "*Part 1: Optical communications over the clear turbulent atmospheric channel using diversity*", IEEE J. Sel. Areas Commun., vol. 22, pp. 1896-1906.

73. **Navidpour S., Uysal M., Jing L.**, **(2004),** "*BER performance of MIMO free-space optical links*", in Proceedings of IEEE, 60th Vehicular Technology, vol. 5, pp. 3378-3382.

74. **Shin E. J., Chan V. W. S., (2002),** "*Optical communication over the turbulent atmospheric channel using spatial diversity*", in Proceedings of IEEE, Global Telecommunications Conference (GLOBECOM), vol. 3, pp. 2055-2060.

75. **Haas S. M., Shapiro J. H., (2003),** "*Capacity of wireless optical communications*", IEEE J. Sel. Area Commun., vol. 21, pp. 1346-1357.

76. **Khalighi M. A., Schwartz N., Aitamer N., Bourennane S., (2009),** "*Fading reduction by aperture averaging and spatial diversity in optical wireless systems* ", IEEE/OSA J. Opt. Commun. Netw., vol. 1, pp. 580-593.

77. **Krishnan P., Kumar D. S., (2014),** "*Bit error rate analysis of free-space optical system with spatial diversity over strong atmospheric turbulence channel with pointing errors*", Opt. Eng., vol. 53, pp. 126108.

78. **Kaur P., Jain V. K., Kar S., (2015),** "*Performance analysis of free space optical links using multi-input multi-output and aperture averaging in presence of turbulence and various weather conditions*", IET Commun., vol. 9, pp. 1104-1109.

79. **Letzepis N., Fabregas A. G. I., (2009),** "*Outage probability of the Gaussian MIMO free-space optical channel with PPM*", IEEE Trans. Commun., vol. 57, pp. 3682-3690.

80. **Farid A. A., Hranilovic S., (2011),** "*Outage capacity for MISO intensity-modulated free-space optical links with misalignment*", IEEE/OSA J. Opt. Commun. Netw., vol. 3, pp. 780-789.

81. **Tsiftsis T. A., Sandalidis H. G., Karagiannidis G. K., Uysal M., (2009),** "*Optical wireless links with spatial diversity over strong atmospheric turbulence channels*", IEEE Trans. Wireless Commun., vol. 8, pp. 951-957.

82. **Safari M., Hranilovic S., (2012),** "*Diversity gain for near-field MISO atmospheric optical communications*", in Proceedings of IEEE, International Conference on Communications (ICC), Ottawa, Canada, pp. 3128-3132.

83. **Higg C., Barday H., Cusumano S., Biliman K., (1998),** "*Active tracking using multibeam illumination*", Proc. SPIE, vol. 3381, pp. 160-167.

84. **Cai Y., Chen Y., Eyyuboğlu H. T., Baykal Y., (2007),** "*Propagation of laser array beams in a turbulent atmosphere* ", Appl. Phys. B, vol. 88, pp. 467-475.

85. **Yuan Y., Cai Y., Zhao C., Eyyuboğlu H. T., Baykal Y., (2010),** "*Propagation factors of laser array beams in turbulent atmosphere*", J. Mod. Opt., vol. 57, no.8, pp. 621-631.

86. **Baykal Y., (2014),** "*Field correlation of laser arrays in atmospheric turbulence*", Appl. Opt., vol. 53, pp. 1284-1289.

87. **Baykal Y., Uysal M., (2014),** "*Analysis of field correlations in atmospheric optical MIMO systems*", in Proceedings of IEEE, 3th International Workshop on Optical Wireless Communications (IWOW), Madeira Island, Portugal, pp. 30-34.

88. **Baykal Y., Eyyuboğlu H. T., Cai Y., (2009),** "*Scintillation of partially coherent multiple Gaussian beams in turbulence*", Appl. Opt, vol.48, pp. 1943-1954.

89. **Baykal Y., Eyyuboğlu H. T., Cai, Y., (2010),** "*Partially coherent off-axis Gaussian beam scintillations*", J. Mod. Opt., vol. 57, pp.1221-1227.

90. **Arpali Ç., Arpali S. A., Baykal Y., Eyyuboğlu H. T. (2011),** "*Intensity fluctuations of partially coherent laser beam arrays in weak atmospheric turbulence*", Appl. Phys. B., vol.103, pp. 237-244.

91. **Baykal Y., (2006),** "*Intensity fluctuations for source arrays in turbulent atmosphere*", Proc. SPIE, vol. 6303, pp. 630308-1-12.

92. **Öztan M. A., Baykal Y., (2015),** "*Scintillations of partially coherent annular and flat-topped array beams in extremely strong turbulent medium*", Opt. Commun., vol. 354, pp. 419-427.

93. **Gerçekcioğlu H., Baykal Y., (2015),** "*Intensity fluctuations of laser array beams in non-Kolmogorov turbulence*", IEEE J. Sel. Area Comm., vol. 33, no. 9, pp. 1877-1882.

94. **Eyyuboğlu H. T., Baykal Y., Cai Y., (2008),** "*Scintillation of laser array beams*", Appl. Phys. B., vol. 91, pp. 265-271.

95. **Kim I. I., Hakakha H., Adhikari P., Korevaar E. J., Majumdar A. K., (1997),** "*Scintillation reduction using multiple transmitters*", Proc. SPIE, vol. 2990, pp. 102-113.

96. **Kim I. I., Mitchell M., Korevaar E., (1999),** "*Measurement of scintillation for free-space laser communication at 785 nm and 1550 nm*", Proc. SPIE, vol. 3850, pp. 49-62.

97. **Tang H., Yuan X., Wang B. (2013),** "*Scintillation optimization of linear Gaussian beam array propagating through weak turbulence*", J. Mod. Opt., vol. 60, no. 20, pp.1830-1837.

98. **Gökçe M. C., Baykal Y., Uysal M., (2014),** "*Effect of LED sources on the performance of MIMO FSO systems*", in Proceedings of Çankaya University Symposium, Mühendislik ve Teknoloji Sempozyumu (MTS 7), Ankara, Turkey, pp. 133-135.

99. **Anguita J. A., Neifeld M. A., Vasic B. V., (2007),** "*Spatial correlation and irradiance statistics in a multiple-beam terrestrial free-space optical communication link*", Appl. Opt., vol. 46, pp. 6561-6571.

100. **Chen Z., Yu S., Wang T., Wu G., Guo H., Gu W. (2013),** "*Spatial correlation for transmitters in spatial MIMO optical wireless links with Gaussian-beam waves and aperture effects*", Opt. Commun., vol. 287, pp. 12-18.

101. **Gökçe M. C., Kamacıoğlu C., Uysal M., Baykal Y., (2014),** "*Performance analysis of MIMO FSO systems with radial array beams and finite sized detectors*", Proc. SPIE, vol. 9224, pp. 922409.

102. **Gökçe M. C., Baykal Y., Kamacıoğlu C., Uysal M., (2015),** "*Aperture averaging in multiple–input single-output free-space optical systems*", Opt. Eng., vol 54,no. 6, pp. 066103.

103. **Gökçe M. C., Baykal Y., Uysal M., (2016),** "*Bit error rate analysis of MISO FSO systems*", Wave Random Complex., vol. 26, no. 4, pp. 642-649.

104. **Gökçe M. C., Baykal Y., Uysal M., (2015),** "*Effect of partial coherence on MISO FSO systems*", in Proceedings of IEEE, 4th International Workshop on Optical Wireless Communications (IWOW), İstanbul, Turkey, pp. 88-92.

105. **Gökçe M. C., Baykal Y., Uysal M., (2016),** "*Aperture averaging in multiple–input single-output free-space optical systems using partially coherent radial array beams*", J. Opt. Soc. Am. A., vol 33, pp. 1041-1048.

106. **Gökçe M. C., Baykal Y., Uysal M., (2016),** "*Performance analysis of multiple-input multiple-output freespace optical systems with partially coherent Gaussian beams and finite-sized detectors*", Opt. Eng., vol. 55 no. 11, pp. 111607.

107. **Thorpe S. A., (2007),** "*An Introduction to Ocean Turbulence*", Cambridge University Press, Cambridge.

108. **Thorpe S. A., (2005),** "*The Turbulent Ocean*", Cambridge University Press, Cambridge.

109. **Cossu G., Corsini R., Khalid A. M., Balestrino S., Coppelli A, Caiti A., Ciaramella E., (2013),** "*Experimental demonstration of high speed underwater visible light communications*", in Proceedings of IEEE, 2th International Workshop on Optical Wireless Communications (IWOW), Newcastle, United Kingdom, pp. 11-15.

110. **Arnon S., Barry J. R., Karagiannidis G. K., Schober R., Uysal M., (2012),** "*Advanced Optical Wireless Communication*", Cambridge University Press, Cambridge.

111. **Doniec M., Vasilescu I., Chitre M., Detweiler C., Hoffmann-Kuhnt M., Rus D., (2009),** "*AquaOptical: A lightweight device for high-rate long-range underwater point-to-point communication*", in Proceedings of IEEE, Oceans, pp. 1-6.

112. **Hanson F., Radic S., (2008),** "*High bandwidth underwater optical communication*", App. Opt., vol. 47, no. 2, pp. 277-283.

113. **Liu L., Zhou S., Cui J. H., (2008),** "*Prospects and problems of wireless communication for underwater sensor networks*", Wireless Commun. Mobile Comput., vol. 8, no. 8, pp. 977-994.

114. **Caiti A., Calabrò V., Munafò A., Dini G., Lo Duca A., (2013),** "*Mobile Underwater Sensor Networks for Protection and Security: Field Experience at the UAN11 Experiment*", J. Field Robot., vol. 30, no. 2, pp. 237-253.

115. **Johnson L. J., Jasman F., Green R., Leeson M. S., (2014),** "*Recent advances in underwater optical wireless communications*", Underwater Technology, vol. 32, no. 3, pp. 167-175.

116. **Khalighi M. A., Gabriel C., Hamza T., Bourennane S., Leon P., Rigaud V., (2014),** "*Underwater wireless optical communication; recent advances and remaining challenges*", in Proceedings of Transparent Optical Networks, ICTON, pp. 1-4.

117. **Ghassemlooy Z., Arnon S., Uysal M., Xu Z., Cheng J., (2015),** "*Emerging optical wireless communications-advances and challenges*", IEEE J. Sel. Area Commun., vol. 33, no. 9, pp. 1738-1749.

118. **Kaushal H., Kaddoum G., (2016),** "*Underwater Optical Wireless Communication*", IEEE Access vol. 4, pp. 1518-1547.

119. **Kettle H., Merchant C. J., (2008),** "*Modeling ocean primary production: sensitivity to spectral resolution of attenuation and absorption of light*", Prog. Oceanogr., vol. 78, no. 2, pp. 135-146.

120. **Johnson L. J., Green R. J., Leeson M. S., (2013),** "*Underwater optical wireless communications: depth dependent variations in attenuation* ", Appl. Opt., vol. 52, no. 33, pp. 7867-7873.

121. **Matciak M., (2012),** "*Anomalous diffraction approximation to the light scattering coefficient spectra of marine particles with power law size distribution*", Opt. Express., vol. 20, no. 25, pp. 27603-27611.

122. **Stramski D., Boss E., Bogucki D., Voss K. J., (1963),** "*The role of seawater constituents in light backscattering in the ocean*", Prog. Oceanogr., vol. 61, no. 1, pp. 27-56.

123. **Potbriant C., Farr N., Ware J., Preisig J., Popenoe H., (2008),** "*Diffuse high-bandwidth optical communications*", in Proceedings of IEEE, Oceans, pp. 1-4.

124. **Duntley S. Q., (1963),** "*Light in the sea*", J. Opt. Soc. Am., vol. 53 no. 2, pp. 214-233.

125. **Gilbert G. D., Stoner T. R., Jergian J. L., (1966),** "*Underwater experiments on the polarization, coherence, and scattering properties of a pulsed blue-green laser*", Proc. SPIE Underwater Photo Optics I, vol. 0007.

126. **Yi X., Li Z., Liu Z., (2015),** "*Underwater optical communication performance for laser beam propagation through weak oceanic turbulence*", Appl. Opt., vol. 54, no. 6, pp. 1273-1278.

127. **Yousefi M., Golmohammady S., Mashal A., Kashani F. D., (2015),** "*Analyzing the propagation behavior of scintillation index and bit error rate of a partially coherent flat-topped laser beam in oceanic turbulence*", J. Opt. Soc., vol. 32, no. 11, pp. 1982-1992.

128. **Baykal Y., (2015),** "*Intensity fluctuations of multimode laser beams in underwater medium*", J. Opt. Soc. A, vol. 32, no. 4, pp. 593-598.

129. **Baykal Y., (2015),** "*Higher order mode laser beam scintillations in oceanic medium*", Wave Random and Complex., vol. 26, no. 1, pp. 21-29.

130. **Gerçekcioğlu H., (2014),** "*Bit error rate of focused Gaussian beams in weak oceanic turubulence*", J. Opt. Soc. Am. A, vol. 31, no. 9, pp. 1963-1968.

131. **Ata Y., Baykal Y., (2014),** "*Scintillations of optical plane and spherical waves in underwater turbulence*", J. Opt. Soc. Am. A, vol. 31, no. 7, pp. 1552-1556.

132. **Korotkova O., Farwell N., Shchepakina E., (2012),** "*Light scintillation in oceanic turbulence*", Wave Random Complex, vol. 22, no. 2, pp. 260-266.

133. **Baykal Y., (2016),** "*Fourth-order mutual coherence function in oceanic turbulence*", Appl. Opt., vol. 55, no. 11, pp. 2976-2979.

134. **Jamali M. V., Akhoundi F., Salehi J. A., (2015),** "*Performance studies of underwater wireless optical communication systems with spatial diversity: MIMO scheme*", arXiv preprint arXiv:1508.03952, 2015.

135. **Jamali M. V., Akhoundi F., Salehi J. A., (2015),** "*On the BER of multiple-input multiple-output underwater wireless optical communication systems*", in Proceedings of IEEE, 4th International Workshop on Optical Wireless Communications (IWOW), İstanbul, Turkey, pp. 26-30.

136. **Dong Y., Liu Jinxing, (2016),** "*On BER performance of underwater wireless optical MISO links under weak turbulence*", in Proceedings of IEEE, Oceans, Shanghai, China, pp. 1-4.

137. **Liu W., Xu Z., Yang L., (2015),** "*SIMO detection schemes for underwater optical wireless communication under turbulence*", Photon. Res., vol. 3, no. 3, pp. 48-53.

138. **Zhang H., Dong Y., Hui L., (2015),** "*On capacity of downlink underwater wireless optical optical MIMO systems with random sea surface*", IEEE Commun. Lett., vol. 19, no. 12, pp. 2166-2169.

139. **Nikishov V. V., Nikishov V. I., (2000),** "*Spectrum of turbulent fluctuations of the sea-water refraction index*", Int. J. Fluid Mech. Res., vol. 27, no.1, pp. 82-98.

140. **Lu L., Wang Z., Zhang J., Zhang P., Qiao C., Fan C., Ji X., (2015),** "*Average intensity of $M \times N$ Gaussian array beams in oceanic turbulence*", App. Opt., vol. 54, no. 25, pp. 7500-7507.

141. **Zhi D., Chen Y. Z., Tao R. M, Ma Y. X., Zhou P., Si L.,(2015),** "*Average spreading and beam quality evolution of Gaussian array beams propagating through oceanic turbulence*", Laser Phys Lett, vol. 12, no. 11, pp. 116001.

142. **Tang M., Zhao D., (2015),** "*Regions of spreading of Gaussian array beams propagating through oceanic turbulence*", Appl. Opt., vol 54, no. 11, pp. 3407-6136.

143. **Lu L., Zhang P., Fan C., Qiao C., (2015),** "*Influence of oceanic turbulence on propagation of a radial Gaussian beam array on propagation of a radial Gaussian beam array*", Opt. Express, vol. 23, no. 3, pp. 2827-2836.

144. **Kashani F. D., Yousefi M., (2016),** "*Analyzing the propagation behavior of coherence and polarization degrees of a phase-locked partially coherent radial flat-topped array laser beam in underwater turbulence*", Appl. Opt., vol 55, no. 23, pp. 6311-6320.

145. **Baykal Y., (2016),** "*Expressing oceanic turbulence parameters by atmospheric turbulence structure constant*", Appl. Opt., vol. 55 no. 6, pp. 1228-1231.

146. **Gökçe M. C., Baykal Y., (2016),** "*Scintillation analysis of multiple-input single-output underwater optical links*", Appl. Opt., vol 55, no. 22, pp. 6130-6136.

147. **Simpson J. A., Hughes B. L., Muth J. F., (2009),** "*A spatial diversity system to measure optical fading in an underwater communications channel*", in Proceedings of IEEE, Oceans, pp. 1-6.

148. **Kanaev A. V., Gladysz S., Almeida de R., Matt S., Nootz G. A., Josset D. B., Hou W., (2016),** "*Measurements of optical underwater turbulence under controlled conditions*", Proc. SPIE, vol. 9827, pp. 982705-1-8.

149. **Simpson J. A., Hughes B. L., Muth J. F., (2012),** "*Smart transmitters and receivers for underwater free-space optical communication*", IEEE J. Sel. Areas Commun., vol. 30, no. 5, pp. 964-974.

150. **Farr N., Chave A., Freitag L., Preisig J., White S., Yoerger D., Titterton P., (2005),** "*Optical modem technology for seafloor observatories*", in Proceedings of IEEE, Oceans, pp. 928-934.

151. **Farr N., Chave A. D., Freitag L., Preisig J., White S. N., Yoerger D., Sonnichsen F., (2006),** "*Optical modem technology for seafloor observatories*", in Proceedings of IEEE, Oceans, pp. 1-6.

152. **Gradshteyn I. S. and Ryzhik I. M., (2000),** "*Tables of Integrals, Series and Products*", Academic, USA.

153. **Leader J. C., (1978),** "*Atmospheric propagation of partially coherent radiation*", J. Opt. Soc. Am., vol. 68, pp. 175-185.

154. **Baykal Y. K., (2016),** "*Optical Wireless Communication An Emerging Technology*", Ch2 in Optical Propagation in Unguided Media, Springer, Switzerland.

APPENDICES

APPENDIX A

Derivation of the Average of the Square of the Power for Coherent MISO

Appendix A is taken from our paper [102].

Here the calculation of $\langle P^2 \rangle$ is shown. First, we need to calculate $\langle I(\mathbf{p_1}) I(\mathbf{p_2}) \rangle$ given by

$$
\begin{aligned}
\langle I(\mathbf{p_1}) I(\mathbf{p_2}) \rangle = \frac{1}{(\lambda L)^4} \int_{-\infty}^{\infty}\int_{-\infty}^{\infty} d^2\mathbf{s}_1 \int_{-\infty}^{\infty}\int_{-\infty}^{\infty} d^2\mathbf{s}_2 \int_{-\infty}^{\infty}\int_{-\infty}^{\infty} d^2\mathbf{s}_3 \int_{-\infty}^{\infty}\int_{-\infty}^{\infty} d^2\mathbf{s}_4 \\
\times u(\mathbf{s}_1) u^*(\mathbf{s}_2) u(\mathbf{s}_3) u^*(\mathbf{s}_4) \\
\times \exp\left[\frac{jk}{2L} \left(|\mathbf{p_1} - \mathbf{s}_1|^2 - |\mathbf{p_1} - \mathbf{s}_2|^2 + |\mathbf{p_2} - \mathbf{s}_3|^2 - |\mathbf{p_2} - \mathbf{s}_4|^2 \right) \right] \\
\times \left\langle \exp\left[\psi(\mathbf{s}_1, \mathbf{p_1}) + \psi^*(\mathbf{s}_2, \mathbf{p_1}) + \psi(\mathbf{s}_3, \mathbf{p_2}) + \psi^*(\mathbf{s}_4, \mathbf{p_2}) \right] \right\rangle,
\end{aligned}
\tag{A.1}
$$

where $\psi(\mathbf{s}, \mathbf{p})$ is the Rytov solution of the random part of the complex phase of a spherical wave propagating from the source point $(\mathbf{s}, z = 0)$ to the receiver point $(\mathbf{p}, z = L)$ with z being the propagation axis. The fourth order medium coherence function given in the last line of Eq. (A1) is used as the given in [61]. Employing Eq. (3.1) and the related equations of [61] in Eq. (A1) and using the resulting Eq. (A1) in Eq. (2.18), the equation for $\langle P^2 \rangle$ is obtained. Applying Eq. 3.323.2 of [152] which is

$\int_{-\infty}^{\infty} dx \exp\left(-t^2 x^2 \pm qx\right) = \left(\pi^{0.5}/t\right) \exp\left[q^2/(4t^2)\right]$, $\left[\operatorname{Re}(t^2) > 0\right]$ and performing the 8-fold integration over the source transverse coordinates and the 4-fold integration over the transverse receiver coordinates, we find

$$\langle P^2 \rangle = \frac{\exp\left(4\sigma_{\chi S}^2\right)}{\left(\lambda L\right)^4} \sum_{n=1}^{N}\sum_{m=1}^{N}\sum_{l=1}^{N}\sum_{o=1}^{N} \exp\left[-r_0^2 k\left(\alpha_n + \alpha_m + \alpha_l + \alpha_o\right)\right]$$

$$\times \exp\left(\frac{JJ_x^2}{4\beta_{1p}^2}\right)\exp\left(\frac{JJ_y^2}{4\beta_{1p}^2}\right)\exp\left(\frac{q_{2px}^2}{4\beta_{2p}^2}\right)\exp\left(\frac{q_{2py}^2}{4\beta_{2p}^2}\right)\exp\left(\frac{AA_x^2}{4\beta_3^2}\right)$$

$$\times \exp\left(\frac{AA_y^2}{4\beta_3^2}\right)\exp\left(\frac{CC_x^2}{4\beta_4^2}\right)\exp\left(\frac{CC_y^2}{4\beta_4^2}\right)\frac{\pi^6}{\beta_1^2\beta_2^2\beta_3^2\beta_4^2\beta_{1p}^2\beta_{2p}^2}$$

$$\times \exp\left(\frac{\cos^2\varphi_n k^2\alpha_n^2 r_0^2}{\beta_1^2} + \cos^2\varphi_n k^2\alpha_n^2 r_0^2 \frac{1}{\beta_2^2\beta_1^4\rho_0^4}\right) \qquad \text{(A.2)}$$

$$\times \exp\left(\frac{k^2\alpha_m^2 r_0^2\cos^2\varphi_m}{\beta_2^2} + \cos\varphi_n k\alpha_n r_0 \frac{2}{\beta_2^2\beta_1^2\rho_0^2} k\alpha_m r_0\cos\varphi_m\right)$$

$$\times \exp\left(\frac{\sin^2\varphi_n k^2\alpha_n^2 r_0^2}{\beta_1^2} + \sin^2\varphi_n k^2\alpha_n^2 r_0^2 \frac{1}{\beta_2^2\beta_1^4\rho_0^4}\right)$$

$$\times \exp\left(\frac{k^2\alpha_m^2 r_0^2\sin^2\varphi_m}{\beta_2^2} + \sin\varphi_n k\alpha_n r_0 \frac{2}{\beta_2^2\beta_1^2\rho_0^2} k\alpha_m r_0\sin\varphi_m\right),$$

where

$$\beta_1^2 = k\alpha_n - \frac{jk}{2L} + \frac{2}{\rho_0^2} - T, \ \beta_2^2 = -\frac{1}{\beta_1^2\rho_0^4} + \theta_1^2,$$

$$\beta_3^2 = -\frac{1}{\beta_2^2}\left(\frac{1}{\rho_0^2} - \frac{T}{\beta_1^2\rho_0^2}\right)^2 - \frac{T^2}{\beta_1^2} + \varsigma_1^2,$$

$$\beta_4^2 = -\frac{1}{\beta_3^2}\left[\frac{1}{\beta_2^2}\left(\frac{1}{\rho_0^2} - \frac{T}{\beta_1^2\rho_0^2}\right)\left(\frac{1}{\beta_1^2\rho_0^4} - R\right) - \frac{T}{\beta_1^2\rho_0^2} + \frac{1}{\rho_0^2}\right]^2$$

$$-\frac{1}{\beta_2^2}\left(\frac{1}{\beta_1^2\rho_0^4} - R\right)^2 - \frac{1}{\beta_1^2\rho_0^4} + \xi_1^2,$$

$$R = \frac{j}{\rho_{\chi S}^2} + \frac{1}{\rho_x^2}, \ T = -\frac{j}{\rho_{\chi S}^2} + \frac{1}{\rho_x^2},$$

$$\theta_1^2 = k\alpha_m + \frac{jk}{2L} + \frac{2}{\rho_0^2} - R, \ \varsigma_1^2 = k\alpha_l - \frac{jk}{2L} + \frac{2}{\rho_0^2} - T,$$

$$\xi_1^2 = k\alpha_o + \frac{jk}{2L} + \frac{2}{\rho_0^2} - R,$$

$$\beta_{1p}^2 = \frac{1}{R_r^2} - \frac{1}{4\beta_1^2}\left(-\frac{jk}{L} - \frac{1}{\rho_0^2} + T\right)^2$$

$$- \frac{1}{4\beta_2^2}\left[\left(-\frac{jk}{L} - \frac{1}{\rho_0^2} + T\right)\frac{1}{\beta_1^2\rho_0^2} + \frac{jk}{L} - \frac{1}{\rho_0^2} + R\right]^2$$

$$- \frac{1}{4\beta_3^2}\left\{\frac{1}{\beta_2^2}\left[\left(-\frac{jk}{L} - \frac{1}{\rho_0^2} + T\right)\frac{1}{\beta_1^2\rho_0^2} + \frac{jk}{L} - \frac{1}{\rho_0^2} + R\right]\left(\frac{1}{\rho_0^2} - \frac{T}{\beta_1^2\rho_0^2}\right)\right.$$

$$\left. - \frac{1}{\beta_1^2}\left(-\frac{jk}{L} - \frac{1}{\rho_0^2} + T\right)T + \frac{1}{\rho_0^2} - T\right\}^2 - \frac{B^2}{4\beta_4^2} + \frac{2}{\rho_0^2} - (T + R),$$

$$\beta_{2p}^2 = \frac{1}{R_r^2} - \frac{1}{4\beta_1^2}\left(\frac{1}{\rho_0^2} - T\right)^2 - \frac{1}{4\beta_2^2}\left[\frac{1}{\beta_1^2\rho_0^2}\left(\frac{1}{\rho_0^2} - T\right) + \frac{1}{\rho_0^2} - R\right]^2$$

$$- \frac{1}{4\beta_3^2}\left\{\frac{1}{\beta_2^2}\left[\frac{1}{\beta_1^2\rho_0^2}\left(\frac{1}{\rho_0^2} - T\right) + \frac{1}{\rho_0^2} - R\right]\left(\frac{1}{\rho_0^2} - \frac{T}{\beta_1^2\rho_0^2}\right)\right.$$

$$\left. - \frac{jk}{L} - \frac{1}{\rho_0^2} + T - \frac{T}{\beta_1^2}\left(\frac{1}{\rho_0^2} - T\right)\right\}^2 - \frac{D^2}{4\beta_4^2} + \frac{2}{\rho_0^2} - (T + R) - \frac{KK^2}{4\beta_{1p}^2},$$

$$B = \frac{1}{\beta_3^2}\left\{\frac{1}{\beta_2^2}\left[\left(-\frac{jk}{L} - \frac{1}{\rho_0^2} + T\right)\frac{1}{\beta_1^2\rho_0^2} + \frac{jk}{L} - \frac{1}{\rho_0^2} + R\right]\left(\frac{1}{\rho_0^2} - \frac{T}{\beta_1^2\rho_0^2}\right)\right.$$

$$\left. - \frac{1}{\beta_1^2}\left(-\frac{jk}{L} - \frac{1}{\rho_0^2} + T\right)T + \frac{1}{\rho_0^2} - T\right\}$$

$$\times \left\{\frac{1}{\beta_2^2}\left(\frac{1}{\rho_0^2} - \frac{T}{\beta_1^2\rho_0^2}\right)\left(\frac{1}{\beta_1^2\rho_0^4} - R\right) - \frac{T}{\beta_1^2\rho_0^2} + \frac{1}{\rho_0^2}\right\}$$

$$+ \frac{1}{\beta_2^2}\left[\left(-\frac{jk}{L} - \frac{1}{\rho_0^2} + T\right)\frac{1}{\beta_1^2\rho_0^2} + \frac{jk}{L} - \frac{1}{\rho_0^2} + R\right]\left(\frac{1}{\beta_1^2\rho_0^4} - R\right)$$

$$+ \left(-\frac{jk}{L} - \frac{1}{\rho_0^2} + T\right)\frac{1}{\beta_1^2\rho_0^2} + \frac{1}{\rho_0^2} - R,$$

$$AA_x = \cos\varphi_n k\alpha_n r_0 \frac{2}{\beta_2^2\beta_1^2\rho_0^2}\left(\frac{1}{\rho_0^2} - \frac{T}{\beta_1^2\rho_0^2}\right) + \frac{k\alpha_m 2r_0 \cos\varphi_m}{\beta_2^2}\left(\frac{1}{\rho_0^2} - \frac{T}{\beta_1^2\rho_0^2}\right)$$

$$- \frac{\cos\varphi_n k\alpha_n r_0 2T}{\beta_1^2} + \cos\varphi_l k\alpha_l 2r_0,$$

$$CC_x = \frac{AA_x}{\beta_3^2}\left\{\frac{1}{\beta_2^2}\left(\frac{1}{\rho_0^2}-\frac{T}{\beta_1^2\rho_0^2}\right)\left(\frac{1}{\beta_1^2\rho_0^4}-R\right)-\frac{T}{\beta_1^2\rho_0^2}+\frac{1}{\rho_0^2}\right\}+BB_x,$$

$$BB_x = \cos\varphi_n k\alpha_n r_0 \frac{2}{\beta_2^2\beta_1^2\rho_0^2}\left(\frac{1}{\beta_1^2\rho_0^4}-R\right)+\frac{2}{\beta_2^2}\ k\alpha_m r_0 \cos\varphi_m\left(\frac{1}{\beta_1^2\rho_0^4}-R\right)$$

$$+\cos\varphi_n k\alpha_n r_0 \frac{2}{\beta_1^2\rho_0^2}+\left(\cos\varphi_o k\alpha_o 2r_0\right),$$

$$JJ_x = \frac{AA_x}{2\beta_3^2}\left\{\frac{1}{\beta_2^2}\left[\left(-\frac{jk}{L}-\frac{1}{\rho_0^2}+T\right)\frac{1}{\beta_1^2\rho_0^2}+\frac{jk}{L}-\frac{1}{\rho_0^2}+R\right]\left(\frac{1}{\rho_0^2}-\frac{T}{\beta_1^2\rho_0^2}\right)\right.$$

$$-\frac{1}{\beta_1^2}\left(-\frac{jk}{L}-\frac{1}{\rho_0^2}+T\right)T+\frac{1}{\rho_0^2}-T\right\}+\frac{CC_x}{2\beta_4^2}B+\frac{\cos\varphi_n k\alpha_n r_0}{\beta_1^2}\left(-\frac{jk}{L}-\frac{1}{\rho_0^2}+T\right)$$

$$+\cos\varphi_n k\alpha_n r_0 \frac{1}{\beta_2^2\beta_1^2\rho_0^2}\left[\left(-\frac{jk}{L}-\frac{1}{\rho_0^2}+T\right)\frac{1}{\beta_1^2\rho_0^2}+\frac{jk}{L}-\frac{1}{\rho_0^2}+R\right]$$

$$+\frac{k\alpha_m r_0 \cos\varphi_m}{\beta_2^2}\left[\left(-\frac{jk}{L}-\frac{1}{\rho_0^2}+T\right)\frac{1}{\beta_1^2\rho_0^2}+\frac{jk}{L}-\frac{1}{\rho_0^2}+R\right],$$

$$q_{2px} = \cos\varphi_n k\alpha_n r_0 \frac{1}{\beta_2^2\beta_1^2\rho_0^2}\left[\frac{1}{\beta_1^2\rho_0^2}\left(\frac{1}{\rho_0^2}-T\right)+\frac{1}{\rho_0^2}-R\right]$$

$$+\frac{k\alpha_m r_0 \cos\varphi_m}{\beta_2^2}\left[\frac{1}{\beta_1^2\rho_0^2}\left(\frac{1}{\rho_0^2}-T\right)+\frac{1}{\rho_0^2}-R\right]$$

$$+\frac{1}{2\beta_4^2}\left(CC_x D\ \right)+\frac{JJ_x KK}{2\beta_{1p}^2}+\frac{\cos\varphi_n k\alpha_n r_0}{\beta_1^2}\left(\frac{1}{\rho_0^2}-T\right)$$

$$+\frac{AA_x}{2\beta_3^2}\left\{\frac{1}{\beta_2^2}\left[\frac{1}{\beta_1^2\rho_0^2}\left(\frac{1}{\rho_0^2}-T\right)+\frac{1}{\rho_0^2}-R\right]\left(\frac{1}{\rho_0^2}-\frac{T}{\beta_1^2\rho_0^2}\right)\right.$$

$$\left.-\frac{jk}{L}-\frac{1}{\rho_0^2}+T-\frac{T}{\beta_1^2}\left(\frac{1}{\rho_0^2}-T\right)\right\},$$

$$KK = \frac{1}{2\beta_3^2} \left\{ \frac{1}{\beta_2^2} \left[\left(-\frac{jk}{L} - \frac{1}{\rho_0^2} + T \right) \frac{1}{\beta_1^2 \rho_0^2} + \frac{jk}{L} - \frac{1}{\rho_0^2} + R \right] \left(\frac{1}{\rho_0^2} - \frac{T}{\beta_1^2 \rho_0^2} \right) \right.$$

$$\left. -\frac{1}{\beta_1^2} \left(-\frac{jk}{L} - \frac{1}{\rho_0^2} + T \right) T + \frac{1}{\rho_0^2} - T \right\}$$

$$\times \left\{ \frac{1}{\beta_2^2} \left[\frac{1}{\beta_1^2 \rho_0^2} \left(\frac{1}{\rho_0^2} - T \right) + \frac{1}{\rho_0^2} - R \right] \left(\frac{1}{\rho_0^2} - \frac{T}{\beta_1^2 \rho_0^2} \right) \right.$$

$$\left. -\frac{jk}{L} - \frac{1}{\rho_0^2} + T - \frac{T}{\beta_1^2} \left(\frac{1}{\rho_0^2} - T \right) \right\}$$

$$+ \frac{1}{2\beta_2^2} \left[\left(-\frac{jk}{L} - \frac{1}{\rho_0^2} + T \right) \frac{1}{\beta_1^2 \rho_0^2} + \frac{jk}{L} - \frac{1}{\rho_0^2} + R \right]$$

$$\times \left[\frac{1}{\beta_1^2 \rho_0^2} \left(\frac{1}{\rho_0^2} - T \right) + \frac{1}{\rho_0^2} - R \right]$$

$$+ \frac{1}{2\beta_4^2} BD + \frac{1}{2\beta_1^2} \left(-\frac{jk}{L} - \frac{1}{\rho_0^2} + T \right) \left(\frac{1}{\rho_0^2} - T \right) - 2(T+R) + \frac{4}{\rho_0^2},$$

Here AA_y, BB_y, CC_y, JJ_y and q_{2py} are attained by respectively replacing all the cos function in AA_x, BB_x, CC_x, JJ_y, and q_{2px} by the sin function.

APPENDIX B

Derivation of the Average of the Square of the Power for Partially Coherent MISO

Appendix B is taken from our paper [105].

Here, the calculation of $\langle P^2 \rangle$ is shown. First, we need to calculate $\langle I(\mathbf{p_1})I(\mathbf{p_2}) \rangle$ given by

$$
\begin{aligned}
\langle I(\mathbf{p_1})I(\mathbf{p_2}) \rangle = \frac{1}{(\lambda L)^4} \int_{-\infty}^{\infty}\int_{-\infty}^{\infty} d^2\mathbf{s}_1 \int_{-\infty}^{\infty}\int_{-\infty}^{\infty} d^2\mathbf{s}_2 \int_{-\infty}^{\infty}\int_{-\infty}^{\infty} d^2\mathbf{s}_3 \int_{-\infty}^{\infty}\int_{-\infty}^{\infty} d^2\mathbf{s}_4 \\
\times \langle u(\mathbf{s}_1)u^*(\mathbf{s}_2) \rangle \langle u(\mathbf{s}_3)u^*(\mathbf{s}_4) \rangle_s \\
\times \exp\left[\frac{jk}{2L} \left(|\mathbf{p_1}-\mathbf{s}_1|^2 - |\mathbf{p_1}-\mathbf{s}_2|^2 + |\mathbf{p_2}-\mathbf{s}_3|^2 - |\mathbf{p_2}-\mathbf{s}_4|^2 \right) \right] \\
\times \left\langle \exp\left[\psi(\mathbf{s}_1,\mathbf{p_1}) + \psi^*(\mathbf{s}_2,\mathbf{p_1}) + \psi(\mathbf{s}_3,\mathbf{p_2}) + \psi^*(\mathbf{s}_4,\mathbf{p_2}) \right] \right\rangle_m ,
\end{aligned}
\tag{B.1}
$$

The second line of the Eq. (B.1) is the fourth-order source coherence function for detection time larger than the source coherence time (i.e., slow detector). The last line of Eq. (B.1) is the fourth order spherical-wave coherence function of the medium. The bracket subscripts *s* and *m* denote the ensemble averages over the statistics of source and turbulent medium, respectively. In weak turbulence, log-amplitude and phase fluctuations are assumed to have Gaussian statistics which yield [61]

$$
\begin{aligned}
\left\langle \exp\left[\psi(\mathbf{s}_1,\mathbf{p_1}) + \psi^*(\mathbf{s}_2,\mathbf{p_1}) + \psi(\mathbf{s}_3,\mathbf{p_2}) + \psi^*(\mathbf{s}_4,\mathbf{p_2}) \right] \right\rangle_m \\
= \left[1 + 2B_\chi(\mathbf{s}_1-\mathbf{s}_3,\mathbf{p}_d) + 2B_\chi(\mathbf{s}_2-\mathbf{s}_4,\mathbf{p}_d) \right] \\
\times \exp\left[-0.5D_\psi(\mathbf{s}_1-\mathbf{s}_2,0) - 0.5D_\psi(\mathbf{s}_3-\mathbf{s}_4,0) \right. \\
-0.5D_\psi(\mathbf{s}_2-\mathbf{s}_3,\mathbf{p}_d) - 0.5D_\psi(\mathbf{s}_1-\mathbf{s}_4,\mathbf{p}_d) \\
+0.5D_\psi(\mathbf{s}_1-\mathbf{s}_3,\mathbf{p}_d) + 0.5D_\psi(\mathbf{s}_2-\mathbf{s}_4,\mathbf{p}_d) \\
\left. +jD_{\chi S}(\mathbf{s}_2-\mathbf{s}_4,\mathbf{p}_d) - jD_{\chi S}(\mathbf{s}_1-\mathbf{s}_3,\mathbf{p}_d) \right],
\end{aligned}
\tag{B.2}
$$

Here, we have

A6

$$B_{\chi}\left(\mathbf{s_r} - \mathbf{s_q}, \mathbf{p}_d\right) = \sigma_{\chi_s}^2 \exp\left[-\frac{1}{\rho_0^2}\left(\left|\mathbf{s_r} - \mathbf{s_q}\right|^2 + \left|\mathbf{s_r} - \mathbf{s_q}\right|\cdot\mathbf{p}_d + \mathbf{p}_d^2\right)\right], \text{ with r = 1, 2 and q = 3, 4}$$

is the log-amplitude correlation function, and $\sigma_{\chi_s}^2 = 0.124 k^{7/6} C_n^2 L^{11/6}$ is the spherical wave log-amplitude variance. $Bx \ll 1$ is taken for approximation in weak turbulence [52] and quadratic approximation is used [153]. $D_{\psi}\left(\mathbf{s}_d, \mathbf{p}_d\right) = 2\rho_0^{-2}\left(\mathbf{s}_d^2 + \mathbf{s}_d\cdot\mathbf{p}_d + \mathbf{p}_d^2\right)$ is the wave structure function. The validation of the wave structure function [61] is within $\sqrt{\lambda L}\ \square\ \left|\mathbf{s_d}\right|\ \square\ l_0$. Here, l_0 is the inner scale of turbulence, $\left|\mathbf{s}_d\right|$ is difference of the transverse source coordinates and $\sqrt{\lambda L}$ is the Fresnel zone. $D_{\chi S}\left(\mathbf{s}_d, \mathbf{p}_d\right) = \rho_{\chi S}^{-2}\left(\mathbf{s}_d^2 + \mathbf{s}_d\cdot\mathbf{p}_d + \mathbf{p}_d^2\right)$ is the log-amplitude phase structure, function, and $\rho_{\chi S} = \left(0.114 C_n^2 k^{13/6} L^{5/6}\right)^{-1/2}$ is the coherence length of log-amplitude and phase. Inserting Eq. (3.7) and Eq. (B2) into Eq. (B1) and using the resulting expression in Eq. (2.18), the equation for $\left\langle P^2 \right\rangle$ is obtained as

$$\left\langle P^2 \right\rangle = \sum_{i=1}^{3} Z_i, \tag{B.3}$$

$$\begin{aligned}
Z_i = &\frac{E_i}{\left(\lambda L\right)^4} \sum_{n=1}^{N}\sum_{m=1}^{N}\sum_{l=1}^{N}\sum_{o=1}^{N} \exp\left[-r_0^2 k\left(\alpha_n + \alpha_m + \alpha_l + \alpha_o\right)\right] \\
&\times \exp\left(\frac{\cos^2 \varphi_n k^2 \alpha_n^2 r_0^2}{\vartheta_1^2} + \frac{F_{1x}^2}{4\vartheta_2^2} + \frac{F_{6x}^2}{4\vartheta_3^2} + \frac{F_{10x}^2}{4\vartheta_4^2} + \frac{F_{13x}^2}{4\vartheta_{1p}^2}\right) \\
&\times \exp\left(\frac{\sin^2 \varphi_n k^2 \alpha_n^2 r_0^2}{\vartheta_1^2} + \frac{F_{1y}^2}{4\vartheta_2^2} + \frac{F_{6y}^2}{4\vartheta_3^2} + \frac{F_{10y}^2}{4\vartheta_4^2} + \frac{F_{13y}^2}{4\vartheta_{1p}^2}\right) \\
&\times \frac{\pi^6}{\vartheta_1^2 \vartheta_2^2 \vartheta_3^2 \vartheta_4^2 \vartheta_{1p}^2 \vartheta_{2p}^2} \exp\left(\frac{q_{2pcx}^2 + q_{2pcy}^2}{4\vartheta_{2p}^2}\right),
\end{aligned} \tag{B.4}$$

where

$$F_{1x} = \frac{2\cos\varphi_n k\alpha_n r_0}{\vartheta_1^2 \rho_0^2} + k\alpha_m 2 r_0 \cos\varphi_m + \frac{\cos\varphi_n k\alpha_n r_0}{2\vartheta_1^2 \rho_s^2},$$

$$F_2 = \left(-jkL^{-1} - \rho_0^{-2} + T_{pc}\right)\left(\frac{1}{\vartheta_1^2 \rho_0^2} + \frac{1}{4\vartheta_1^2 \rho_s^2}\right) + \frac{jk}{L} - \frac{1}{\rho_0^2} + R_{pc},$$

$$F_3 = \left(\frac{1}{\rho_0^2} - T_{pc} \right) \left(\frac{1}{\vartheta_1^2 \rho_0^2} + \frac{1}{4\vartheta_1^2 \rho_s^2} \right) + \frac{1}{\rho_0^2} - R_{pc},$$

$$F_4 = \frac{2}{\rho_0^2} - \frac{2T_{pc}}{\vartheta_1^2 \rho_0^2} - \frac{T_{pc}}{2\rho_s^2 \vartheta_1^2},$$

$$F_5 = \frac{2}{\vartheta_1^2 \rho_0^4} + \frac{1}{\vartheta_1^2 \rho_0^2 2\rho_s^2} - 2R_{pc},$$

$$F_{6x} = \frac{F_{1x} F_4}{2\vartheta_2^2} - \frac{\cos\varphi_n k\alpha_n r_0 2T_{pc}}{\vartheta_1^2} + \cos\varphi_l k\alpha_l 2r_0,$$

$$F_7 = \frac{F_2 F_4}{2\vartheta_2^2} - \frac{1}{\vartheta_1^2} \left(-jkL^{-1} - \rho_0^{-2} + T_{pc} \right) T_{pc} + \frac{1}{\rho_0^2} - T_{pc},$$

$$F_8 = \frac{F_3 F_4}{2\vartheta_2^2} - \frac{T_{pc}}{\vartheta_1^2} \left(\frac{1}{\rho_0^2} - T_{pc} \right) - \frac{jk}{L} - \frac{1}{\rho_0^2} + T_{pc},$$

$$F_9 = \frac{F_4 F_5}{2\vartheta_2^2} - \frac{2T_{pc}}{\vartheta_1^2 \rho_0^2} + 2\left(\frac{1}{\rho_0^2} + \frac{1}{4\rho_s^2} \right),$$

$$F_{10x} = \frac{F_{6x} F_9}{2\vartheta_3^2} + \frac{F_{1x} F_5}{2\vartheta_2^2} + \cos\varphi_n k\alpha_n r_0 \frac{2}{\vartheta_1^2 \rho_0^2} + \cos\varphi_o k\alpha_o 2r_0,$$

$$F_{11} = \frac{F_7 F_9}{2\vartheta_3^2} + \frac{F_2 F_5}{2\vartheta_2^2} + \left(-jkL^{-1} - \rho_0^{-2} + T_{pc} \right) \frac{1}{\vartheta_1^2 \rho_0^2} + \frac{1}{\rho_0^2} - R_{pc},$$

$$F_{12} = \frac{F_8 F_9}{2\vartheta_3^2} + \frac{F_3 F_5}{2\vartheta_2^2} + \frac{1}{\vartheta_1^2 \rho_0^2} \left(\frac{1}{\rho_0^2} - T_{pc} \right) + \frac{jk}{L} - \frac{1}{\rho_0^2} + R_{pc},$$

$$F_{13x} = \frac{\cos\varphi_n k\alpha_n r_0}{\vartheta_1^2} \left(-jkL^{-1} - \rho_0^{-2} + T_{pc} \right) + \frac{F_{1x} F_2}{2\vartheta_2^2} + \frac{F_{6x} F_7}{2\vartheta_3^2} + \frac{F_{10x} F_{11}}{2\vartheta_4^2},$$

$$F_{14} = \frac{1}{2\vartheta_1^2} \left(-jkL^{-1} - \rho_0^{-2} + T_{pc} \right) \left(\frac{1}{\rho_0^2} - T_{pc} \right) + \frac{F_2 F_3}{2\vartheta_2^2} + \frac{F_7 F_8}{2\vartheta_3^2} + \frac{F_{11} F_{12}}{2\vartheta_4^2} + \frac{4}{\rho_0^2} - 2\left(T_{pc} + R_{pc} \right),$$

$$\vartheta_{1p}^2 = \frac{1}{R_r^2} - \frac{1}{4\vartheta_1^2} \left(-jkL^{-1} - \rho_0^{-2} + T_{pc} \right)^2 - \frac{F_2^2}{4\vartheta_2^2} - \frac{F_7^2}{4\vartheta_3^2} - \frac{F_{11}^2}{4\vartheta_4^2} + \frac{2}{\rho_0^2} - \left(T_{pc} + R_{pc} \right),$$

$$\vartheta_{2p}^2 = \frac{1}{R_r^2} - \frac{F_{14}^2}{4\vartheta_{1p}^2} - \frac{1}{4\vartheta_1^2} \left(\frac{1}{\rho_0^2} - T_{pc} \right)^2 - \frac{F_3^2}{4\vartheta_2^2} - \frac{F_8^2}{4\vartheta_3^2} - \frac{F_{12}^2}{4\vartheta_4^2} + \frac{2}{\rho_0^2} - \left(T_{pc} + R_{pc} \right),$$

$$\vartheta_2^2 = -\frac{1}{\vartheta_1^2 \rho_0^4} - \frac{1}{16\vartheta_1^2 \rho_s^4} - \frac{1}{\vartheta_1^2 \rho_0^2 2\rho_s^2} + \theta_{pc}^2,$$

$$\vartheta_3^2 = -\frac{F_4^2}{4\vartheta_2^2} - \frac{T_{pc}^2}{\vartheta_1^2} + \varsigma_{pc}^2,$$

$$\vartheta_4^2 = -\frac{F_9^2}{4\vartheta_3^2} - \frac{F_5^2}{4\vartheta_2^2} - \frac{1}{\vartheta_1^2 \rho_0^4} + \xi_{pc}^2,$$

$$\vartheta_1^2 = k\alpha_n - 0.5jkL^{-1} + 2\rho_0^{-2} - T_{pc} + 0.25\rho_s^{-2},$$

$$\theta_{pc}^2 = k\alpha_m + 0.5jkL^{-1} - R_{pc} + 2\rho_0^{-2} + 0.25\rho_s^{-2},$$

$$\varsigma_{pc}^2 = k\alpha_l - 0.5jkL^{-1} + 2\rho_0^{-2} - T_{pc} + 0.25\rho_s^{-2},$$

$$\xi_{pc}^2 = k\alpha_o + 0.5jkL^{-1} - R_{pc} + 2\rho_0^{-2} + 0.25\rho_s^{-2},$$

$$q_{2pcx} = \frac{F_{13x}F_{14}}{2\vartheta_{1p}^2} + \frac{\cos\varphi_n k\alpha_n r_0}{\vartheta_1^2}\left(\frac{1}{\rho_0^2} - T_{pc}\right) + \frac{F_{1x}F_3}{2\vartheta_2^2} + \frac{F_{6x}F_8}{2\vartheta_3^2} + \frac{F_{10x}F_{12}}{2\vartheta_4^2},$$

In Z_1; $E_1 = 1$, $T_{pc} = -\dfrac{j}{\rho_{\chi S}^2} + \dfrac{1}{\rho_0^2}$, $R_{pc} = \dfrac{j}{\rho_{\chi S}^2} + \dfrac{1}{\rho_0^2}$,

In Z_2; $E_2 = 2\sigma_{\chi S}^2$, $T_{pc} = -\dfrac{j}{\rho_{\chi S}^2}$, $R_{pc} = \dfrac{j}{\rho_{\chi S}^2} + \dfrac{1}{\rho_0^2}$,

In Z_3; $E_3 = 2\sigma_{\chi S}^2$, $T_{pc} = -\dfrac{j}{\rho_{\chi S}^2} + \dfrac{1}{\rho_0^2}$, $R_{pc} = \dfrac{j}{\rho_{\chi S}^2}$.

Here, F_{1y}, F_{6y}, F_{10y}, F_{13y}, q_{2pcy} are obtained by respectively replacing all the cosine functions in F_{1x}, F_{6x}, F_{10x}, F_{13x}, q_{2pcx} by the sine functions.

APPENDIX C

Derivation of the Average of the Square of the Power for Partially Coherent MIMO

Appendix C taken from our paper [106].

Here, the calculation of $\langle P^2 \rangle$ is shown for finite sized detector array. we will follow the steps presented in Appendix B. First, we need to calculate $\langle I(\mathbf{p}_1)I(\mathbf{p}_2) \rangle$ which is given by Eq. (B1). Thus, inserting Eqs. (3.7) and (B2) into Eq. (B1), using the resulting expression in Eq. (2.18), the equation for $\langle P^2 \rangle$ is found to be

$$\langle P^2 \rangle = \sum_{i=1}^{3} B_i, \tag{C.1}$$

$$
\begin{aligned}
B_i = {}& E_i (\lambda L)^{-4} \pi^6 \exp\left(-2 r_r^2 R_r^{-2}\right) \\
& \times \sum_{h=1}^{H} \sum_{f=1}^{H} \sum_{n=1}^{N} \sum_{m=1}^{N} \sum_{l=1}^{N} \sum_{o=1}^{N} \exp\left[-r_0^2 k \left(\alpha_n + \alpha_m + \alpha_l + \alpha_o \right) \right] \\
& \times \exp\left(\frac{\cos^2 \varphi_n k^2 \alpha_n^2 r_0^2}{\vartheta_1^2} + \frac{F_{1x}^2}{4\vartheta_2^2} + \frac{F_{6x}^2}{4\vartheta_3^2} + \frac{F_{10x}^2}{4\vartheta_4^2} + \frac{F_{13mx}^2}{4\vartheta_{1p}^2} \right) \\
& \times \exp\left(\frac{\sin^2 \varphi_n k^2 \alpha_n^2 r_0^2}{\vartheta_1^2} + \frac{F_{1y}^2}{4\vartheta_2^2} + \frac{F_{6y}^2}{4\vartheta_3^2} + \frac{F_{10y}^2}{4\vartheta_4^2} + \frac{F_{13my}^2}{4\vartheta_{1p}^2} \right), \\
& \times \exp\left[0.25 \vartheta_{2p}^{-2} \left(q_{2mx}^2 + q_{2my}^2 \right) \right] \left(\vartheta_1 \vartheta_2 \vartheta_3 \vartheta_4 \vartheta_{1p} \vartheta_{2p} \right)^{-2}
\end{aligned}
\tag{C.2}
$$

$$F_{13mx} = \frac{2r_r}{R_r^2} \cos \varphi_h + \frac{\cos \varphi_n k \alpha_n r_0}{\vartheta_1^2} \left(-jkL^{-1} - \rho_0^{-2} + T_{pc} \right) + \frac{F_{1x}F_2}{2\vartheta_2^2} + \frac{F_{6x}F_7}{2\vartheta_3^2} + \frac{F_{10x}F_{11}}{2\vartheta_4^2},$$

$$q_{2mx} = \frac{2r_r}{R_r^2} \cos \varphi_f + \frac{F_{13mx}F_{14}}{2\vartheta_{1p}^2} + \frac{\cos \varphi_n k \alpha_n r_0}{\vartheta_1^2} \left(\frac{1}{\rho_0^2} - T_{pc} \right) + \frac{F_{1x}F_3}{2\vartheta_2^2} + \frac{F_{6x}F_8}{2\vartheta_3^2} + \frac{F_{10x}F_{12}}{2\vartheta_4^2},$$

Here, F_{13my}, q_{2my} are obtained by respectively replacing all the cosine functions in F_{13mx}, q_{2mx} by the sine functions. F_{1x}, F_{6x}, F_{10x}, F_{1y}, F_{6y}, F_{10y}, ϑ_1, ϑ_2, ϑ_3, ϑ_4, ϑ_{1p}, ϑ_{2p}, E_i, T_{pc}, R_{pc} are as previously defined in Appendix B.

CURRICULUM VITAE

PERSONAL INFORMATION

Surname, Name: Gökçe, Muhsin Caner

Date and Place of Birth: 2 January 1985, Malatya

Marital Status: Single

Phone: +90 533 422 54 22

Email: mgokce@cankaya.edu.tr

EDUCATION

Degree	Institution	Year of Graduation
M.Sc.	Ankara Univ., Electrical and Electronics Engineering	2012
B.Sc.	Çankaya Univ., Computer Engineering	2010
B.Sc.	Çankaya Univ., Electronic and Communication Engineering, GPA:360/4	2009

FOREIGN LANGUAGES

Advanced English, Beginner German

PUBLICATIONS (from the thesis)

1. Gökçe, M. C., Baykal, Y., "*Scintillation analysis of multiple-input single-output underwater optical links*", Appl. Opt., vol. 55, no. 22, pp. 6130-6136, (2016).

2. Gökçe, M. C., Baykal, Y., Uysal, M., "*Performance analysis of multiple-input multiple-output freespace optical systems with partially coherent Gaussian beams and finite-sized detectors*", Opt. Eng., vol. 55, no. 11, pp. 111607, (2016).

3. Gökçe, M. C., Baykal, Y., Uysal, M., "*Bit error rate analysis of MISO FSO systems*", Waves Random Complex, vol. 26, no. 4, pp. 642-649, (2016).

4. Gökçe, M. C., Baykal, Y., Uysal, M., "*Aperture averaging in multiple-input single-output free-space optical systems using partially coherent radial array beams*", J. Opt. Soc. Am A, vol. 33, pp. 1041-1048, (2016).

5. Gökçe, M. C., Baykal, Kamacıoğlu, C., Y., Uysal, M., "*Aperture averaging in multiple-input single-output free-space optical systems*", Opt. Eng., vol 54, pp. 066103, (2015).

CONFERENCES (from the thesis)

1. Gökçe, M. C., Baykal, Y., Uysal M., "*Effect of partial coherence on MISO FSO systems*", IEEE International Workshop on Optical Wireless Communication (IWOW), 7-8 September, 2015, İstanbul, Turkey.

2. Gökçe, M. C., Kamacıoğlu, C., Uysal, M., Baykal, Y., "*Performance Analysis of MIMO FSO systems with radial array beams and finite sized detectors*", SPIE Laser Beam Shaping, 17-21 August 2014, California, USA.

3. Gökçe, M. C., Baykal, Y., Uysal M., "*Effect of LED sources on the performance of MIMO FSO systems*", in Proceedings of Çankaya University Symposium, Mühendislik ve Teknoloji Sempozyumu (MTS 7), 15-16 May, 2014, Ankara, Turkey,

PROJECT (from the thesis)

1. High Speed Optical Communication without Fiber, Project Number: 0448.TGSD.2015, Ministry of Science, Industry and Technology, 2015.

GRANT (from the thesis)

1. TÜBİTAK, Scholarship Program for PhD Students (2211-C)